UNIVERSITÀ DEGLI STUDI DI PADOVA

SCUOLA DI SCIENZE
Dipartimento di Geoscienze
Direttore Prof. Nicola Surian

TESI DI LAUREA MAGISTRALE
IN
GEOLOGIA AMBIENTALE E DINAMICA DELLA TERRA
CURRICULUM: EARTH DYNAMICS

FLUID-ROCK INTERACTION IN ECLOGITE-FACIES META-PERIDOTITE (ERRO-TOBBIO UNIT, LIGURIAN ALPS)

Relatore: Prof. Giorgio Pennacchioni

Correlatore: Prof. Marco Scambelluri

Laureanda: Serena Cacciari

ANNO ACCADEMICO 2022/2023

ABSTRACT

The investigation of exhumed blueschist/eclogite-facies ophiolitic serpentinites, i.e. altered oceanic mantle ultramafites, can provide information on dehydration reactions, fluid activity and, possibly, seismicity occurring at depth in subduction zones. Serpentinites, commonly formed through extensive hydration of mantle peridotites at the sea floor or at the forearc region, provide a water storage that is progressively released during subduction by breakdown reactions. Fluid release leads to periodic fluid pressure build up that may eventually lead to brittle failure – a process known as dehydration embrittlement. This mechanism is likely responsible for triggering deep Episodic Tremor and Slow Slip events (deep ETS), composed of correlated tectonic tremor (low-frequency seismic swarms) and aseismic slow-slip events (SSEs), located along the subduction interface at depth ranges of 25-60 km (*Behr & Bürgmann, 2021*). This domain is characterised by high Vp/Vs ratio (indicating the presence of pressurized fluids), and tectonic underplating (resulting in mixing of different lithologies at the subduction interface). These features suggest the association of deep ETS to (i) high pore pressure, due to the progressive release of fluids by dehydration reactions and cyclically reaching supralithostatic values and (ii) rheological heterogeneities, which allow strain partitioning into low-strain domains, developing crack-seal veining and radiating tremor, and high-strain domains accommodating SSEs. The ETS events are well documented by geophysical observations, but only a few exhumed geological assemblages have been proposed as potential records of deep ETS so far.

My Master thesis investigates fluid-rock interactions occurring in meta-peridotites exhumed from subduction zones intermediate-depths. The study focuses on an outcrop of the ophiolitic Erro-Tobbio (E-T) Unit (Voltri Massif, Western Alps), which consists of metamorphosed spinel and plagioclase lherzolites recording deformation related to the oceanic extension (Jurassic Ligurian Tethys) and the subsequent Alpine subduction and exhumation (*Hermann et al., 2000, Scambelluri et al., 1991, Scambelluri et al. 1995*). The deformation experienced during subduction occurred mostly in the depth range identified for deep ETS, with formation of olivine (*Ol*) veins related to breakdown of brucite (*Brc*) and antigorite (*Atg*) to *Ol* at 350-500 °C (*Hermann et al., 2000*). The uneven serpentinization experienced during the oceanic phase led to partitioning of the eclogite-facies deformation into high-strain domains of serpentinite mylonites (interpreted as horizons of SSEs), hosting overprinting brittle and ductile structures and low strain

domains of undeformed meta-peridotites (interpreted as the asperities reaching failure and triggering tremor), mainly affected by brittle deformation.

The investigated outcrop includes both low-strain domains of meta-peridotite and tens-of-cm-thick mylonitic serpentinite. The outcrop displays a pervasive network of mm-thick reaction bands of metamorphic olivine (*Ol₂*), Ti-clinohumite (*Ti-chu*), antigorite (*Atg*), both within the meta-peridotite and serpentinite mylonites. A quantitative description of the relationship between the discrete ductile structures and the orientation of the high-pressure veins and reaction bands was performed with field work. Mapping included the reconstruction of a georeferenced, high-resolution 3D photomosaic and orthophoto of the outcrop, created with the Agisoft Metashape software from images taken by UVA. The orthophoto was used as base map for detailed structural mapping. The study at the meso-scale suggests a correlation between the reaction bands and the mylonites:

- The reaction bands can be grouped into two main sets: (i) Ol-fabric-1 (OlF1), steeply-dipping around 320°, oriented at high angle to the mylonites, (ii) Ol-fabric-2 (OlF2) which trends parallel to the mylonitic domains and progressively increases in spatial density towards the mylonites. Locally, the structural arrangement is more complex and includes multiple sets of olivine veins.
- The N-S trending mylonitic domains include: (i) type 1 mylonites, composed of a planar foliation marked by olivine reaction bands (OlF2), and (ii) type 2 mylonites, apparently Ol-free and displaying a chaotic structure.

The southern part of the outcrop contains, in addition, sub-horizontal, cm-thick veins of *Ol+Ti-chu+Atg*, conjugated right stepping en-echelon arrays of *Ol + Ti-chu* veins, and a foliated rodingitized mafic dyke. Sub-horizontal serpentine veins are also present.

Sample analysis included: (i) transmitted-light optical and SEM microscopy (BSE - Back-Scattered Electron - imaging), (ii) SEM-EDS (Energy Dispersion Spectrometry) compositional analysis, (iii) EBSD (Electron Back-scattered Diffraction) mapping. EBSD maps were post-processed using the Aztec software and the MatLab-based open-source MTEX software. Micro-Raman spectroscopy was used for phase identification and distinction of serpentine polymorphs. The analysis at the microscale evidenced:

- Organization of OlF1 into conjugate *Ol*, *Ti-chu* reaction bands, and radial aggregates, in which *Al-free Atg* replaces *Ol₂+Brc* along a network of microcracks. Coarse *Al-rich Atg* replaces *Ol₁* relics and grows within the reaction

bands, which also contain minor *Brc* and magnetite (*Mt*). Mantle olivine (Ol_1) relics appear structurally linked to the fine-grained Ol_2 that constitutes the reaction-bands. Fe-Mg zonation of the Ol_2 was observed by BSE and determined through SEM-EDS measurements.

- Nucleation of coronitic granoblastic olivine at the contact between *Brc* and *Atg*, reflecting the dehydration reaction $Atg+Br \rightarrow Ol+H_2O$, and within previous Ol_2 sites within the reaction bands. This new olivine (Ol_3), identified as olivine through SEM-EDS point-analyses (composition and Mg/Si ratio characteristic of *Ol*) grows from a porous phase containing antigorite (identified through EDS analyses and Raman spectra).
- EBSD maps acquired on a reaction band and at the contact between Ol_1 relics and the Ol_2 reaction bands, reveal epitaxial growth of Ol_2 over Ol_1. Ol_2 grains are iso-oriented with Ol_1 in areas close to the Ol_1 relics, and the misorientation of the Ol_2 grains increases moving away from the Ol_1 relics.
- *Ol+Ti-chu+Mt+Clinochlore+Di* assemblage within the thicker veins of the southern part of the outcrop and *Ol+Ti-chu* assemblage within the en-echelon veins. The contact between these two sets is sealed by *Mt* and fine-grained *Ol* arranged to form an oblique fabric. From the hand-specimen and the thin sections the following sequence of events was determined: (i) development of horizontal *Atg* veins, hosting μm-sized *Ol* and *Ti-chu* grains, (ii) formation of the *Ol+Ti-chu+Atg+Clinochlore+Di* vein subparallel to the *Atg* vein, decorated by locally sheared, orthogonal *Atg* lamellae, and of the en-echelon veins (iii) reactivation of the veins through the formation of Atg-bearing microcracks (iv) late veins of calcite and chrysotile crosscutting the previous structures.

These observations suggest the occurrence of two stages of *Atg* dehydration, and an intermediate stage of hydration, occurred within the stability field of *Atg, Brc* and *Ol*. The first extensive dehydration following oceanic serpentinization led to the formation of the metamorphic olivine (Ol_2) arranged along the reaction bands. The new stage of hydration was localized in *Atg*-bearing microcracks formed especially within the reaction bands, which were, in turn, affected by dehydration, leading to growth of granoblastic olivine (Ol_3).

In-situ determination of trace elements through LA-ICP-MS allowed the determination of the sources of fluids released during the subduction process. The geochemical analyses

focused on the distribution of fluid-mobile elements (FMEs: *As, Sb, Ba, W, Li, B*) within the different minerals, as tracers of fluid-rock interactions occurring during dehydration reactions in subducted serpentinites. Enrichment in FMEs detected within the metamorphic olivine and in the Al-free antigorite provide evidence of infiltration of external, sedimentary-derived fluids, indicating an opening of the system at eclogite-facies conditions. These observations are consistent with the results reported by *Scambelluri et al. (2012)* and *Clarke et al. (2020).*

INDEX

1. Introduction

Subduction zones are key domains were most of the seismicity, as well as the largest earthquakes, are recorded, and where global-scale recycling of chemical elements occurs. These seismic and geochemical processes are strongly correlated with the occurrence of fluid-rock interactions, especially in relation to breakdown reactions of hydrous minerals.

Seismicity in subduction zones extends down to 660 km depth, and it is divided into three main domains (shallow, intermediate-depth and deep), based on the depth of the focal mechanisms. Most of the recorded seismic activity lies within the first 30 km, and it exponentially decreases with depth, reaching a minimum at 300 km (*Zahn et al., 2020*). The s*hallow domain*, hosts large megathrust earthquakes that nucleate within the seismogenic zone, due to the strong coupling between the subducting slab and the upper plate. The downdip limit of this shallow domains is conventionally at 60 km. *Intermediate-depth earthquakes,* recorded between 60 and 300 km depth, are distributed along a double plane of seismicity, located at the slab interface and 20-40 km within the subducting slab. These two layers are characterized by compressional and extensional focal mechanisms respectively, reflecting the stress field associated with unbending of the rigid portion of the slab. *Deep earthquakes* are concentrated at 520-660 km depth, in correspondence of a compressional domain generated by the resistance opposed by the lower mantle due to its higher viscosity (*Zahn et al., 2020*).

Focusing on intermediate depths, two main mechanisms triggering seismicity have been proposed, considering either a wet and or a dry environment, respectively: (i) dehydration embrittlement, which implies a fluid pressure build up caused by fluid release by breakdown reactions of hydrous minerals, allowing brittle failure even at low differential stresses and high confining pressures; (ii) thermal runaway, related to localization of deformation along ductile precursors, through progressive shear heating and rock softening, eventually resulting in a seismic slip (*Zhan et al., 2020*). However, these two mechanisms cannot explain the development of pseudotachylytes within the dry peridotites of the Lanzo Ultramafic Massif (Western Alps), that are not preceded by any coeval ductile precursors (*Pennacchioni et al., 2020, Scambelluri et al., 2017*). The earthquakes associated to these pseudotachylytes, nucleated at around 70 km depth, have been explained by the presence of small, hydrated regions (serpentinites) embedded within the dry domain, that act as local stress amplifiers, triggering brittle failure of

otherwise dry peridotites at large confining pressures (*Toffol et al., 2022*). Hence, the Lanzo Massif represents a dry end-member of a subduction environment hosting intermediate-depth earthquakes, recorded by the occurrence of widespread eclogite-facies pseudotachylytes. The Erro-Tobbio Unit (Voltri Massif, Ligurian Alps), considered in this thesis, represents the hydrated counterpart, where dehydration embrittlement may have played a role. In fact, the Erro-Tobbio Unit is dominantly composed of meta-peridotites and antigorite serpentinites that experienced the same peak conditions as the Lanzo Massif during the Alpine subduction. Antigorite, main constituent of the Erro-Tobbio rocks, has a fundamental role as carrier of water and fluid mobile elements (FMEs) down to the mantle, since it can store up to 13% of structurally bonded H_2O (*Peters et al., 2017*) and its stability field extends down to 200 km depth (*Ulmer & Trommsdorff, 1995*).

The stress related to convergence in subduction zones is not only released through regular earthquakes, but also through aseismic slip and slow earthquakes. The progressive breakdown of hydrous minerals – such as antigorite – during subduction, is believed to be responsible for cyclic fluid pressure increase, up to lithostatic values, at the slab interface. At depths ranging between 25 and 60 km, the build-up of fluid pressure triggers deep-seated slow earthquakes, via dehydration embrittlement. Slow earthquakes are, in fact, recurrent events detected in correspondence to the domain of the subduction interface where high Vp/Vs ratio indicate the presence of conspicuous pore fluids (*Kato et al., 2010*). Deep slow earthquakes are estimated to release 75-100% of the stress related to convergence and occur mostly downdip the locked zone, where a transitional, conditionally stable domain has been described. This domain, in fact, is characterized by heterogeneous frictional properties, and hosts both seismic and aseismic slip (Fig. 1a).

Discovered through networks of highly-sensitive seismometers and GPS (*Rogers & Dragert, 2003, Obara & Kato, 2016, Bürgmann, 2018*), slow earthquakes are characterized by peculiar properties, consisting of spatio-temporally correlated aseismic and seismic slip (*Rogers & Dragert, 2003, Behr & Bürgmann, 2021*), in the form slow slip or creep events (SSEs), and tectonic tremor, respectively. Accordingly, slow earthquakes are characterized by intermediate properties between seismic (strain rate ~10 s^{-1}, slip rate 10 m/s, stress drop 1-100MPa, characteristic frequency ~10 Hz) and aseismic slip:

- SSEs, are slow, long duration, slip events detected through geodetic observations that don't produce any detectable seismic radiation and last in average 10-20 days. SSEs stand out for the slow propagation of the slip front (~10 km/day), and can reach magnitude values as regular earthquakes (~6-7), relying on slower slip rates (1-2 mm/day, *Giuntoli et al., 2022*) distributed over longer periods, smaller displacements (mm to a few cm), lower stress drops and higher recurrence frequency (months to years) (*Behr & Bürgmann, 2021*).
- Tectonic or nonvolcanic tremor is a weak, long-lasting (few minutes to several hours) seismic signal consisting of a swarm of low-frequency earthquakes (LFEs) and very-low frequency earthquakes – low frequency seismic pulses that last about one minute (*Rogers & Dragert, 2003*). Tremors propagate at the velocity of shear waves (~4 km/s), which are the main components of the tremor waveforms (*Schwartz & Rokosky, 2006*), where the amplitude decays with increasing frequency (*Brown et al., 2013*). LFEs (magnitudes < 2.5) display high amplitudes for frequencies of 2-8 Hz, very-low frequency earthquakes (magnitudes 3-4), for frequencies < 1 Hz (*Shelly et al., 2007, Behr & Bürgmann, 2021*). LFEs account stress drops of 1-100k Pa (*Giuntoli et al., 2022*).

Even though a correlation between SSEs and tectonic tremor is missing in some cases (likely due to the detection limits of the instruments) these two processes are commonly jointly referred to as SSTs (Slow Slip and Tremors, *Behr et al., 2018*) or ETS (Episodic Tremor and Slow slip, *Rogers & Dragert, 2003*).

These recurrent events are located at the mantle wedge corner, a region of the slab interface characterized by the presence of a heterogeneous melange, where mixing of lithologies with different rheology and frictional properties occurs during tectonic underplating (*Behr & Bürgmann, 2021*). The presence of rheological heterogeneities allows strain partitioning between low-strain domains (that behave as small, locked asperities that fail when critically stressed, producing LFEs), and high-strain domains (accommodating SSEs through ductile flow) (*Behr & Bürgmann, 2021, Schwartz & Rokosky, 2006*).

SSTs are well documented by geophysical observations, but the associated deformation processes are still debated, and only a few cases of exhumed rocks have been proposed as possible geological record (*Behr et al., 2018, Giuntoli et al., 2022*). To better constrain the mechanisms underlying ETS, it is, therefore, fundamental to study geological units

displaying evidence of fluid activity and heterogeneous rheology, that reached the depths inferred for ETS occurrence.

In this thesis, we study the ophiolitic Erro-Tobbio Unit of the Western Alps (referred to as E-T Unit hereafter), that, according to previous petrologic and structural studies (*Scambelluri et al., 1991, 1995, Hermann et al., 2000*), can be considered as a suitable candidate for having hosted SSTs during its prograde history in subduction, since:

(i) the E-T Unit displays a pervasive serpentinization, related to the origin from a slow spreading ridge – serpentinite provide an important internal fluid source during subduction;

(ii) the E-T Unit experienced subduction-related eclogite-facies (intermediate depths) conditions during the Alpine history. In particular, evidence of cyclic fluid pressure increases is preserved, represented by sets of olivine (*Ol*) + titanian-clinohumite (*Ti-chu*) veins and reaction bands developed from the antigorite-brucite dehydration. Considering the reconstructed P-T paths of the E-T Unit (*Hermann et al., 2000*, Fig. 1b) serpentinite dehydration reaction and olivine vein formation occurred at depths consistent with the SSTs depth range;

(iii) the E-T Unit displays an internal rheological heterogeneity, likely related to the initial heterogeneity in oceanic serpentinization, with strain partitioning between discrete mylonitic domains (serpentinite mylonites) and low-strain domains (meta-peridotites);

Detailed studies on the hydrofracturing related to the fluid release through antigorite + brucite breakdown, and on its channelization within the network of veins of metamorphic olivine, have been performed by *Plümper et al. (2016)*. The aim of my thesis is to describe at the outcrop and at the micro-scale the structures associated to antigorite-brucite dehydration developed within the SSTs depth range, with the future perspective of contributing to the understanding of the deformation mechanisms possibly associated to this kind of seismicity. Trace elements and, especially, fluid-mobile elements (FMEs: *As, Sb, Ba, W, Li, B*) analysis, have been considered to trace fluid-rock interactions and determine the fluid sources, to constrain the chemical evolution of the systems during the formation of the investigated structures.

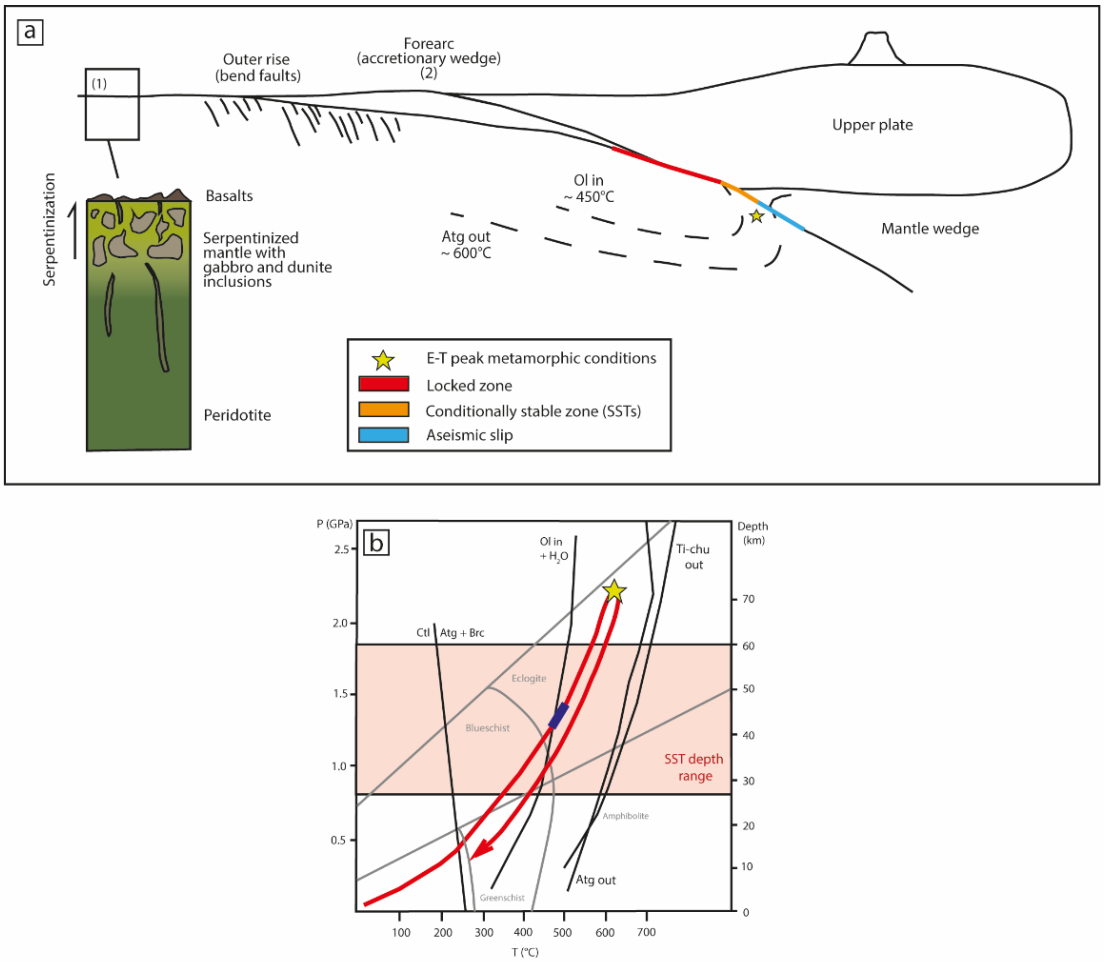

Figure 1. a) Sketch of the geodynamic evolution of the Erro-Tobbio Unit, from the oceanic, low temperature serpentinization at a slow spreading ridge (1) (after Dick et al., 2006), to the forearc serpentinization (2), to the peak metamorphism at eclogite-facies conditions (yellow star). Sketch after *Scambelluri et al. (2019)*. b) Erro-Tobbio Unit P-T path. Estimated peak metamorphic conditions (yellow star) between the olivine-in and the antigorite-out reactions, estimated P-T conditions for the formation of the olivine veins and reaction bands (blue segment) within the SSTs depth range. P-T path after *Hermann et al. (2000)*, SSTs depth range from *Behr & Bürgmann (2020)* and *Brown et al. (2013)*.

2. Geological and tectonic framework

This thesis is focused on a specific domain of the E-T Unit of the Voltri Massif (Internal Pennidic Units, Western Ligurian Alps) (Fig. 1a). The Voltri Massif (Fig. 2b) consists of sub-horizontal thrust sheets emplaced on top of the Hercynic continental basement rocks (gneisses and amphibolites) of the Savona Basement, and it includes from bottom to top: (i) the Voltri-Rossigliano Unit, (ii) the Beigua Unit, and (iii) the ophiolites of the E-T Unit (Fig. 2b). The Voltri Massif is covered by the Molasse sedimentary units, deposited in the Piemontese Tertiary Basin in the Eocene (35-38 Ma) after the exhumation of the Massif. The Molasse breccias and conglomerates, in fact, include clasts from the high-pressure units of the Voltri Massif (Fig. 4a).

The Voltri-Rossigliano (V-R) Unit, consists of high-pressure oceanic metasediments (calcschists) and serpentinites, outcropping as a roughly N-S-oriented band at the centre of the Massif (Fig. 2b). The Beigua Unit, outcropping to the west of the V-R Unit, is made of mylonitic antigorite serpentinites anastomosing around eclogitic metagabbros and mafic dykes. The mafic rocks present in this unit were metasomatized during oceanic serpentinization and transformed to rodingites. The ophiolitic E-T Unit consists of two main peridotite bodies, separated by the V-R Unit and surrounded by the Beigua Unit. To the north the Voltri Massif is confined by the Piemontese Tertiary Basin (Fig. 2b). The Mt. Tobbio meta-peridotites, focus of my Master thesis, outcrop at the easternmost boundary of the Ligurian Alps, close to the high-pressure Sestri-Voltaggio zone – the geological limit between the Alpine and the Apennine Units. The E-T Unit also contains mafic dykes, that were locally rodingitized due to early metasomatism. During subduction, non-rodingitized dykes developed an eclogite-facies paragenesis of *omphacite* + *garnet* + *chloritoid* + *chlorite* + *talc*, that yields peak high-pressure metamorphic conditions of 550-600°C and 2.0-2.5 GPa (*Scambelluri et al., 1991, Messiga et al., 1995*).

The ophiolitic rocks of the Voltri Massif represent remnants of the Jurassic Ligurian Tethys and experienced a complex tectonic evolution, detailed in the following section for the E-T Unit, the ultramafic unit of the Massif considered in my study.

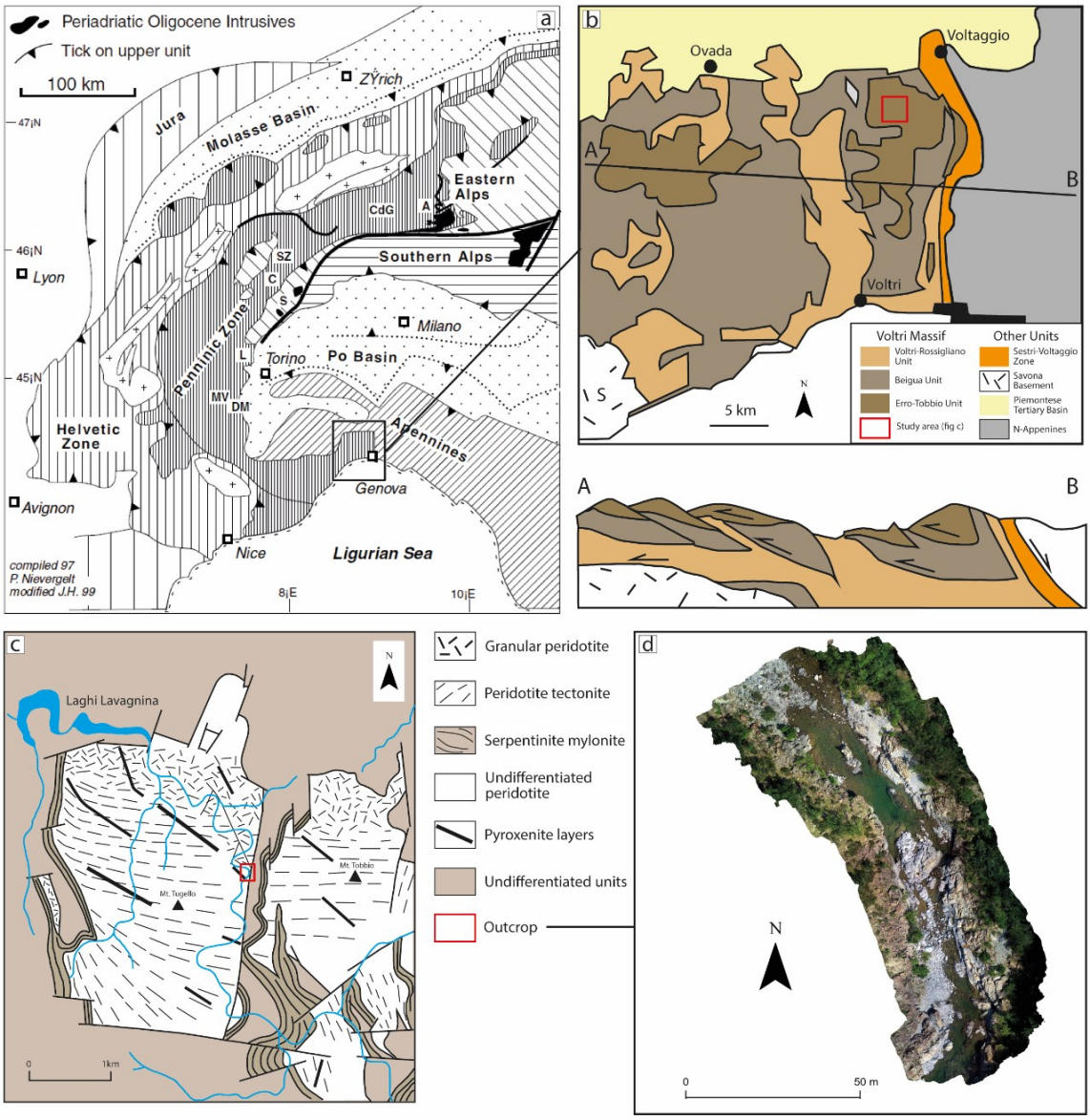

Figure 2. Geographical and geological framework of the investigated area. a) Schematic map of the Western Alps from *Hermann et al. (2000)*, b) Schematic geological map and cross section of the Voltri Massif nappes stack (after *Hermann et al., 2000*), the red area identifies the region of c), c) schematic geological map of the eastern section of the Erro-Tobbio Unit (Mt. Tobbio) within the Capanne di Marcarolo Natural Park, after *Peters et al. (2020)*, d) Orthophoto map of the investigated outcrop.

2.1 Tectonic evolution of the Erro-Tobbio Unit

The protolith rocks of the E-T Unit are spinel and plagioclase lherzolites, attributed to the Adria subcontinental mantle (*Scambelluri et al., 1995*). The tectonic evolution of these rocks consists of three main phases:

Phase 1: *Late Jurassic - Late Cretaceous extension, low-grade serpentinization*

The opening of the Ligurian Tethys occurred during the Late Jurassic – Early Cretaceous, from a slow-spreading ridge separating the European and the Adria continental plates. Mantle unroofing at the spreading ridge, occurred through lithospheric extensional shear zones (detachment) (*Messiga et al., 1995*), caused the exhumation of the subcontinental mantle at the seafloor (Fig. 3a). Along the upper part of the detachment, the ultramafites experienced heterogeneous low-grade serpentinization (chrysotile and lizardite), by interaction with seawater. At the same time, the associated gabbros and mafic dykes, with a MOR affinity, were locally rodingitized due to the metasomatic alteration within the host ultramafic rocks (*Messiga et al., 1995*). Shearing during tectonic unroofing caused the formation of the regional N-S schistosity of the ET meta-peridotites.

Phase 2: Late Cretaceous - Paleocene compression, subduction and high-pressure metamorphism

The closure of the Ligurian Tethys, associated with intra-oceanic subduction, began in the Late Cretaceous, around 25 Ma after the end of the oceanic spreading. South dipping subduction continued during the Palaeocene eventually involving the European plate margin (Fig. 3b). During subduction, the E-T Unit initially experienced a further stage of serpentinization, related to seawater infiltration at the forearc region, associated with plate bending (*Faccenda, et al., 2009*, *Scambelluri et al., 2019*). At deeper subduction levels, the Erro-Tobbio Unit ophiolites underwent a complex tectono-metamorphic evolution, eventually leading to eclogite-facies peak metamorphic conditions at 550-600°C and 2.0-2.5 GPa (70-80 km, *Peters et al., 2020, Plümper et al., 2016*).

Subduction-related deformation localized along the domains of most pervasive oceanic serpentinization, leading to formation of serpentinite mylonites (high-strain domains). Within the less serpentinized domains, meta-peridotites preserved the mantle textures and, partly, the mineral assemblages (low-strain domains). The serpentinite mylonites wrap around the undeformed meta-peridotite cores, which mostly experienced static eclogite-facies metamorphism. In both high and low-strain domains, the formation of en-

echelon veins containing high-pressure assemblages (olivine + Ti-clinohumite + antigorite) is interpreted as hydrofracturing that resulted from fluid release in relation to the antigorite-brucite breakdown (e.g. *Hermann et al., 2000*). In the serpentinite mylonite these structures were later deformed, forming a complex set of overprinting brittle and ductile structures.

The Alpine deformation consisted of 3 stages recorded within the serpentinite mylonites (Fig. 4b), with formation of structures indicating a top-to-the-NW shear sense, consistent with a prograde path (*Hermann et al., 2000*): (1) antigorite shear bands, (2) en-echelon olivine-bearing veins, related to the onset of antigorite breakdown , and (3) olivine-bearing shear bands. These 3 stages occurred before the inversion in shear sense associated to the onset of exhumation.

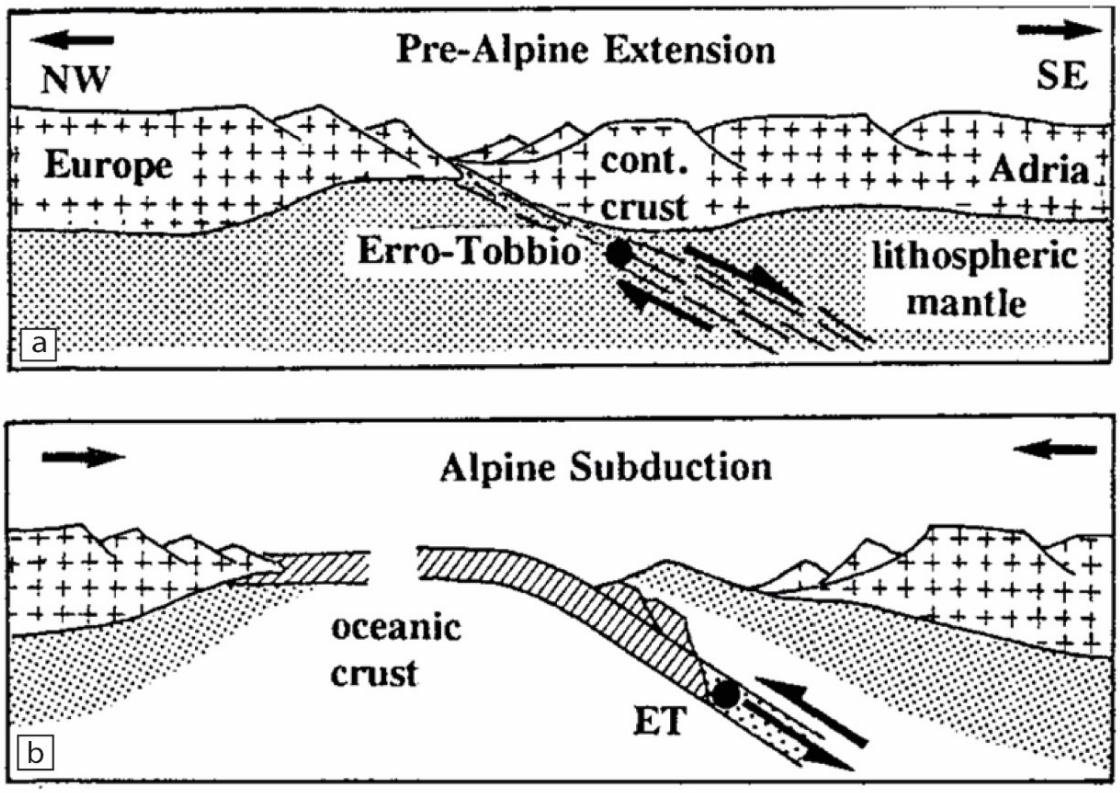

Figure 3. Tectonic evolution of the Erro-Tobbio Unit. Sketches of a) the Cretaceous extensional phase and b) the Palaeocene compression, from *Scambelluri et al. (1995)*.

Phase 3: Eocene-Oligocene exhumation

The exhumation of the Voltri Massif began during the Eocene, with the simultaneous deposition of the Molassa (Fig. 4a) in the Piemontese Tertiary Basin. The onset of the exhumation is recorded by the presence of structures with a top-to-the-SE shear sense, opposite with respect to the kinematics of prograde structures. As suggested by *Hermann et al. (2000)*, the exhumation mechanism for this deeply subducted unit is related to the buoyancy of serpentinites, extensively developed within the unit. *Vignaroli et al. (2010)* propose a two stages exhumations process: early synorogenic exhumation within the subduction zone (Eocene), and post-orogenic exhumation during crustal thinning related to regional geodynamic reorganization (Oligocene).

In summary, the rocks of the Erro-Tobbio Unit can be attributed to 2 main groups based on their structure, resulting from their complex tectono-metamorphic evolution (Fig. 2c): (i) undeformed granoblastic meta-peridotites (low-strain domains) affected by brittle prograde deformation; (ii) serpentinite mylonites (high-strain domains), anastomosing around mafic dykes boudins and undeformed meta-peridotite domains, recording all the stages of prograde deformation (*Hermann et al., 2000*).

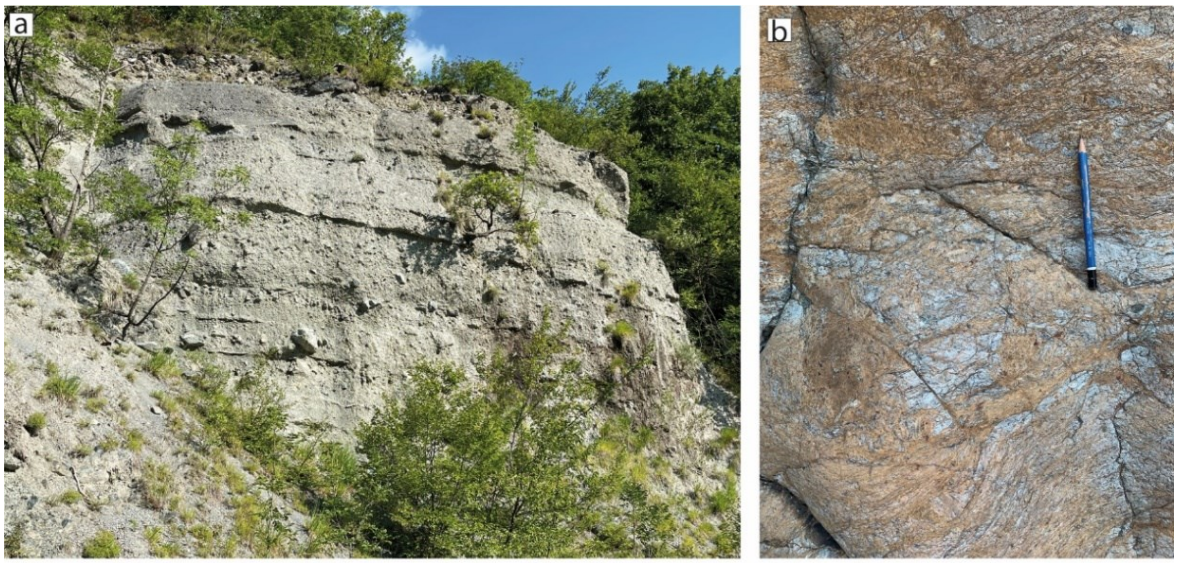

Figure 4. Field photographs of a) the Piemontese Tertiary Basin Molasse sediments, b) serpentinite mylonites belonging to the high-strain domains of the Erro-Tobbio Unit.

3. Methods

The study of the observed petrological and structural features at different scales involved different techniques. Mesoscale analysis included field work and geological survey of an outcrop; investigations at the microscale involved optical and SEM microscopy, micro-Raman spectroscopy and geochemical analyses. In detail, transmitted-light optical microscopy was used in the first place for petrological and microstructural analyses. Ten thin sections containing the key structures were studied, including six collected for previous studies by Prof. Marco Scambelluri (21.37A, 21.37B, 21.38A, 21.38B, 21.39A, 21.39B). Further microstructural observations were performed on a single thin section (2139A) by Scanning Electron Microscopy (SEM). BSE and SE modes were used to image the structures at the micrometric and nanometric scale. EBSD maps were acquired to investigate the crystallographic orientation of the metamorphic olivine forming the veins/reaction bands, SEM-EDS compositional analyses were performed to identify mineral phases not resolvable by Raman spectroscopy. Micro-Raman spectroscopy was used for qualitative identification of the mineral phases and, especially, to distinguish the serpentine polymorphs. LA-ICP-MS analysis was used for *in-situ* determination of trace elements, carried out under the supervision of Dr. Enrico Cannaò, to constrain the role of fluids in the different deformation stages and the chemical evolution of the system during subduction.

3.1 Field work

The focus of the fieldwork was the detailed structural mapping of the outcrop along the Gorzente river, especially addressed at the definition of the architecture of the olivine veins/reaction bands and their relationship with the discrete ductile domains.

The structural map was drawn in QGIS using a high-resolution ortho-photograph of the outcrop as a base map. This ortho-photograph was created from high-resolution images acquired with a drone (DJI Phantom 4 Pro drone equipped with a DJI FC6310 camera). The photos were taken with an overlap of 70% in all directions, to allow an accurate photogrammetric analysis. Two drone flights, planned using the DJI software, were performed at different heights, (15 and 20 m), resulting in outputs with two different resolutions. Since the lightning conditions were not ideal, the photos were post-processed

using Adobe Lightroom to fix the exposure, and the photogrammetric elaboration for the creation of the high-resolution 3D models and georeferenced ortho-mosaics was carried out afterwards using the Agisoft Metashape software. The ortho-photograph covering a larger area of the outcrop was saved in tiff format to be used as a base layer for field mapping. The structural data acquired in the field were finally added to the QGIS project to complete the structural map.

The drone-made ortho-mosaics were integrated with a high-resolution 3D model and ortho-photograph of a wall of the southern part of the outcrop, to schematise the en-echelon geometry of olivine veins (Fig. 12, Chapter 4). In this case, the photos were taken with a Nikon D700 camera, with an overlap of ~70%, and processed with Agisoft Metashape for the creation of the high-resolution 3D model and ortho-photograph.

During the fieldwork the orientation of the veins and reaction bands was systematically measured, as well as the orientation of the foliation displayed by the mylonite horizons. The structural data were elaborated and plotted using the Stereonet software. Sample 22-45, displaying overprinting high-pressure veins, was collected, and cut for the creation of four adjacent thin sections. Mapping formed also the basis for a structurally-controlled collection of representative samples.

3.2 Optical microscopy

A first optical petrographic and microstructural analysis was carried out on all thin sections (21.37A, 21.37B, 21.38A, 21.38B, 21.39A, 21.39B, 22-45A, 22-45B, 22-45C, 22-45D) with a transmitted-light ZEISS polarizing microscope. Thin sections from 2137A to 2139B have a thickness of 30-40 μm, while the thin sections obtained from sample 2245 are slightly thicker (50 μm), with the purpose of performing laser ablation for trace element analysis. The focus of the optical analysis was to perform an explorative study to select the samples and the domains for more detailed and in-depth investigations. Microphotographs of the key structural and petrographic elements were taken with a Canon EOS 550D camera at different magnifications.

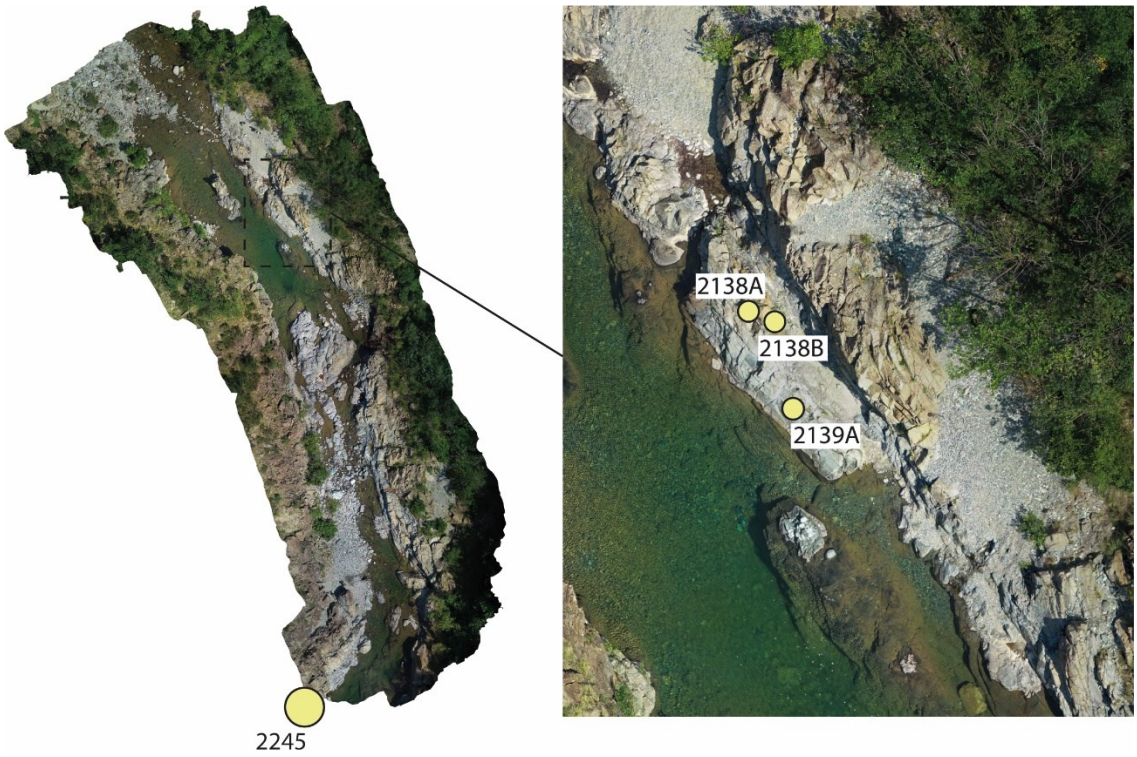

Figure 5. Sample locations in the investigated area.

3.3 Micro-Raman Spectroscopy

Micro-Raman spectroscopy was applied for a qualitative identification of the main mineral phases and, especially, to distinguish the serpentine polymorphs. It was carried out on selected, polished thin sections of (i) a meta-peridotite containing a network of reaction bands (2139A), (ii) a mylonite (2138A) and (iii) a meta-dunite (2138B) collected along the transect displaying the contact between the three rock-types. Three thin sections of sample 22-45 (22-45A, 22-45B, 22-45D) were analysed to define the components of the overprinting sets of veins. The analyses were carried out at the Department of Geosciences of the Università degli Studi di Padova, using a WITec Raman alpha 300 RS, equipped with a Zeiss microscope and a motorised x-y-scanning stage. The Raman analyses were executed at the highest resolution, using a 50x objective, while transmitted and reflected-light microphotographs were acquired at different magnifications. The spectra were acquired in the range 100-3750 cm^{-1}, using a 532 nm laser, with an estimated spot size of 0.5 µm. Most measurements were performed using a power of 2 mW, to avoid damage, especially in presence of lizardite (damage was immediately observed at higher power of 3 mW).

The micro-Raman was used for point-analysis and acquisition of maps. The integration time used for point-analyses on thin sections 2139A, 2138A, and 2138B was 10 s and the accumulation time 3 s. The maps, instead, were acquired using different working conditions: (i) the map on thin section 2139A (*Rmap1*) was acquired using a continuous scanning of the selected areas, with a power of 2 mW and an integration time of 0.15 s*, (ii)* the map on thin section 2138A (*Rmap2)* was acquired using 2 mW, 0,6 s integration time and a rastered scanning of the area with a 2 μm step size. *Rmap1 and Rmap2* are reported in the Appendix (A2, A3). Point-analysis on thin sections of sample 22-45 was performed with 5 s integration time, 6 s accumulation time and 2.5 mW.

The spectra were processed for background and cosmic ray spikes removal using the OMNIC Spectra software. The open-source Crystal Sleuth software, used together with the RRUFF Raman Mineral library was employed for mineral identification. The WITio MATLAB toolbox (*Tapani Holmi & Lipsanen, 2020*) was used to review the spectra acquired with the maps.

3.4 Scanning Electron Microscopy

High-resolution microstructural investigation was performed using the dual-beam FIB-FE-SEM TESCAN SOLARIS SEM available at the Department of Geoscience of the Università degli Studi di Padova. SE-BSE images, EDS microchemical measurements and EBSD maps were acquired using, respectively, SE and mid-angle BSE detectors, Silicon Drift EDS Ultim Max 65 detector, and the CMOS-Symmetry EBSD detector. The SEM analysis was performed on a single thin section (2139A), on sites selected through optical investigations. The thin section was SYTON-polished to remove the surface damage related to Raman analyses and to standard polishing procedures, and coated with a 7 nm carbon layer.

Imaging of the microstructures was performed through SE and BSE modes, with 5 kV acceleration voltage, 300 pA beam current and 4-5 mm working distance.

EBSD maps were acquired on 4 selected domains of the thin section, to investigate the relative crystallographic orientation of the metamorphic olivine grains, mantle olivine relics and coarse Al-rich antigorite. Working conditions during EBSD mapping were: 15 kV acceleration voltage, 3 nA beam current, 15-17 mm working distance, 70° sample

tilting. During acquisition: the exposure time was 4 ms, the dwell time 10 μs, the step size variable from 0.7 μm (*Smap1* and *Smap2*) to 0.35 μm (*Smap3*, and *Smap4*).

The large size of the maps required an initial processing of the EBSD data using the Aztec software, for wild spike removal, performed considering 6 neighbouring pixels for all maps, and interpolation of empty pixels. *Smap3* was divided into two subsets, to separate the orientation data related to the metamorphic and the mantle olivine. The clean maps were saved in crp/crc format and further elaborated using the open-source Matlab toolbox MTEX by Ralf Hielscher (https://mtex-toolbox.github.io/). All the pole figures are projected on the lower hemisphere.

Working conditions for SEM-EDS point measurements were: 15 kV acceleration voltage, 1 nA beam current, 5 mm working distance and 20 s acquisition time.

3.5 LA-ICP-MS

The in-situ determination of trace elements by LA-ICP-MS (Laser Ablation Inductively Coupled Plasma Mass Spectrometry) on thin sections 2139A, 22-45A, 22-45D was performed at the laboratory of Geochemistry, Geochronology and Isotope Geology of the Università degli Studi di Milano-La Statale, for quantification of trace elements in the key mineral phases. The used laser ablation system is the Teledyne Photon Machines Analyte Excite Excimer, equipped with a double volume sample holder and with an air-cooled 193 nm ArF Excimer laser. The spectrometer is a Thermoscientific ICP-MS iCAP RQ, equipped with a single quadrupole for mass-based separation of the elements. The minimum spot size reachable by the instrument is 1 μm, but the analyses were performed with spot sizes of 20-50 μm, to ensure high accuracy and precision of the data; a smaller spot size would have allowed to measure smaller phases individually, but would have provided less reliable measurements. The working conditions for the analyses with a spot size of 35-50 μm were: 3 J/m^2 fluence for serpentines and 2.5 J/m^2 fluence for olivine, brucite, chlorite, Ti-clinohumite and pyroxenes; 10 Hz frequency (shot/s) and 60 s dwell time. The dwell time included 40 s for initial background measurement, and 10 s for the wash out phase at the end of the sample measurement, to allow the movement of the laser beam to the next site. Grains of metamorphic olivine and Al-free antigorite replacing metamorphic olivine and brucite were analysed with a spot size of 20-25 μm, dwell time of 30 s, fluence of 3.5 J/m^2 and 10 Hz. The calibration was performed by analysing the

USGS GDS-2g standard (synthetic basaltic glass), and three glasses for quality control, BCR-2g (homogenised natural basalt), ML3B (synthetic basaltic glass) and ARM3 (synthetic andesitic glass). The measurements of the standard and of the quality control samples were set every ~ 20 unknowns. The output data were processed using the Glitter software, using as internal standards the values reported in the Appendix (A6).

The reliability of the analyses was verified by computing the accuracy (*(mean-reference)/reference*) and precision (as RSD%, Relative Standard Deviation = *standard deviation/mean*) of the measurements obtained for the GDS-2g, BCR-2g, ML3B and ARM3 glasses. The reference values of the trace element contents in the standard glasses were downloaded from the Georem database preferred values (http://georem.mpch-mainz.gwdg.de). The certainty of the measurements was confirmed by accuracy values below 20% and RDS% values below 10%. The precision and accuracy values for the glasses are reported in the Appendix (A7).

4. Field work

The investigated outcrop (Fig. 7) is a well exposed domain along the Gorzente River (Bosio, AL) that consists of N-S-trending discrete mylonitic serpentinite layers cutting through meta-dunite and meta-peridotite low-strain domains. The rocks from this outcrop have been previously described in a series of papers (*Scambelluri et al., 1995, Plümper et al., 2016*), but a detailed structural map of the outcrop is missing. In particular, Plümper et al. (2016) describe a network of overprinting *Ol* + *Ti-chu* reaction bands and veins across the meta-peridotite that formed from high-pressure dehydration of antigorite-brucite during subduction. A main aim of the field work and mapping along the Gorzente outcrop was to establish the architecture of the reaction bands and veins within the low-strain domains and their relationship with the mylonitic zones. The map is shown in Fig. 7 and Fig. 8, and the outcrop structure is schematized in Fig. 10a.

The meta-peridotites display mm-sized whitish pyroxenes visible at the hand-specimen scale. Meta-dunites are characterized by the presence of mm-to-cm-sized sites of spinel pseudomorphosed by magnetite (*Mt*) rimmed by chlorite (*Chl*), typically well recognizable on weathered outcrop as dark metallic grains (*Mt*) surrounded by white mantle (*Chl*) within the dark orange rock (Fig 6a). The meta-peridotite-dunite contact is locally marked by a reaction horizon, or, more commonly, it is gradual. The meta-peridotites host parallel meta-dunite layers (spinel-rich) and ~10 cm-thick pyroxenite bands, which define the large-scale schistosity related to the mantle exhumation along the oceanic detachment.

Figure 6. Field photographs of the two main lithologies. a) Meta-dunite hosting mm-to-cm-sized sites of spinel pseudomorphosed by *Mt* and *Chl*, b) Meta-peridotite displaying a set of olivine reaction bands (OlF1, see below), dissected by a thicker olivine vein.

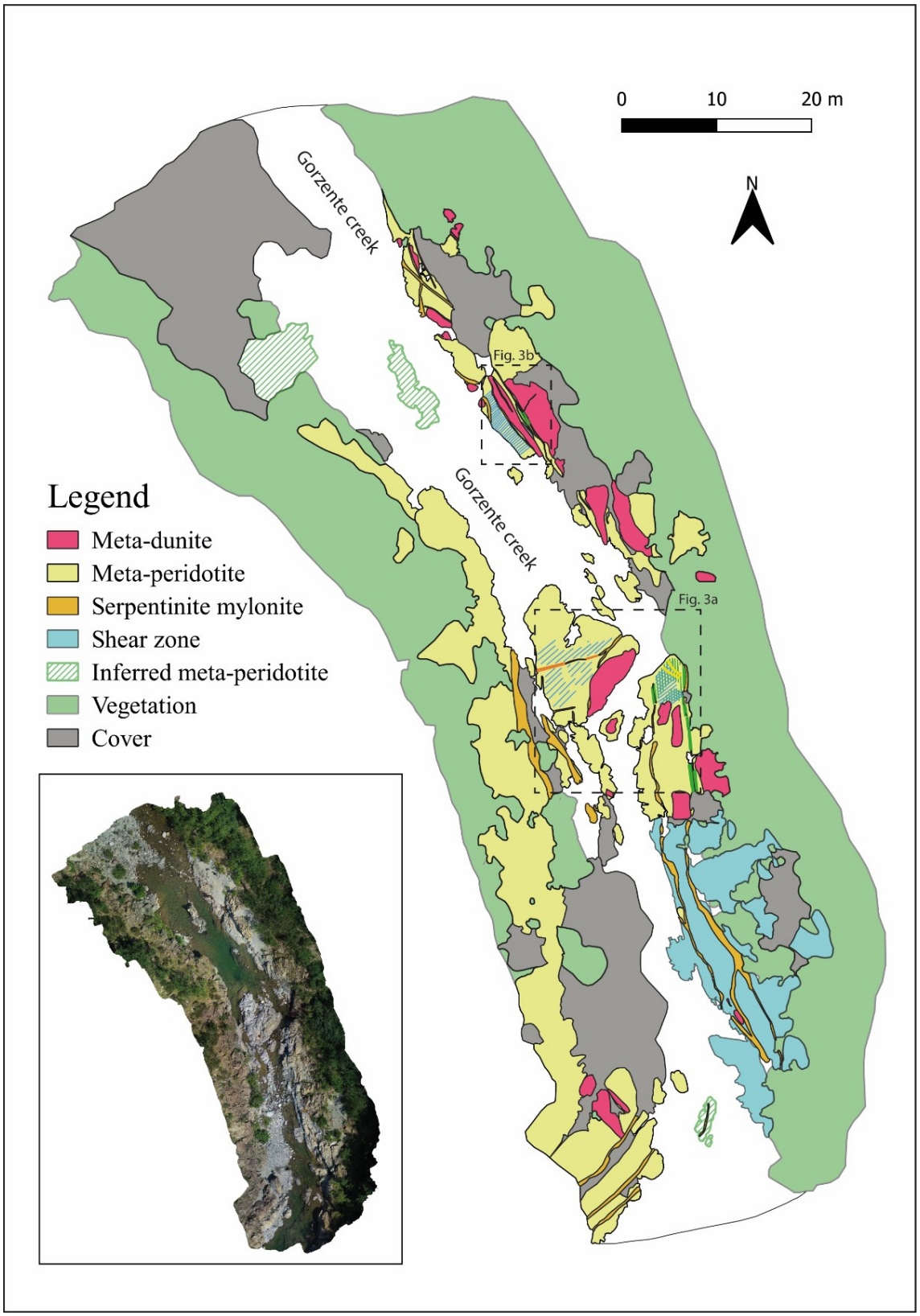

Figure 7. Structural-geological map of the investigated outcrop along the Gorzente creek. Two magnifications of the areas displaying the structures of interest are shown in Fig. 8.

The meta-peridotites contain *Ol + Ti-chu* mm-thick reaction bands and veins arranged in steeply-dipping sets of closely cm-spaced structures. As shown in the structural map and in the structural sketch (Fig. 10a), a set (olivine fabric 1: OlF1) steeply-dipping around 320° prevails in the low-strain domain (LS1) along the creek. Together with this dominant set, veins and reaction bands with other orientations occur, and locally the main veins/reaction band array resembles a set of conjugate structures. In LS1, the main OlF1 abuts at a high angle against the serpentinite boundary. In contrast, the low-strain domain (LS2) shows more complex arrangements of olivine veins and reaction bands. In the core of LS2, a cm-spaced set (OlF2) is present with a trend parallel to the flanking serpentinite mylonites. On the eastern side, OlF2 progressively intensifies to form a closely spaced (mm-spacing) fabric parallel to the mylonitic foliation. The same fabric is also locally present, adjacent to the serpentinite mylonite on the western border of LS2. In addition to the dominant OlF1, other sets are locally present, and some complex networks are locally developed. The orientations of the mylonites and the olivine fabric are summarized in the stereonet of Fig. 10b.

The serpentinite mylonites include 2 main types: (i) mylonites with a planar foliation marked by closely spaced olivine reaction bands (OlF2) (type 1); (ii) serpentinite mylonites with a chaotic structure, apparently free of macroscopic olivine (type 2). Type 1 mylonites make a transition to meta-peridotite by progressive decrease of the foliation intensity and decrease in spacing of the olivine reaction bands (Fig. 8a, 9c, 9d, 10a). The contact between type 1 and type 2 mylonites is sharp and parallel to the foliation (Fig. 8, 9c). On the contact plane a slikenline lineation marked by serpentine fibres is locally present, with a high angle plunge towards SW. Both the type 1 and 2 mylonites are a few cm to 10s of cm wide with a NNW-SSE to NE-SW trend, subparallel to the stream. The mylonites locally contain foliation-parallel calcite veins.

In the south-eastern part of the mapped area, where the serpentinite mylonites (M2 and M3) bounding the LS2 converge, the meta-peridotite and the meta-dunite domains are deformed in a metre-thick shear zone where the foliation is pervasively folded, especially at the convergence zone between M2 and M3. In these folded mylonites, *Ol + Ti-chu* reaction bands and veins are either folded (Fig. 9h) or arranged along the fold axial plane.

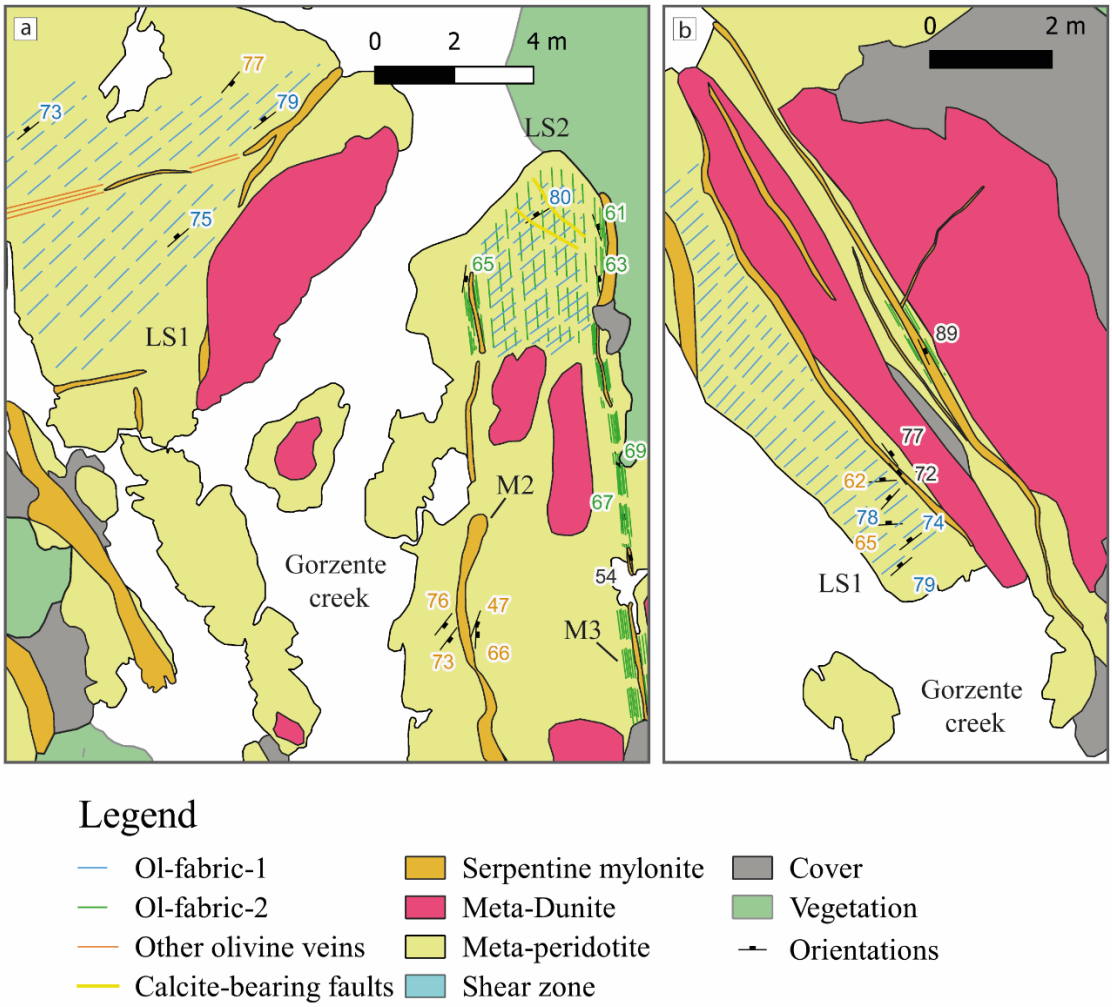

Figure 8. Detailed structural map of two key areas of the outcrop showing all the different structures. The colours of the labels indicating the dip angles are consistent with the colour of the respective structural element, black is for serpentinite mylonites.

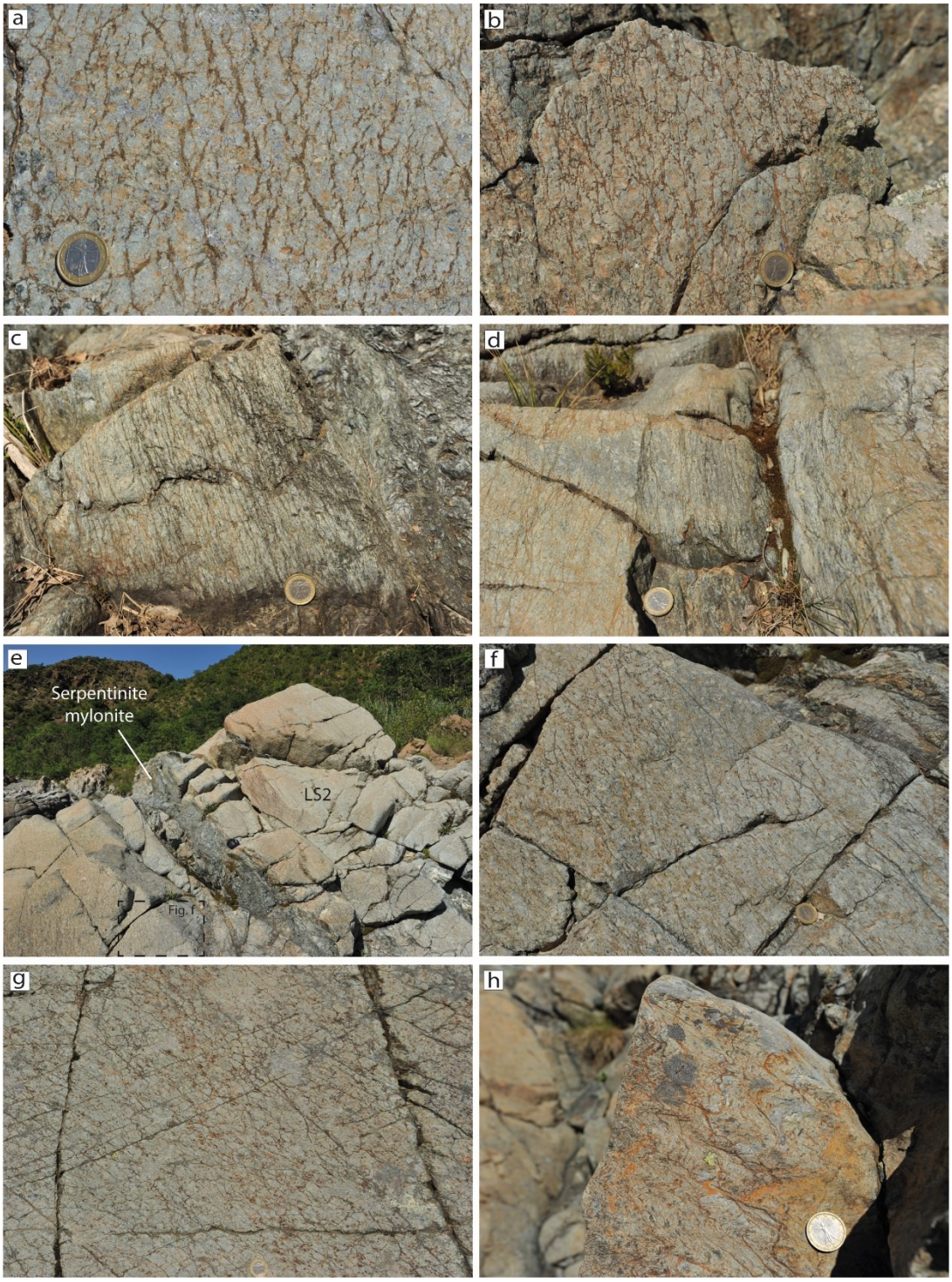

Figure 9. Field photographs of the sets of olivine veins/reaction bands and the serpentinite mylonites. a) Close view of the OlF1 hosted in LS1 along the creek, b) OlF1 intersecting OlF2 in LS2, within some tens of cm from the serpentinite mylonite (M3 in Fig. 10a), c) sharp foliation parallel contact between the type 1 mylonite, constituted by the olivine reaction bands, and the chaotic serpentine mylonite (type 2), locally tiny domains of type 2 mylonite are embedded within type 1 mylonite, d) type 2 mylonite, intensive foliation of the meta-peridotite given by the OlF2-parallel reaction bands, e) overview of the relationship between the type 1 mylonite and the LS2 of meta-peridotite, f, g) other sets of olivine veins cross-cutting the meta-peridotite, h) folded *Ol + Ti-chu* veins/reaction bands within the shear zone (SZ, Fig.10a).

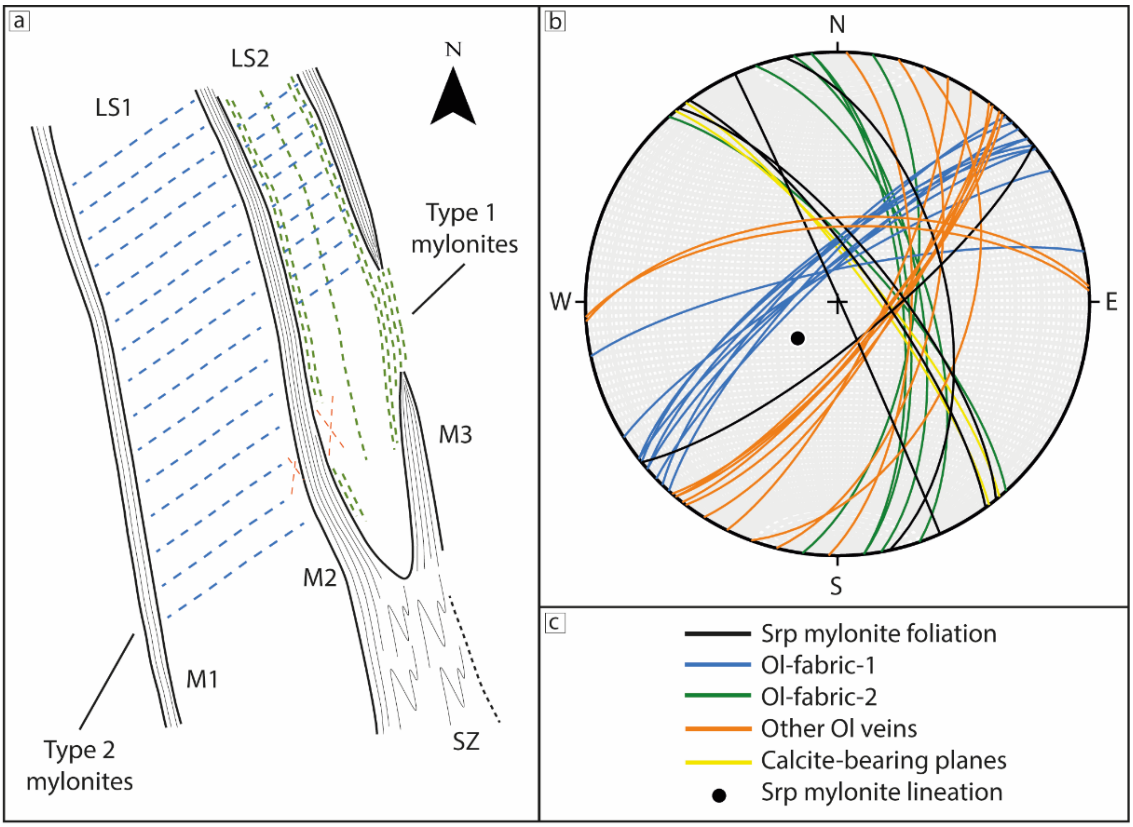

Figure 10. a) Sketch of the field relationships between the serpentinite mylonites (M1, M2, M3) converging to the SE in the m-thick shear zone (SZ), and the olivine fabrics developing within the meta-dunite-meta-peridotite low-strain domains (LS1 and LS2); legend in c). The NE-SW-trending OlF1 is dominant within LS1. In LS2, the OlF2 takes over close to the mylonites, trending parallel to these. Locally, OlF2 constitutes type 1 mylonites. b) Stereonet showing the orientations of all the structural elements (equal area, lower hemisphere projection), legend in c).

Outside the mapped area, a few tens of meters upstream the Gorzente creek, the meta-peridotite includes cm-thick *Ol* + *Ti-chu* veins, arranged into a sub-horizontal set and in right-stepping en-echelon veins at high angle to the sub-horizontal set (Fig. 12). One sample of these veins was collected (22-45) for lab analysis. Locally, the rims of the veins are decorated by orthogonal antigorite fibres displaying a crack-seal texture. The occurrence of vein-parallel exposures of these veins allow to observe that these structures are closely linked to the mm-thick *Ol* reaction bands (Fig. 11d). This area is also characterized by the presence of other sets of olivine-bearing veins with different orientations, and major fractures cross-cutting the previously listed features (Fig.12). An NNW-SSE-striking, foliated, rodingitized mafic dyke dissects the meta-peridotite a few meters downstream the area in Fig 12 (Fig. 11b).

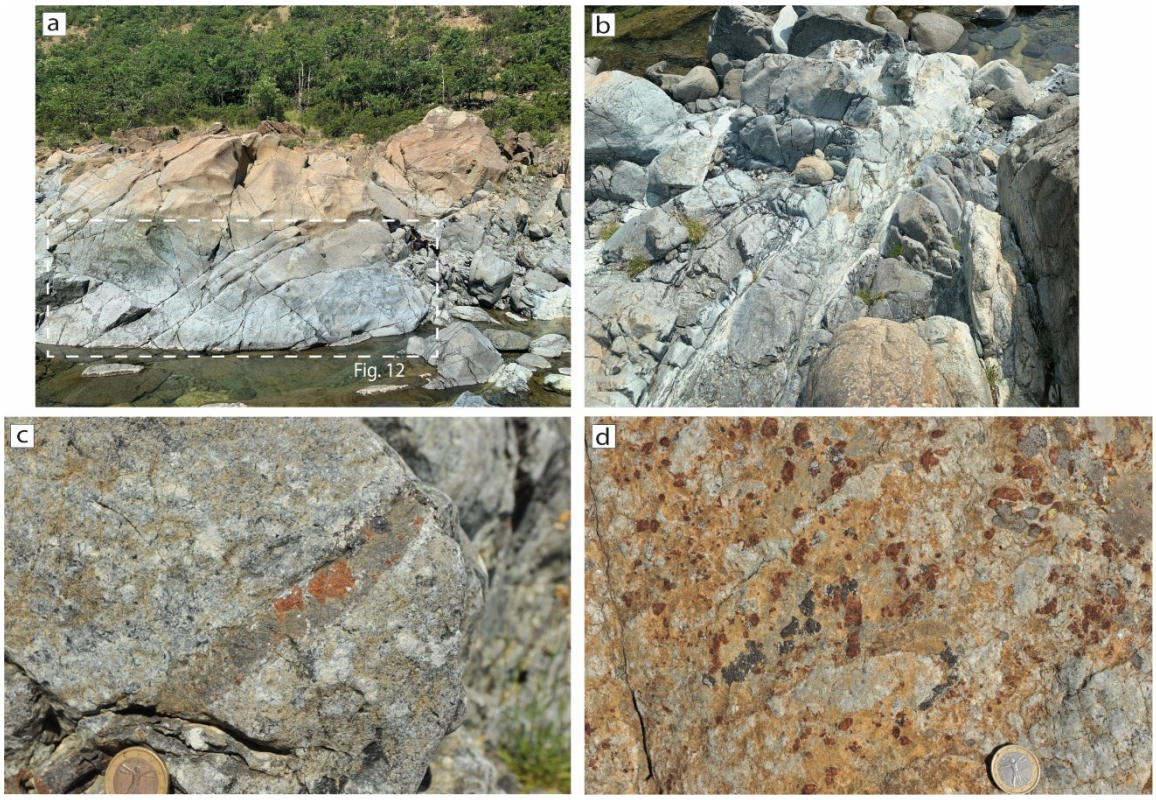

Figure 11. Field photographs of the structures outside the mapped area, displaying en-echelon veins and rodingitized dykes. a) overview of the area of Fig.6, characterized by en-echelon *Ol + Ti-chu* veins, b) rodingitized dyke dissecting the meta-peridotite, c) zoom of the *Ol+Ti-chu +Mt* veins dissecting the meta-peridotite, d) vein-parallel cross-section of a vein, showing mm-sized *Ti-chu* and *Mt* crystals.

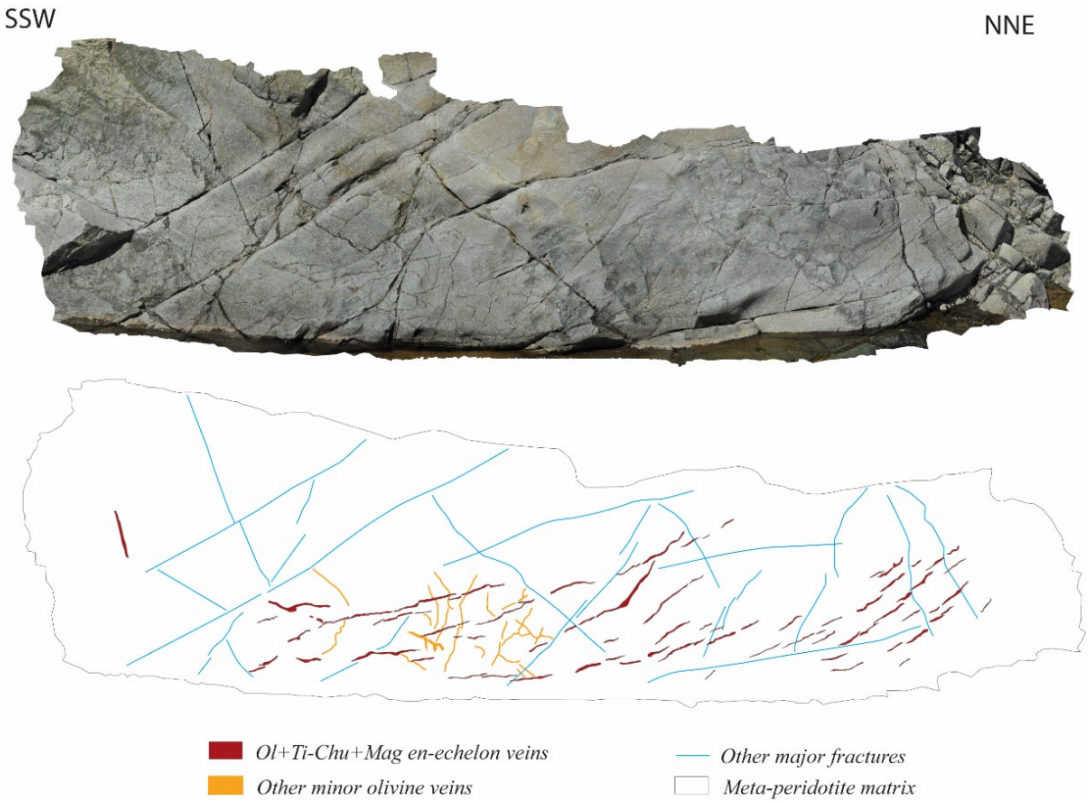

Figure 12. Orthophotograph and sketch of the area displaying the dominant set of right-stepping en-echelon veins. Other veins and fractures with different orientations are also skecthed.

5. Petrography and microstructural observations

Petrographic and microstructural observations were performed by optical and SEM microscopy on: (i) meta-peridotite containing *Ol* + *Ti-chu* reaction bands and veins, (ii) Ol-bearing serpentinite mylonite and (iii) meta-dunite.

5.1 Meta-peridotite (2139A)

The meta-peridotite largely consists of antigorite statically replacing mantle olivine and clinopyroxene, which are only locally preserved, The meta-peridotite hosts *Ol* + *Ti-chu* ± *Mt* reaction bands and veins and *Ol* + *Ti-chu* + *Di* (Diopside) + *C-chl* (Clinochlore) veins.

5.1.1 Meta-peridotite matrix

The antigorite matrix mainly consists of randomly oriented aggregates, characterized by an interpenetrative texture. Locally preserved mantle olivine and clinopyroxene (diopside, determined by Raman spectroscopy, Raman spectra in A1) exhibit brittle (fractures) and crystal-plastic (undulose extinction) deformation, respectively. The antigorite replacing mantle olivine forms rims of radiating coarse lamellae or occurs as fracture filling (Fig 13a, 13b). Clinopyroxene is replaced by antigorite along cleavage planes and at its rims (Fig. 13f). The clinopyroxenes have commonly a dusty appearance under the optical microscope (Fig. 13d), due to alteration to an ultrafine aggregate (not resolvable by any of the applied analytical techniques). EDS measurements on the antigorite replacing mantle olivine reveals a distinctive Al enrichment (see EDS spectra in the Appendix, A4). Locally, fine-grained olivine fills the largest fractures within mantle olivine relics.

The mantle olivine sites that are completely substituted by antigorite, show a median vein (a few tens of μm thick) of either antigorite or fine-grained olivine, surrounded by coarse orthogonal antigorite fibres (Fig 13h). Clinopyroxene sites are epitaxially overgrown by antigorite fibres and high-pressure diopside needles (Fig. 1g); locally, an intermediate stage of substitution of the mantle clinopyroxene by antigorite and high-pressure diopside is observed. In meta-peridotite, mantle spinel is replaced by magnetite rimmed by chlorite (*Chl*) (Fig. 13i).

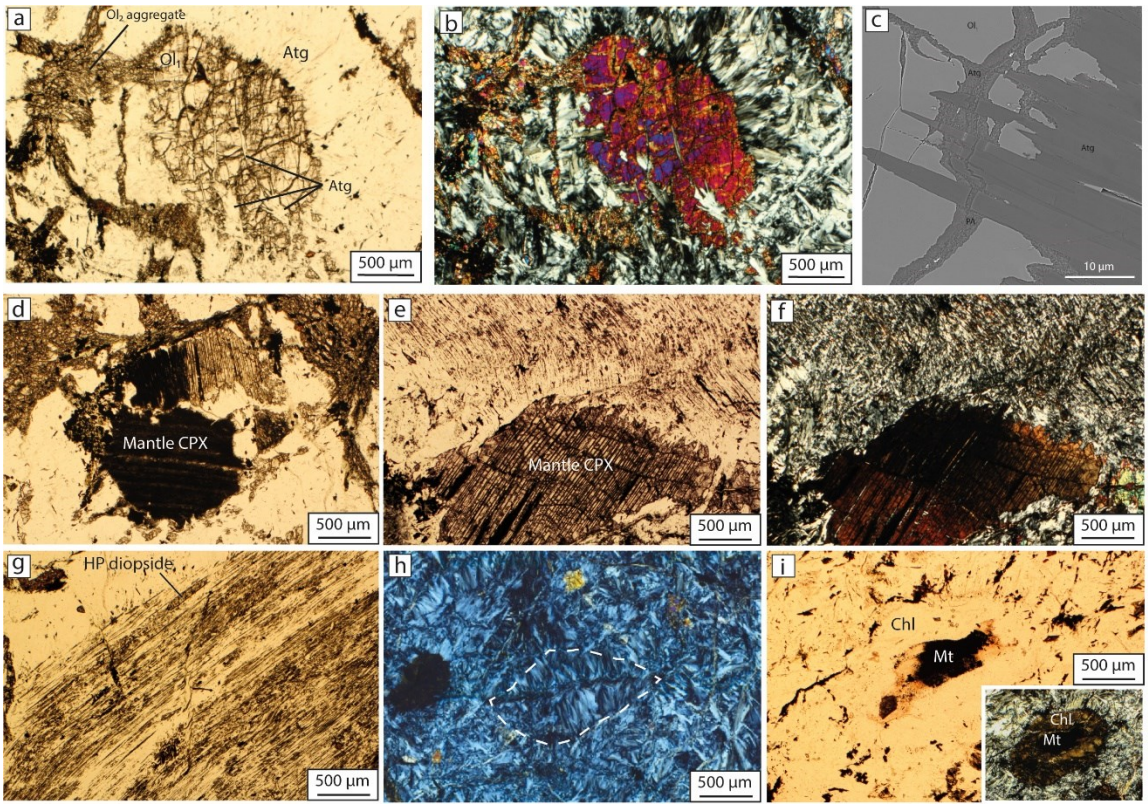

Figure 13. Microphotographs of the meta-peridotite matrix microstructures. a, b) Mantle olivine relict replaced by antigorite lamellae, radially at the rims, and along the fractures, c) BSE image, mantle olivine overgrown by antigorite lamellae and cut by microcracks containing antigorite (area in EBSD map *Smap3, subset 1*), d) mantle clinopyroxene relics locally altered to a ultrafine aggregate (dusty areas), e, f) mantle clinopyroxene displaying a cleavage and undulose extinction, with antigorite growth along the cleavage planes, g) former clinopyroxene site, high-pressure (HP) diopside needles and antigorite epitaxially replacing clinopyroxene, preserving its cleavage, h) former mantle olivine sites, completely replaced by antigorite lamellae with a median antigorite vein, i) coronitic structure after mantle spinel, magnetite core and chlorite rim, XPL microphotograph in the lower right corner.

5.1.2 The reaction bands

The meta-peridotite, studied in detail by SEM (sample 2139A), is characterised by a network of reaction bands made of metamorphic (high-pressure) olivine (*Ol_2*), with subordinate *Ti-chu* + *Mt* + *Brc* (brucite) + *Atg,* geometrically arranged to form subsets mutually oriented at ~40° and ~90°. *Ol, Ti-chu* and *Atg*-filled microcracks within the reaction bands are commonly arranged to define a fabric oblique to the band boundary. The fabric has an opposite obliquity in the cross-cutting sets of reaction bands, that suggests that the reaction bands actually form conjugate structures (Fig. 14a, 14b).

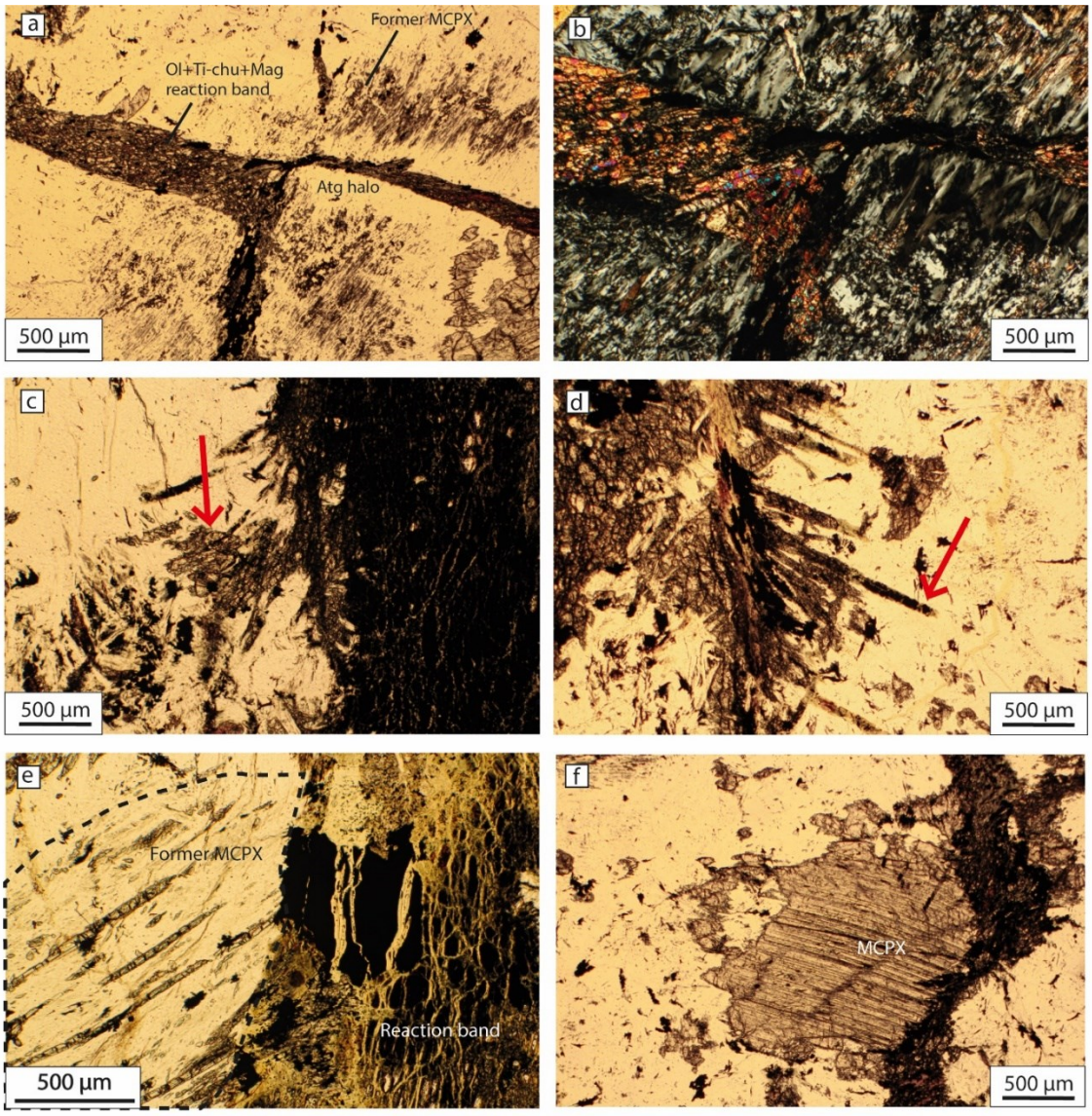

Figure 14. Microphotographs of the reaction bands microstructures. a) reaction band with sharp boundaries with an antigorite halo, dissecting the site of a former mantle clinopyroxene (MCPX), b) XPL microphotograph of the area in a), antigorite lamellae orthogonal to the reaction bands, oblique fabric defined by the *Ol, Ti-chu* and *Atg*-filling microcracks, c, d) olivine aggregates branching out from the reaction band (red arrows), e) reaction band dissecting a MCPX pseudomorphosed by *Atg* and high-pressure diopside, antigorite-lizardite (Raman spectra in the Appendix, A1) microcracks sub-parallel to the vein, f) reaction band dissecting a MCPX.

The metamorphic olivine in the reaction bands has, locally, specific relationships with the mantle relics. Preserved or pseudomorphosed mantle clinopyroxenes are often dissected by the reaction bands (Fig. 14f), which, in the latter case, are characterised by sharp margins and coarse orthogonal antigorite fibres forming a halo at the rims of the veins (Fig. 14a). Mantle olivine crystals are in several cases linked to the reaction bands through fine-grained olivine (Fig. 13a); this specific relationship was investigated by EBSD and is discussed in detail further in this section.

In most of the cases, the rims of the reaction bands are irregular, and Ol_2 crystals systematically branch out of the reaction bands, forming needles or fan-shaped aggregates (Fig. 14c, 14d).

In thin section 2139A, aggregates of Ol_2 + *Brc* + *Atg* + *Mt* occur at the intersection of reaction bands subsets (Fig. 15a). In these aggregates, different generations of antigorite were identified by coupled high-resolution BSE images and EDS measurements: (i) Al-rich antigorite (*Atg*) forming coarse lamellae (5-20 μm), either isolated or in aggregates (Fig. 15c), (ii) Al-free antigorite (Atg_2), filling microcracks dissecting Ol_2 grains and, (iii) Al-free nanometric, granoblastic antigorite (Atg_2) growing at the expenses of brucite and replacing Ol_2 (Fig. 15d). The former and the latter have reacted at the contact with brucite to form aggregates of nanometric olivine grains (Ol_3), reflecting the dehydration reaction $Atg + Brc \rightarrow Ol + H_2O$. Ol_3 was identified by EDS analyses yielding the characteristic MgO/SiO_2 ratio of olivine, despite the analysis was contaminated due to the fine grainsize of the grains (EDS spectra in Appendix A4). EDS analyses also confirmed the Fe-Mg zonation of the Ol_2 grains evidenced by different grey tones in BSE, that is characteristic of metamorphic olivine, in contrast with the compositionally homogeneous mantle olivine. Brucite, identified by Raman spectroscopy (see Appendix A2), in addition of the reaction with antigorite, shows a breakdown to porous patches (PB in Fig. 15c) where the Al-free antigorite (Atg_2) nucleates, commonly in association with magnetite (Fig. 15d, overview): this reflects the dehydration reaction $Brc + Si \rightarrow Serpentine + Magnetite + H_2O$ (*Frost & Beard, 2007*). The breakdown products are arranged in a pattern of sub-parallel domains within brucite, resembling cleavage planes and possibly suggesting the epitaxial growth of brucite over a former orthopyroxene. Brucite is present in these domains and within the Ol_2-rich reaction bands as either pure brucite or a mixture of brucite + antigorite (Fig. 16d). The antigorite + brucite aggregates (dark brown in cross-polarized light) were not indexed during EBSD analysis, due their highly heterogeneous and fine-grained texture, but were recognized by BSE and EDS.

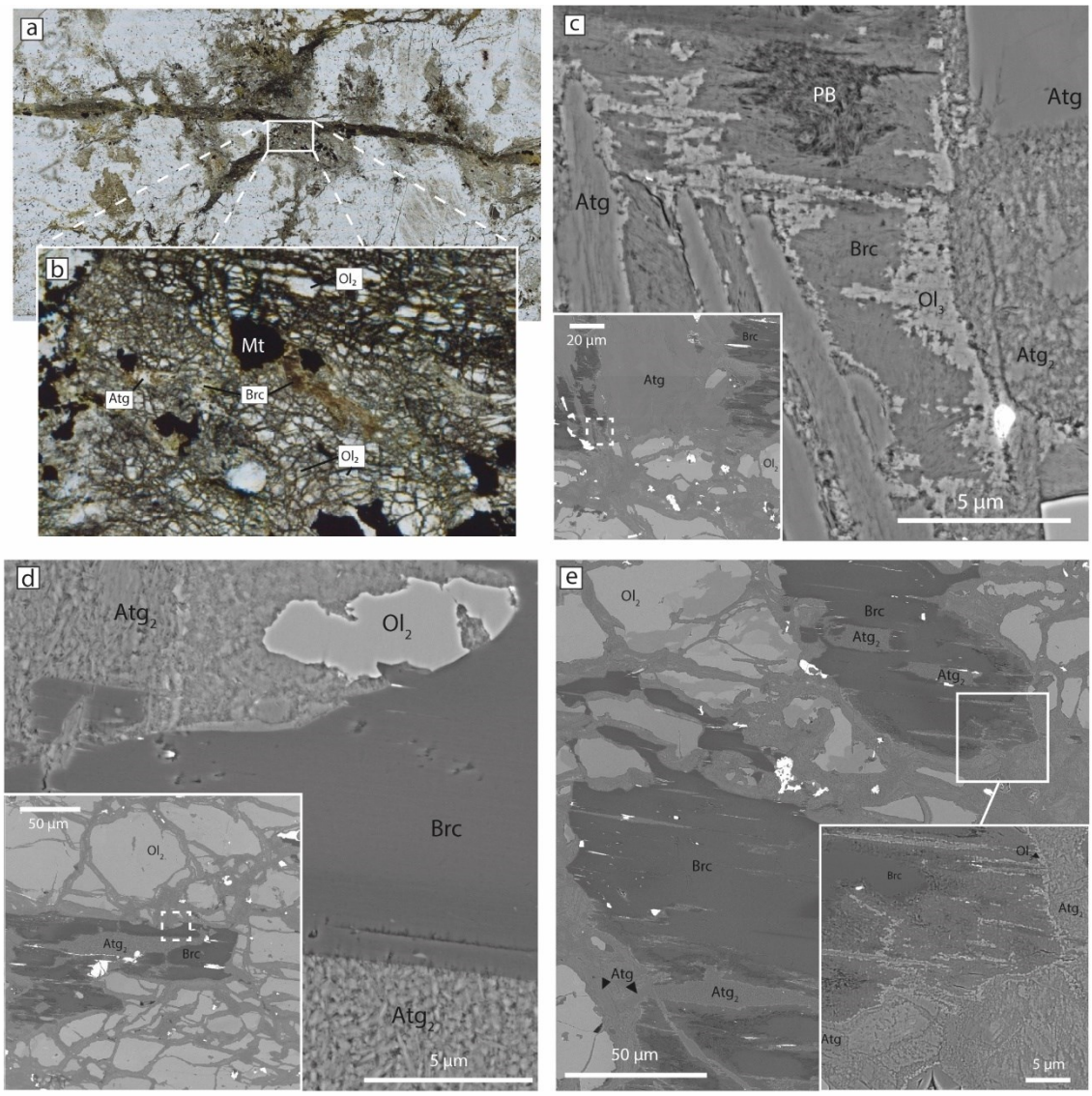

Figure 15. BSE images of the microstructures observed within the aggregates at the intersection of reaction band subsets. A) High-resolution thin section scan (sample 2139A), b) *Ol+Brc+Atg* aggregate at the intersection between reaction bands, area selected for SEM investigations. c) Nanometric Ol_3 grains nucleating at the contact between pure brucite (*Brc*) and both Al-rich *Atg* (Atg_1) and Al-free *Atg* (Atg_2); formation of the breakdown product of *Brc* (PB), site for Atg_2 nucleation. d) Atg_2 replacing *Brc*, localization of the area in the overview in the lower left corner, where Ol_2 grains are dissected by Atg_2 microcracks. e) Nanometric Ol_3 nucleating the contact between *Brc* and Atg_2.

High-resolution BSE and EDS analysis, performed on a radial aggregate of Ol_2 and on Ol_2 forming a reaction band, shows the presence of (i) Al-free antigorite (Atg_2) microcracks dissecting the Ol_2 grains (as also observed within the intersection Ol_2 + *Brc* + *Atg* ± *Mt* clusters), and (ii) nanometric (300-500 nm) olivine grains (Ol_3) nucleating along the Atg_2 microcracks, where Ol_2 was previously replaced by fibrous antigorite (Fig 16b). Formation of Atg_2 and Ol_3 therefore represents a new stage of hydration and

dehydration following the breakdown of *Atg* to Ol_2. In some areas, Ol_2 was completely substituted by Atg_2, leaving dark grey sites in BSE, where Ol_3 nucleates. The composition of Ol_3 was verified by EDS analyses. Ol_2 grains are dissected by intergranular and intragranular, cracks (5-10 µm in thickness) filled by Atg_2 + porous phase (likely unstable antigorite, PA in Fig. 16) ± *Mt* (± *Brc*). The presence of brucite within the microcracks was (i) inferred based on the observations on brucite-antigorite dehydration reported by *Nagaya et al. (2022)*, and on the similarity with the antigorite + brucite mixtures in BSE, and (ii) determined by EBSD analyses in other areas (*Smap2,* phase map in appendix A3). The microcracks dissecting Ol_2 are characterised by a systematic, symmetric pattern including from the centre to the border of the microcrack: (i) Ol_3, (ii) dark porous phase (DPA), likely made of *Atg* ± *Brc*, (iii) a light porous phase (likely containing antigorite, PA), and (iv) Al-free Atg_2 (Fig. 16e). The presence of antigorite within PA and DPA is suggested based on their MgO/SiO_2 ratio (EDS spectra in A4). Commonly, Atg_2 contains a light, porous inner band which is, likely, the breakdown product of Atg_2 from which Ol_3 nucleates. Locally, Al-rich euhedral antigorite lamellae are present within the cracks (Fig. 20c).

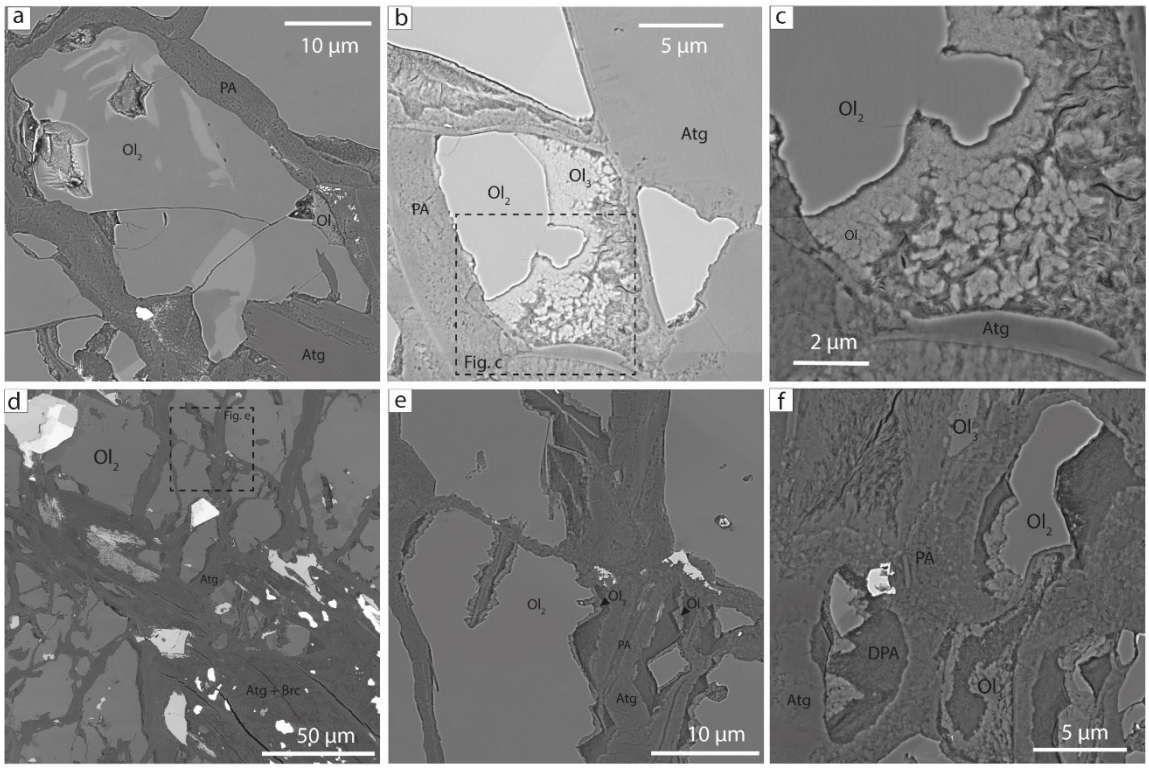

Figure 16. BSE images of reaction bands microstructures. a) Strong Fe-Mg zonation of Ol_2, dissected by PA and Atg_2-filling microcracks. b) Nanometric Ol_3 grains nucleating within a former Ol_2 site previously replaced by antigorite; the different Ol_2 sites belong to the same crystal, dissected by the microcracks constituted by porous antigorite (PA) and Atg_2. c) Detail of b). d) Overview displaying the *Atg*+*Brc* mixture, zoned Ol_2 grains dissected by antigorite-bearing

microcracks. e) Detail of d), systematic internal structure characterizing the microcracks. f) Ol_3 nucleating within Ol_2 sites, growing from the dark porous antigorite (DPA).

These microstructures were further investigated by EBSD, especially to analyse metamorphic olivine (Ol_2) and its relationship with mantle olivine (Ol_1). With this purposes, four EBSD maps were acquired on thin section 2139A (Fig. 17).

The crystallographic orientation of Ol_2 is represented in the inverse pole figures and pole figures of figures 18 and 19 and compared with the crystallographic orientations of mantle olivine (Ol_1) in figures 21 and 22.

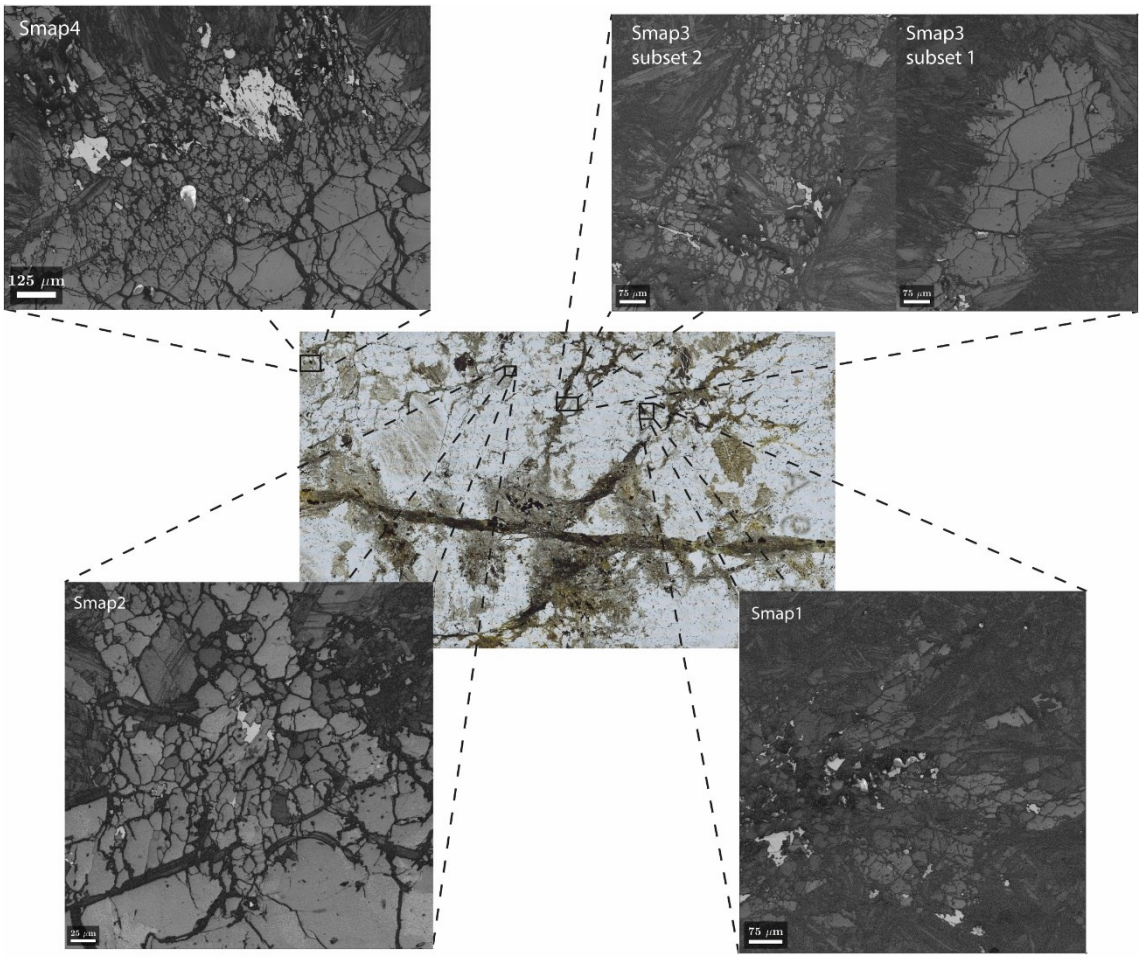

Figure 17. Location of the EBSD maps (*Smap1, SMap2, Smap3, Smap4*) acquired on thin section 2139A.

EBSD maps were acquired on a radial aggregate of Ol_2 (*Smap1*) and on a section of a reaction band (*Smap3, subset 2*). In these maps, the zoned Ol_2, ranging in grainsize from 20 to 100 µm is dissected by the Atg_2 microcracks (Fig. 20c). Inverse pole figures do not evidence a CPO for Ol_2, however, pole figures (lower hemisphere projection), reveal a

weak clustering of the *Ol*$_2$ orientations (Fig. 18, 19), which is more pronounced for the reaction band than for the radial aggregate.

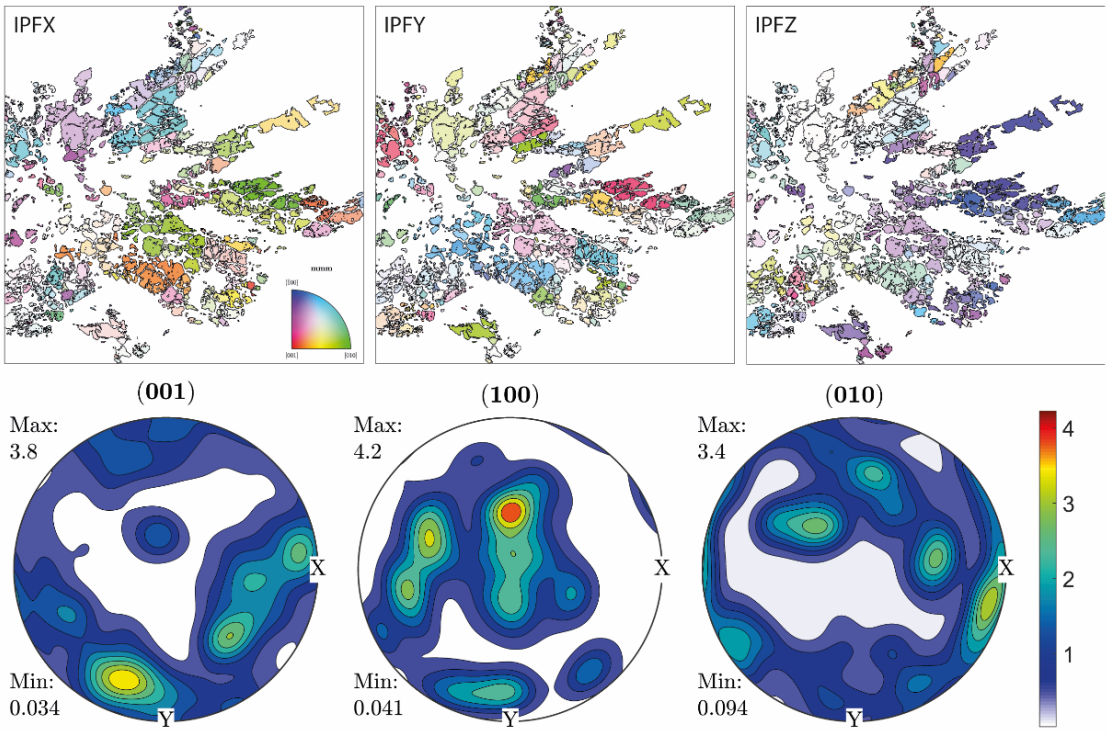

Figure 18. *Smap1* EBSD data. Above, X, Y, Z inverse pole figures. Below, pole figures indicating only a weak clustering of *Ol*$_2$ crystallographic orientations.

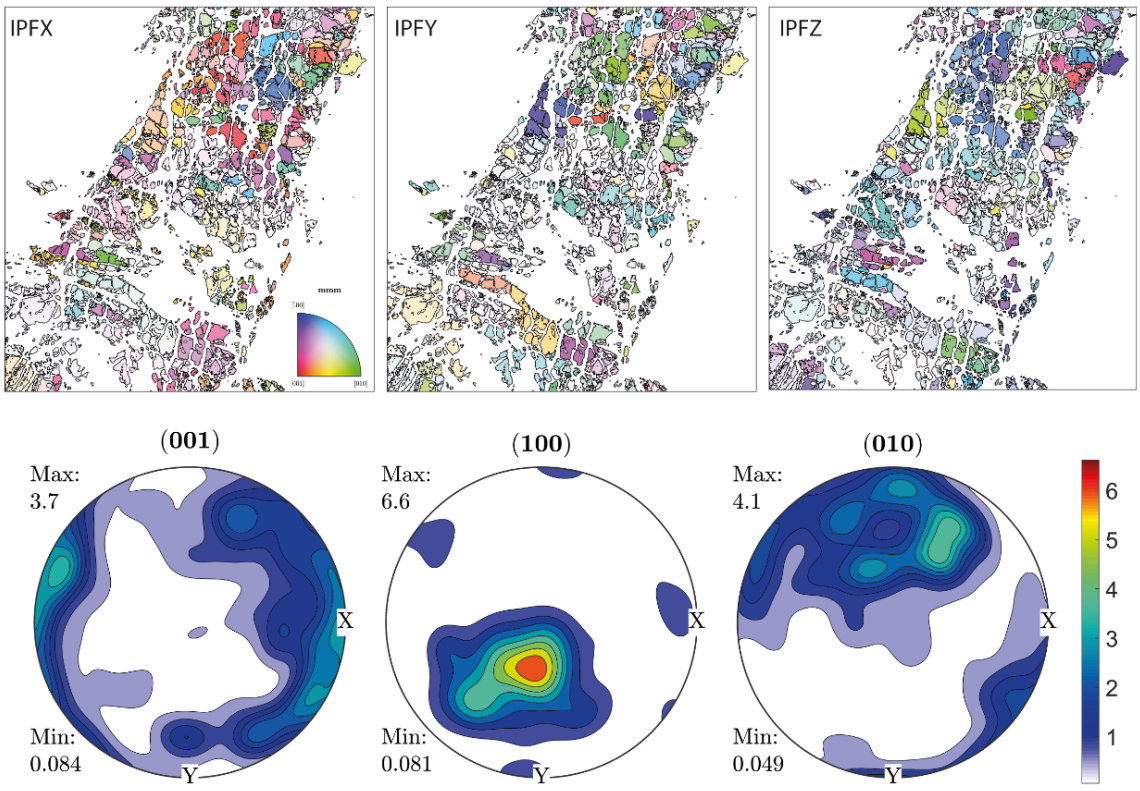

Figure 19. *Smap3, subset 2* EBSD data. Above X, Y, Z inverse pole figures, below pole figures showing a weak iso-orientation of *Ol*$_2$ grains.

In some domains, the Ol_2 reaction bands are in close contact with mantle olivine (Ol_1) relics. EBSD maps (*Smap2* and *Smap4)* acquired at the contact between Ol_1 and Ol_2, indicate that Ol_2 grew in epitaxial continuity with Ol_1. In the pole figures (Fig. 21), the crystallographic axes of the two generations of olivine plot in the same regions defining a maxima. A weak decrease in the iso-orientation between Ol_1 and Ol_2 with distance from the mantle olivine in *Smap2* and *Smap4* is visible from the inverse pole figures (Fig 21). In these domains, both Ol_1 and Ol_2 grains are dissected by microcracks filled with Al-free antigorite (Atg_2) + *Brc*, where brucite commonly occurs in association with magnetite (phase map Smap2 in appendix A5). These relationships suggest a stage of hydration of Ol_2 along these cracks, through the reaction $Ol + H_2O \rightarrow Serpentine + Mag + Brc$ (*Frost & Beard, 2007*). In *Smap1* and *Smap3 (subset 2)* brucite was not indexed along the cracks, either due to the bigger step size set for the maps acquisition, or to its consumption by the reaction $Brc + Si \rightarrow Serpentine + Mag + H_2O + H_2$ (*Frost & Beard, 2007*). From the pole figures, similar orientations for olivine were obtained from the two maps, where the olivine *a*-axes define a maxima between Y and Z directions, the *b* and *c*-axes plot at 90° creating a maxima between X and Y. The same pattern was recognized in *Smap3* (Fig. 22c), suggesting a CPO for mantle olivine.

In *Smap2* a brucite crystal (around 60 μm large) localized within Ol_2 grains in association with magnetite, shows a peculiar relationship with Ol_2 zonation. Brucite is locally present within Fe-poor domains (dark grey in BSE) of Ol_2 grains, while it is absent in Fe-rich domains (light grey in BSE). In detail, the brucite grown close to the contact between Fe-poor and Fe-rich domains, have a sharp termination at the boundary between the two domains (Fig. 20d).

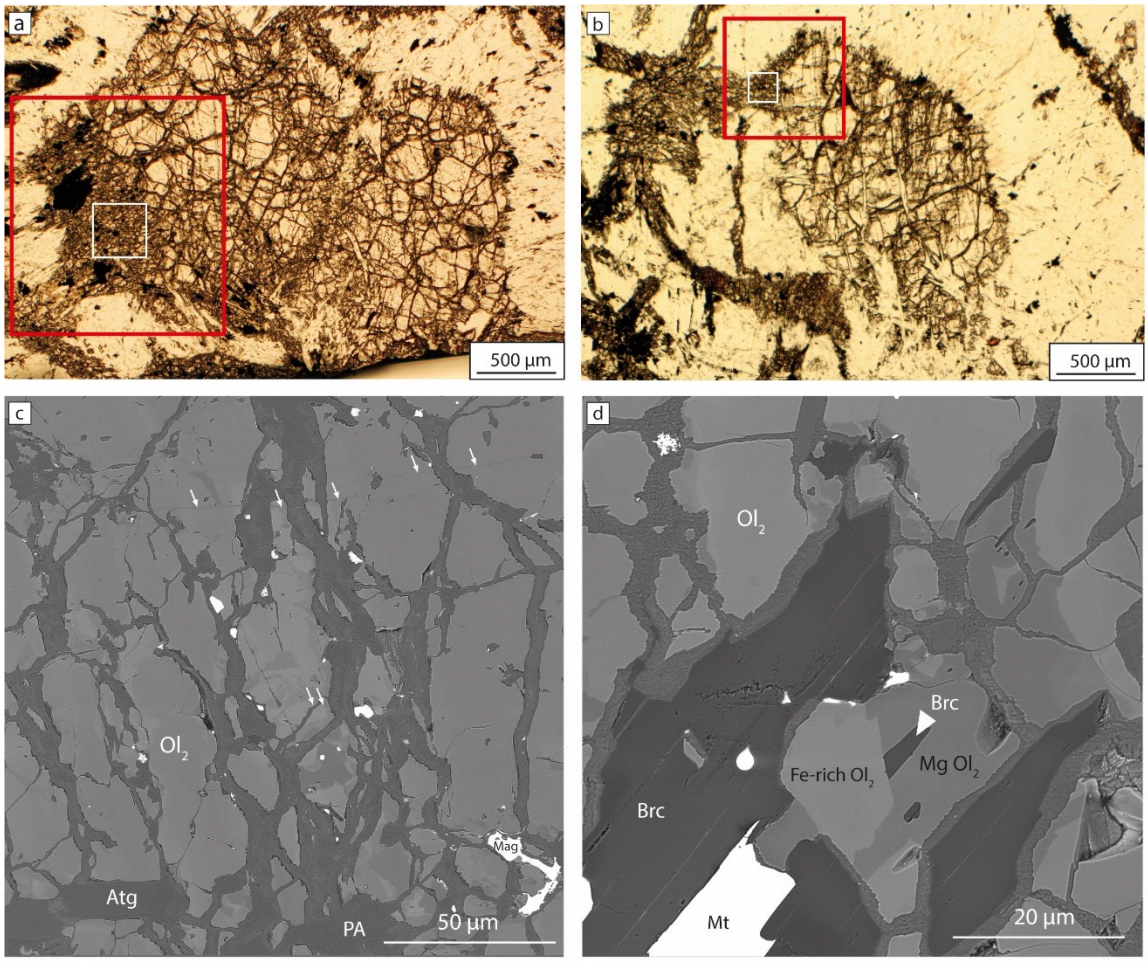

Figure 20. a, b) Mantle olivine relict with fine-grained olivine (Ol_2) growing within the red rectangles (*Smap4* and *Smap2* areas respectively); areas within the white rectangle in BSE images of c) and d) respectively. c) Strong zonation of Ol_2 dissected by the microcracks (white arrows); Atg_1 lamellae are locally present along the microcracks. d) Brucite associated with magnetite (*Mt*) replacing *Ol*; *Brc* present within Mg zonations of Ol_2, absent from the Fe-rich domains, with which it creates a sharp boundary.

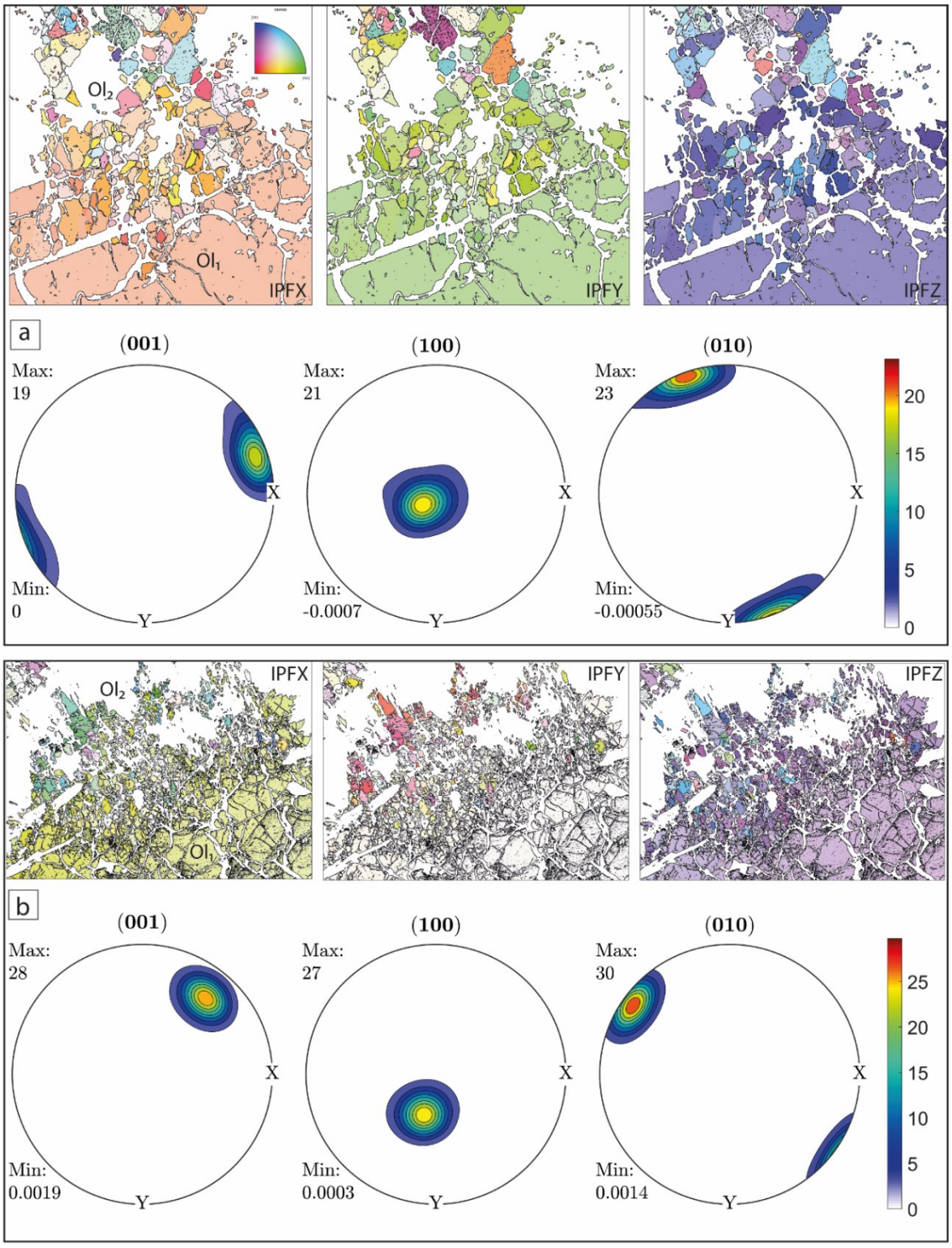

Figure 21. Orientation of *Ol₁* and *Ol₂* from *Smap2*, X, Y, Z inverse pole figures and pole figures, b) Orientation of *Ol₁* and *Ol₂* from *Smap4*, X, Y, Z inverse pole figures and pole figures.

The same pattern, indicating consistent orientation of the two olivine generations, can be observed in *Smap3* (Fig. 10). Comparison between the inverse pole figures and the pole figures obtained from *Smap3 (subset 1)* and *Smap3 (subset 2)*, acquired on an *Ol₁* relic and on a section of the neighbouring reaction band respectively, indicates, also in this

case, a control on the reaction band-forming Ol_2 of the isolated Ol_1 crystal, even without a direct contact between the two generations of olivine (Fig. 22). In fact, Ol_2 orientations (*subset 2*) in pole figures define girdles around the maxima related to the mantle olivine porphyroclast orientation (*subset 1*).

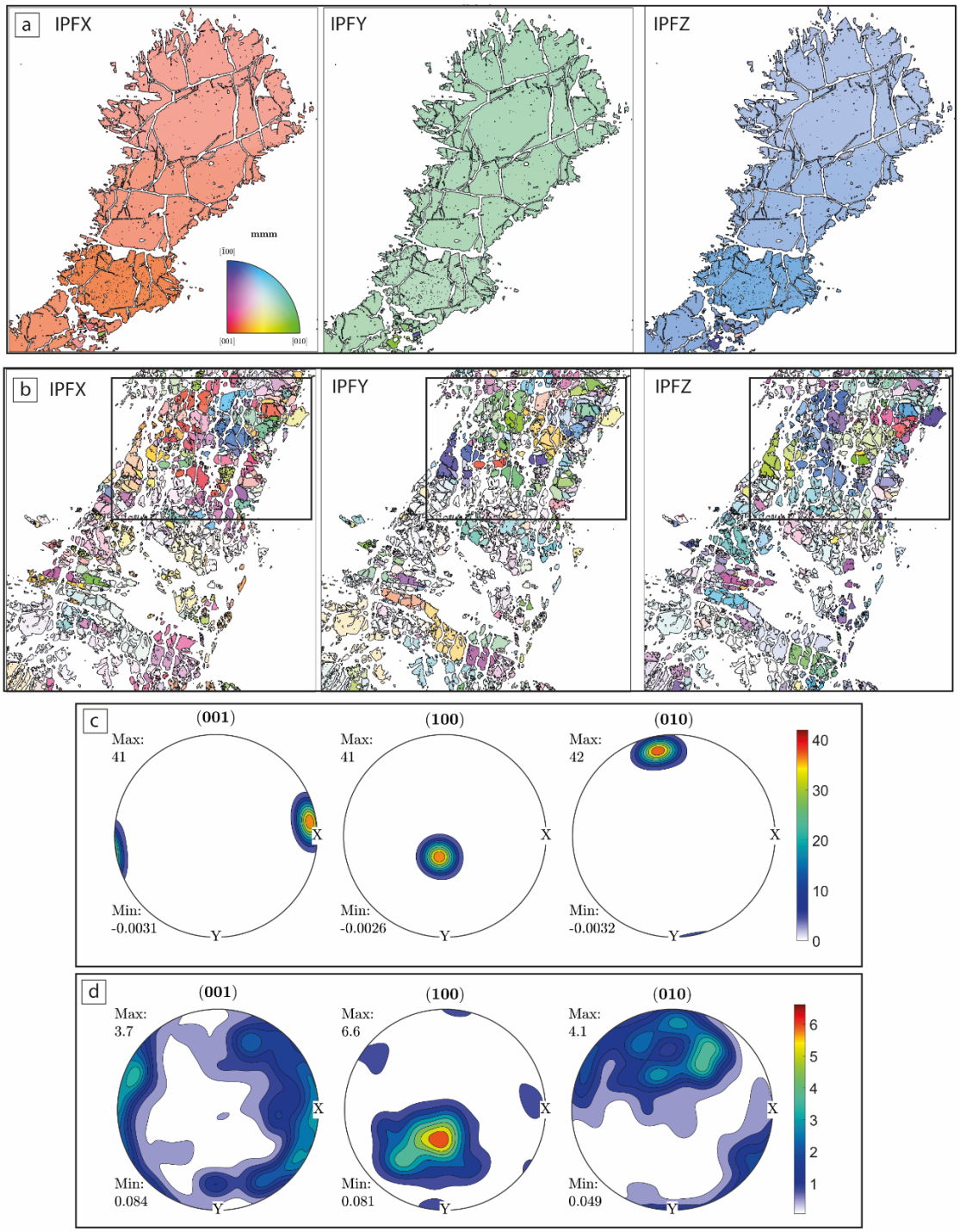

Figure 22. a) X, Y, Z inverse pole figures of mantle olivine (*Smap3, subset 1*), b) X, Y, Z inverse pole figures of a neighbouring reaction band (*Smap3, subset 2*). From the inverse pole figures Ol_2 crystals displaying the same orientations as the Ol_1 can be identified within the black rectangle in b). c) Pole figures of Ol_1 in a), d) pole figures of Ol_2 forming the reaction bands in b).

Considering the systematic presence of antigorite rims around mantle olivine relics, EBSD analysis was also performed on the Al-rich radial antigorite (*Smap2, Smap3, Smap4*), despite the low-quality indexing caused by the structure of antigorite. In pole figures a maxima related to the *c*-axes indicates that the antigorite fibres are always oriented with the basal hexagon parallel to the X-Y plane, orthogonal to the Z direction. *a*- and *b*-axes, instead, are oriented parallel to the X-Y plane of the sample, reflecting the radial arrangement of the antigorite fibres. *Smap1* was not considered due to the very poor indexing of antigorite.

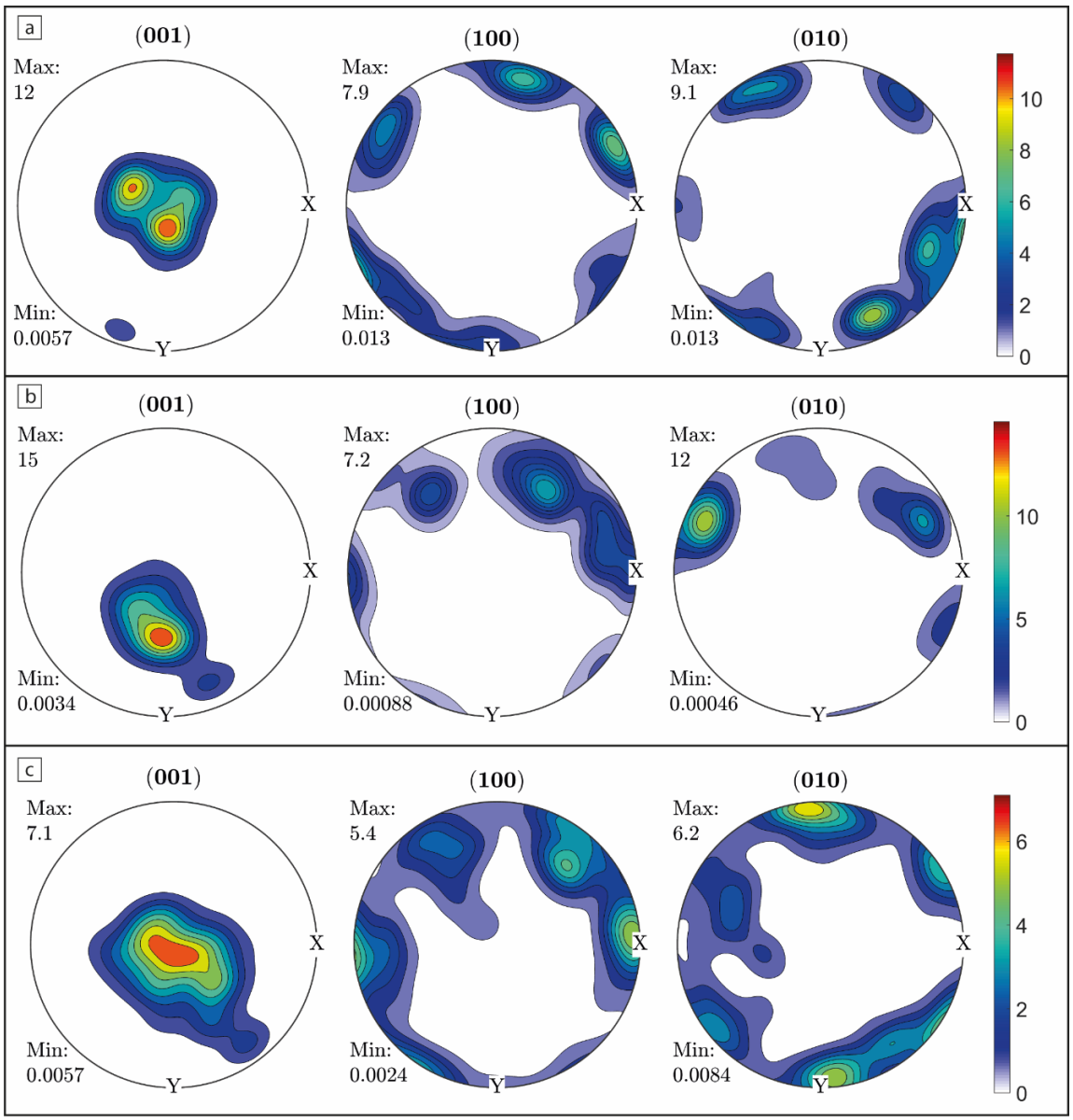

Figure 23. EBSD data of the radial *Atg* lamellae replacing Ol_1 from a) *Smap2*, b) *Smap3*, c) *Smap4*, with *c*-axes defining a maxima and *a*-axes and *b*-axes parallel to the X-Y plane, reflecting the radial arrangement.

5.1.3 The high-pressure veins

The meta-peridotite sample collected in the southern part of the outcrop (2245) displays nicely preserved sets of cross-cutting sets of high-pressure veins (Fig. 24). A main cm-thick vein (V1) contains cm-sized crystals of Ol_2, *C-Chl* (Clinochlore), *Ti-chu*, *Mt* and *Di* (Fig. 25a) and runs parallel to an antigorite vein (V2) which is dissected by *Ol* + *Ti-chu* mm-thick veins (V3) (Fig. 25g). V3 comprises a set of en-echelon veins conjugated to V1 suggesting a sinistral shear sense. The rims of V3 veins are characterized by vein-parallel cracks of antigorite (Fig. 25d), which also cross-cut the inner part of the veins, as in V1, and that are locally spatially denser. The very contact between V1 and the V3 is sealed by magnetite, antigorite, and fine-grained olivine (Ol_s) forming an oblique fabric, which suggests sinistral shearing (Fig. 25e). The rims of V1 are decorated by antigorite fibres growing orthogonally to V1, locally sheared consistently with the en-echelon geometry and the oblique fabric displayed by Ol_s (Fig. 25c). V2 is an antigorite vein which splits in 2-3 veins in some areas (Fig. 25f) and which contains aggregates of µm-sized granoblastic olivine and *Ti-chu*. The described structures are finally dissected by late calcite and chrysotile veins (Fig. 25h).

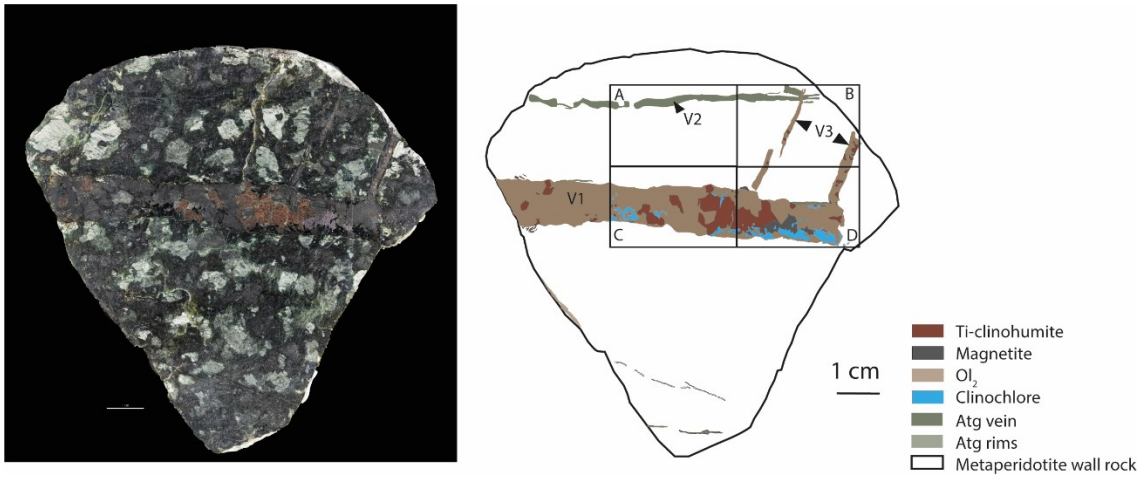

Figure 24. Locations of thin sections obtained from sample 22-45.

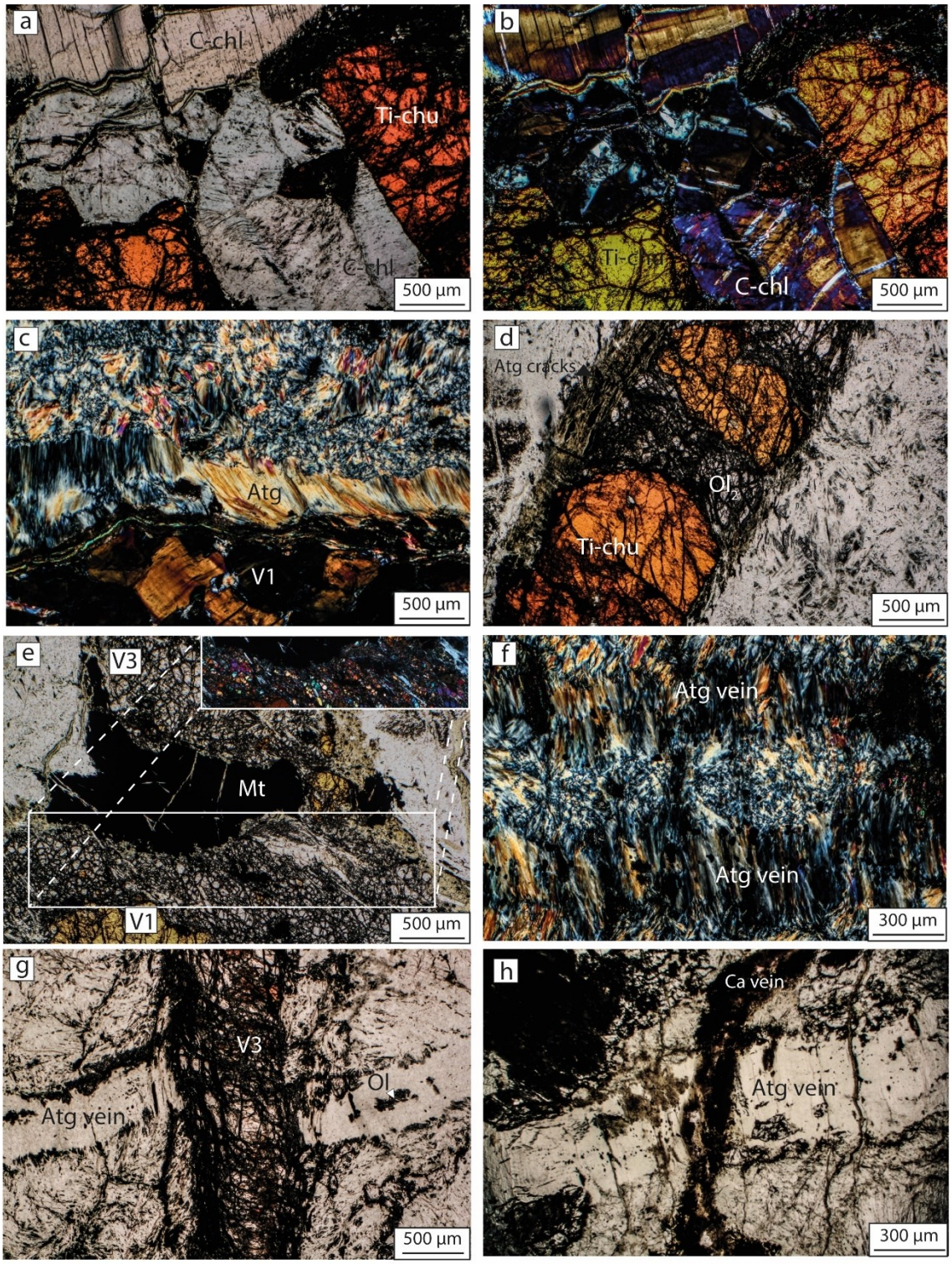

Figure 25. Microphotographs of thin sections from sample 22-45. a, b) PPL and XPL microphotographs of the *Ti-chu* and *C-Chl* in V1, thin section 22-45D, c) antigorite lamellae at the rim of V1, thin section 22-45D, d) *Ti-chu* and *Ol* forming a V3 vein, with vein-parallel microcracks of antigorite, thins section 22-45B, e) contact between V1 and V3 veins, sealed by *Mt, Atg* and fine-grained *Ol* arranged to form an oblique fabric, thin section 22-45D f) antigorite veins (V2) in XPL, g) *Atg* vein containing *Ol* aggregates and dissected by a V3 vein, thin section 22-45B, h) antigorite vein dissected by a late calcite vein, thin section 22-45A.

5.2 Mylonite (2138A)

The sample 2138A consists of a meta-peridotite mylonite located at the boundary between the meta-peridotite hosting the reaction bands (section 5.1, sample 2139A) and the meta-dunite (section 5.3, sample 2138B). The S-C foliation of the mylonite and the asymmetric shape of clinochlore and clinopyroxene porphyroclasts indicate a sinistral shear sense (Fig. 26d, 26g). Mantle olivine porphyroclasts, locally affected by undulose extinction, are wrapped around by the foliation, forming pressure shadows hosting antigorite and metamorphic, fine-grained olivine (Fig. 26a, 26b, 26c). Metamorphic olivine and Ti-clinohumite layers (similar to the reaction bands in meta-peridotite) also delineates the foliation (Fig. 26e). This foliation marked by olivine planes parallel to the mylonitic foliation, is referable to the OlF2 detected in the field. OlF2 has gradual boundaries with the mylonitic matrix and is deformed with an opposite shear sense with respect to the hosting mylonite. Mantle olivine relics are statically overgrown by antigorite (Fig 26c), likely in relation to a later stage of serpentinization than the antigorite forming the foliation. Late veins of chrysotile and calcite dissect the mylonitic foliation (Fig. 26f) (Raman spectra reported in the Appendix A1, A3).

5.3 Dunite (2138B)

Sample 2138B is mostly made of mantle olivine pervasively serpentinized along a closely-spaced sets of subparallel antigorite-chrysotile veins. Minor domains were affected by static serpentinization, where olivine was completely replaced by antigorite displaying an interpenetrative texture. Coronitic structures of *Mt* and *Chl* after mantle spinel, surrounded by statically grown antigorite, are common (Fig. 27b). Locally, 3 mutually cross-cutting generations of serpentine veins can be distinguished: (1) fine-grained, antigorite with interpenetrative texture, (2) antigorite veins, (3) antigorite – chrysotile veins (identified by Raman: see Appendix A1) cross-cutting (2) at an angle of around 70° (Fig 27a).

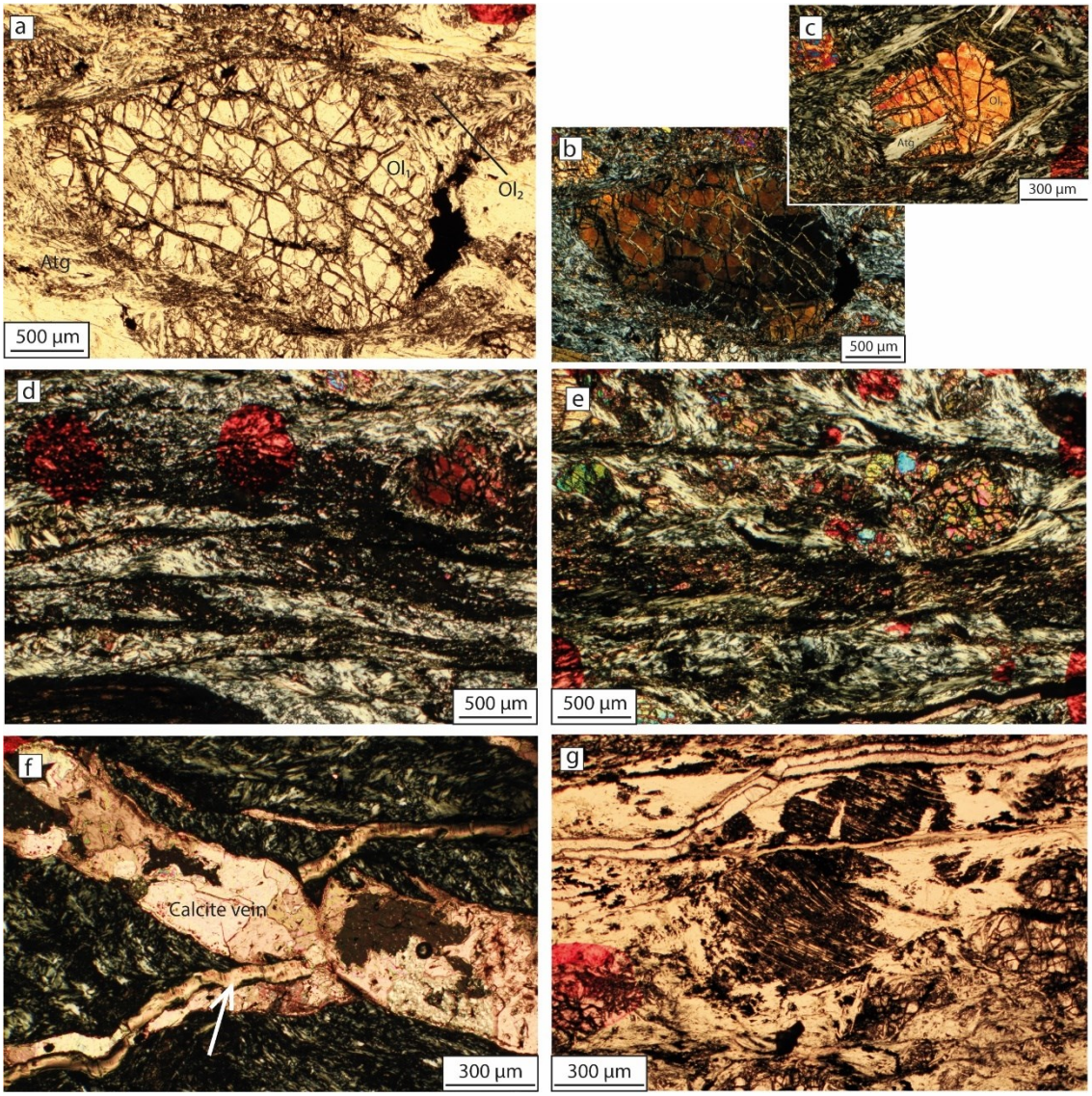

Figure 26. Mylonite microphotographs. a) Fractured mantle olivine porphyroclast, decorated at the rims and in the pressure shadows by fine-grained *Ol* and antigorite; fractures filled by serpentine. b) XPL optical image of the area in a), evidencing the mantle olivine undulose exctinction. c) XPL microphotograph of a mantle olivine porphyroclats statically replaced by antigorite lamellae. D) mylonitic S-C type foliation., e) *Ol* + *Ti-chu* band parallel to the foliation, identified as OlF2. F) late chrysotile vein dissected by a calcite vein, g) former mantle clinopyroxene mineral fishes within the foliation.

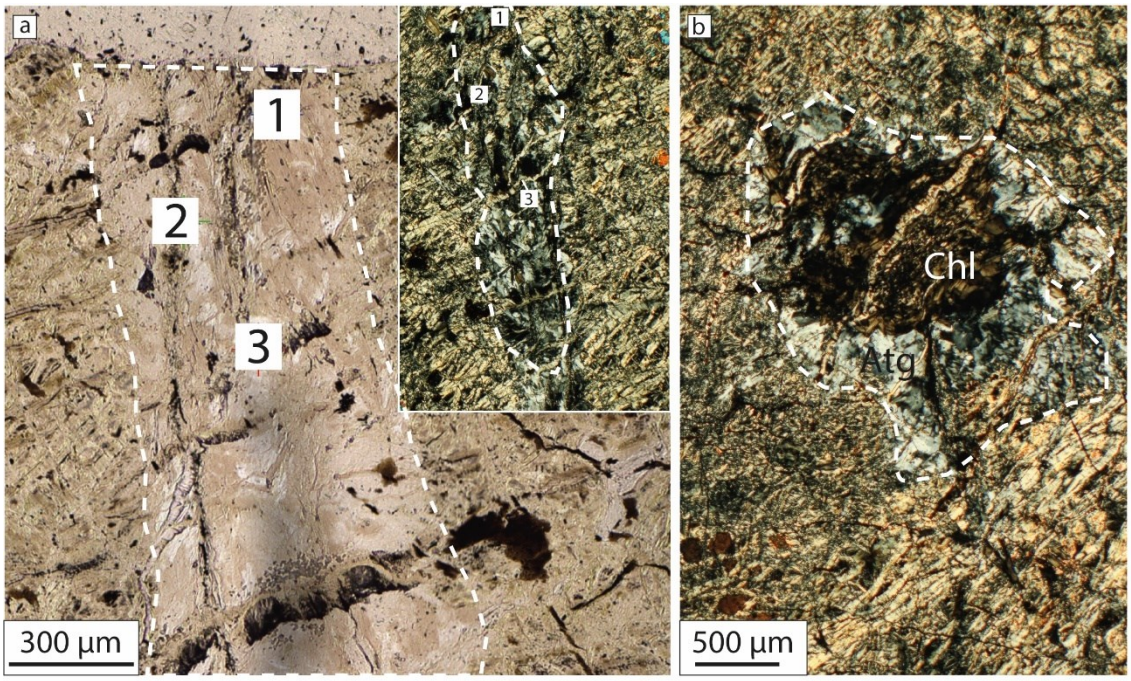

Figure 27. Meta-dunite microstructures. a) 3 mutually cross-cutting antigorite generations, b) *Mt – Chl* coronitic structure surrounded by an antigorite rim, dissected by the main set of veins. In a) a statically grown antigorite (1) is dissected by an antigorite vein (2) and finally by the main set of veins.

6. LA-ICP-MS: Trace element analyses

Trace element concentrations of the main minerals contained in the different structural elements were analysed, to constrain the sources of the fluids involved in the different stages of deformation. Fluid mobile elements (*B, Li, As, Sb, Sr, Ba, W*), were especially considered for *Ol, Ti-chu* and *Atg*, as tracers of fluid-rock interactions occurring during *Ol*-forming antigorite dehydration reactions in subducted serpentinites.

6.1 Antigorite generations composition

The two main antigorite generations – Al-rich (Atg_1) and Al-free (Atg_2) antigorite– display the same trace elements composition in both the analysed samples (2139A and 2245), which is summarized hereafter.

Atg_1 is characterized by significant concentrations of *B* (5-25 µg/g) and is depleted in *Li, As* and *Sb*, with values generally below the detection limits (LoD). However, 3 different measurements provided an *Sb* concentration of 0.073 µg/g and *As* contents of around 0.3µg/g. The content of the remaining FMEs is moderate, with *Sr* concentrations of 0.1-1.2 µg/g, *W* within the range 0.005-0.3 µg/g, and *Ba* contents of 0.031-1.7 µg/g.

Atg_2, present within the microcracks and replacing brucite, contains, conversely, very high *B* concentrations (35-190 µg/g). It also enriched in *Sr* (3.2-5.7 µg/g), *W* (0.28-0.73 µg/g) and *Ba* (1.7-8.5 µg/g). The few *Sb* values above the LoD reveal an enrichment in this element with respect to Atg_1, with a concentration of 0.21-0.56 µg/g. *As* data, conversely, are always below the LoD.

Despite the majority of *As* and *Sb* measurements being below the LoD, these values were considered to create *As* vs *Sb* plots. *As* and *Sb* systematics are used to compare the compositions of the two generations of antigorite with the data proposed by Cannaò et al. (2016), that uses *As* and *Sb* systematics to deduce infiltration of sedimentary and crust-derived fluids within the high-strain domains of the Voltri Massif, which are enriched in these elements with respect to the bulk low-strain domains, conversely not affected by the interaction with the external fluids. In this study, the values of the detection limits are treated as maximum values, and the reliability of the plot for the interpretation is guaranteed by the few values above the LoD measured for the Atg_2. Figure 32a shows that the Atg_1 plots in correspondence to the low-strain domains of the Voltri Massif, while

the Atg_2 in correspondence to the high-strain domains. The fact that most of the Atg_1 has concentrations below the LoD is negligible, since the evident difference between the two generations, would be even larger in the case of lower values.

Based on the work by Peters et al. (2017), *Cs* content and the *Cs/Yb* ratio of the different antigorite generations were considered to unravel the previous hydration environment of this unit. The *Cs* content of both generations ranges between 0.03 and 0.37 μg/g, while the *Cs/Yb* ratio ranges between 0 and 15, as visible in the diagram in Fig. 32c.

6.2 Mantle relics

Trace element concentrations of mantle relics were measured in both the investigated samples, for comparison with the composition of the high-pressure counterparts. Mantle olivine contains: (i) *B* concentrations below LoD (Fig. 32d), (ii) low concentrations of *W* (0.0046 μg/g) and *Ba* (0.025-0.096 μg/g), (iii) *Sr* concentrations in the range 0.06 - 0.8 μg/g. Mantle clinopyroxenes contain: (i) *B* concentrations in the range 4 - 16 μg/g, (ii) slightly higher *Ba* contents with respect to the mantle olivine (0.7-4 μg/g), and (iii) *W* concentrations in the range 0.0061 - 24 μg/g. The pseudomorphic chlorite after spinel is slightly enriched in *B* (7.23-9 μg/g) and *Ba* (1.35-3 μg/g). *Cs* within the chlorite is present in minor amount (0.042 μg/g), as *W* (0.011-0.0038 μg/g) and *Pb* (0.028 μg/g). *As* and *Sb* are below the LoD for all measurements. *Li* concentrations are in the range 1.2 - 2 μg/g.

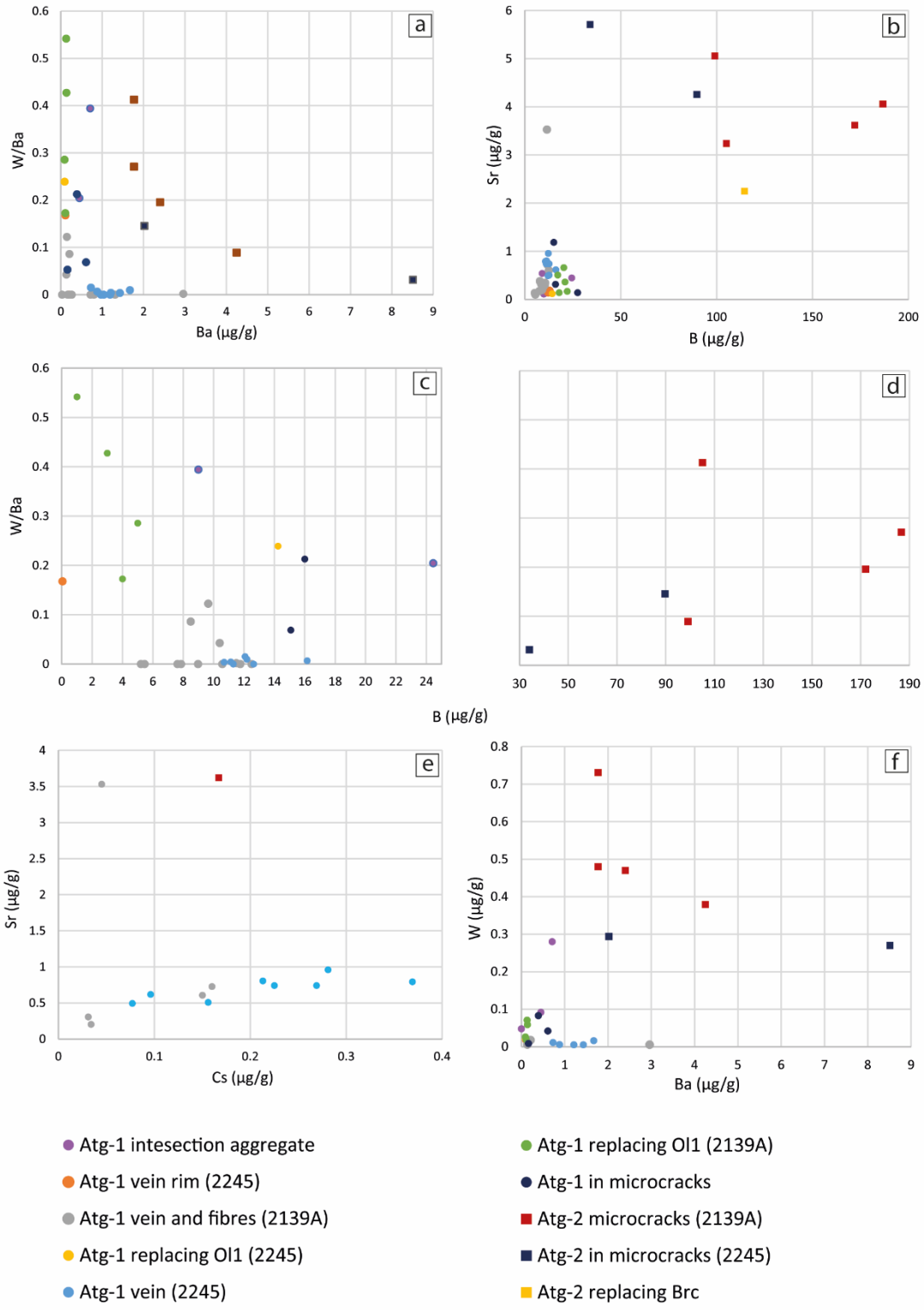

Figure 28. Fluid-mobile element enrichment plots for antigorite of different generations, sites and samples. The intersection aggregate refers to Fig. 15b. *Atg*-1=Al-rich antigorite, *Atg*-2=Al-free antigorite. Legend for all plots below, sample indicated in brackets where ambiguous. a)*Ba* vs *W/Ba*, b) *B* vs *Sr,* c) *B* vs *W/Ba* for Atg_1, d) *B* vs *W/Ba* for Atg_2, e) *Cs* vs *Sr*, f) *Ba* vs *W*.

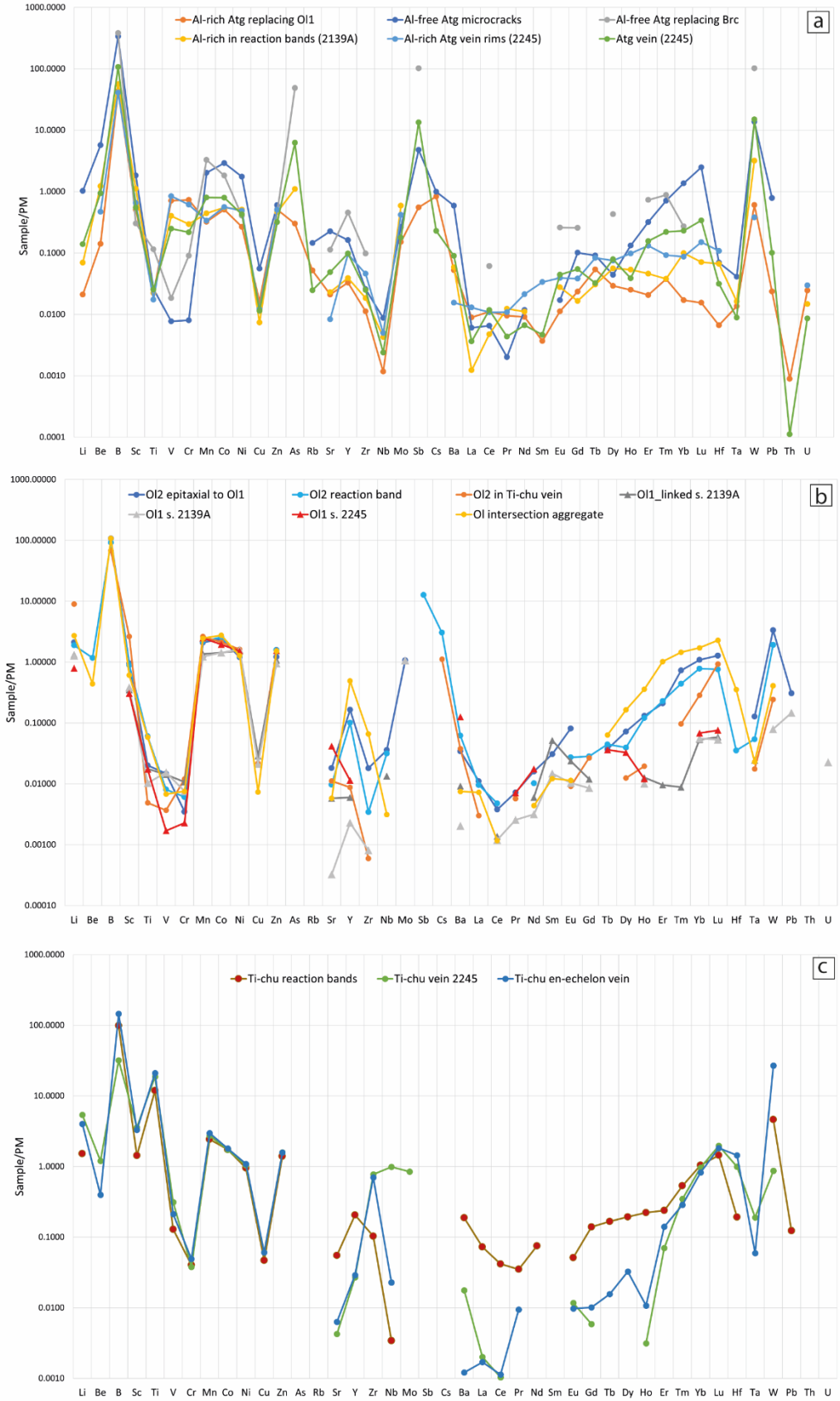

Figure 29. Primitive mantle normalized trace elements distribution diagrams of a) antigorite, b) olivine, c) Ti-clinohumite generations within samples 2139A and 2245. Primitive mantle (PM) values after Mc Donough and Sun (1995).

6.3 Reaction bands (2139A)

The Ol_2 constituting the reaction bands contains significant amounts of *B* (19-38 μg/g), clearly distinguished from the B-free Ol_1 (section 6.2). Only one measurement provided *Sb* concentrations of 0.35 μg/g, while As contents are systematically below the LoD. In addition, *W* and *Sr* contents in the range 0.073-0.4 μg/g and 0.13-0.56 μg/g, respectively, place the metamorphic olivine at intermediate FMEs enrichments between the Al-rich and the Al-free antigorite, as shown in Fig. 32d. The amount of *Sr* does not vary between Ol_1 and Ol_2. The *Ba* concentrations ranges between 0.09 and 1.09 μg/g, *Li* concentrations between 2.5 and 6 μg/g was observed (Fig. 30).

As in the case of antigorite, *As* vs *Sb* plots were considered for the olivine (Fig. 32b), using the values of the detection limits as maximum values. The metamorphic olivine of the reaction bands appears to cluster in composition in correspondence to the Voltri Massif high-strain domains, affected by infiltration of sedimentary-derived fluids, while the mantle olivine and the olivine present within the intersection cluster plot in correspondence to the low-strain domains. In this case, however, statistically more robust data are needed for more reliable inferences on fluid sources, since only one value was above the LoD.

The *Ti-chu* included in the reaction bands is characterized by concentrations: in the range of 28.8-30.5 μg/g for *B*; in the range 0.62 – 1.57 μg/g for *Sr*; 1.24 μg/g for *Ba*; in the range of 0.096 and 0.172 μg/g for *W* (Fig. 3). *As* and *Sb* are below the LoD.

The pure brucite has concentrations in the range: 2.19-18.6 μg/g for *B*, 0.074 – 0.2 μg/g for *Ba*, 0.03-0.51 μg/g for *Sr*, and 0.031-1.09 μg/g for *W*. *As* and *Sb* are in most of the cases below the LoD; only two measurement gave 0.36 μg/g for *As* and 0.102 μg/g for *Sb*.

6.4 High-pressure veins (2245)

The metamorphic olivine contained in the major vein is characterized by *B* contents comparable to the Al-rich antigorite (19-21 μg/g), Sr concentrations in the range 0.06-0.3 μg/g and *Ba* concentrations around 0.5 μg/g. These values are comparable to the values measured within the reaction bands, while they have a slightly lower *W* content

(0.014 µg/g) and are very enriched in *Li*, which ranges between 14 and 15 µg/g. (Fig. 30).

A significant difference can be observed between the *Ti-chu* present within the major vein and the *Ti-chu* within the en-echelon vein, the former being less enriched in *B* (9-10 µg/g) and in *W* (0.019-0.027 µg/g) with respect to the latter (*B* 37-50 µg/g, *W* 0.49-1.06 µg/g). Conversely, *Ba* shows higher concentrations within the thicker vein with respect to the en-echelon ones (0.07-0.27 µg/g and 0.016 µg/g, respectively).

Clinochlore present within the vein has *B* contents equivalent to the coeval olivine (7.9-14 µg/g), and is depleted in the other FMEs (values in the Appendix). The high-pressure diopside contained in the vein was not analysed.

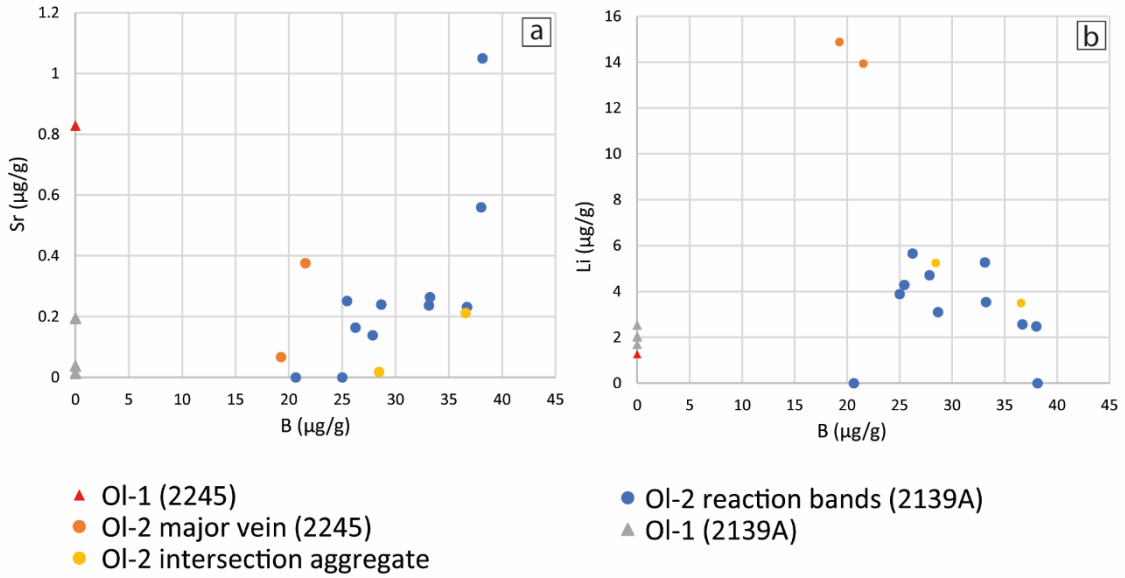

Figure 30. Fluid-mobile elements distributions in olivine generations. *Ol*-1=mantle olivine, *Ol*-2= metamorphic olivine. Legend for all plots below, samples in brackets. a) *B* vs *Sr*, b) *B* vs *Li*. The values below the detection limits for *B* in *Ol*-1 were set to 0 to allow the visualization of the different compositions.

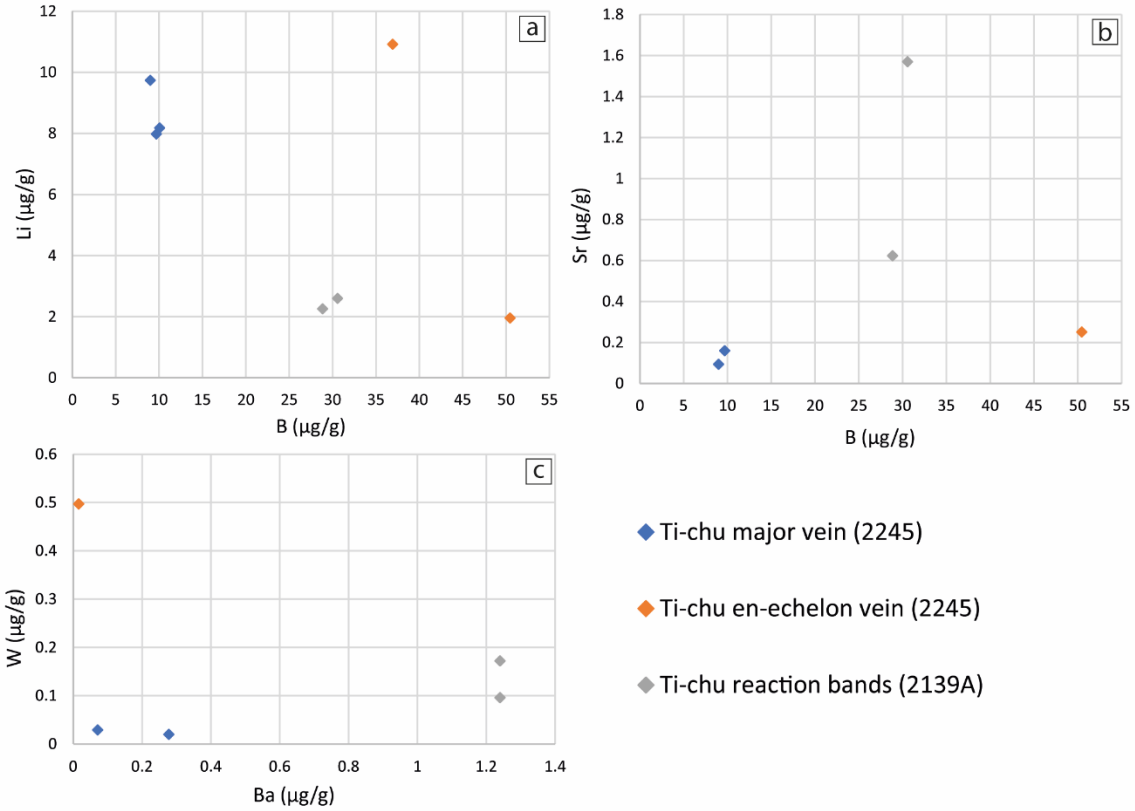

Figure 31. Fluid-mobile elements distributions in Ti-clinohumite hosted in the different structures. Legend on the bottom right, samples indicated in brackets. a) *Bs* vs *W*, b) *B* vs *Sr*, c) *B* vs *Li*.

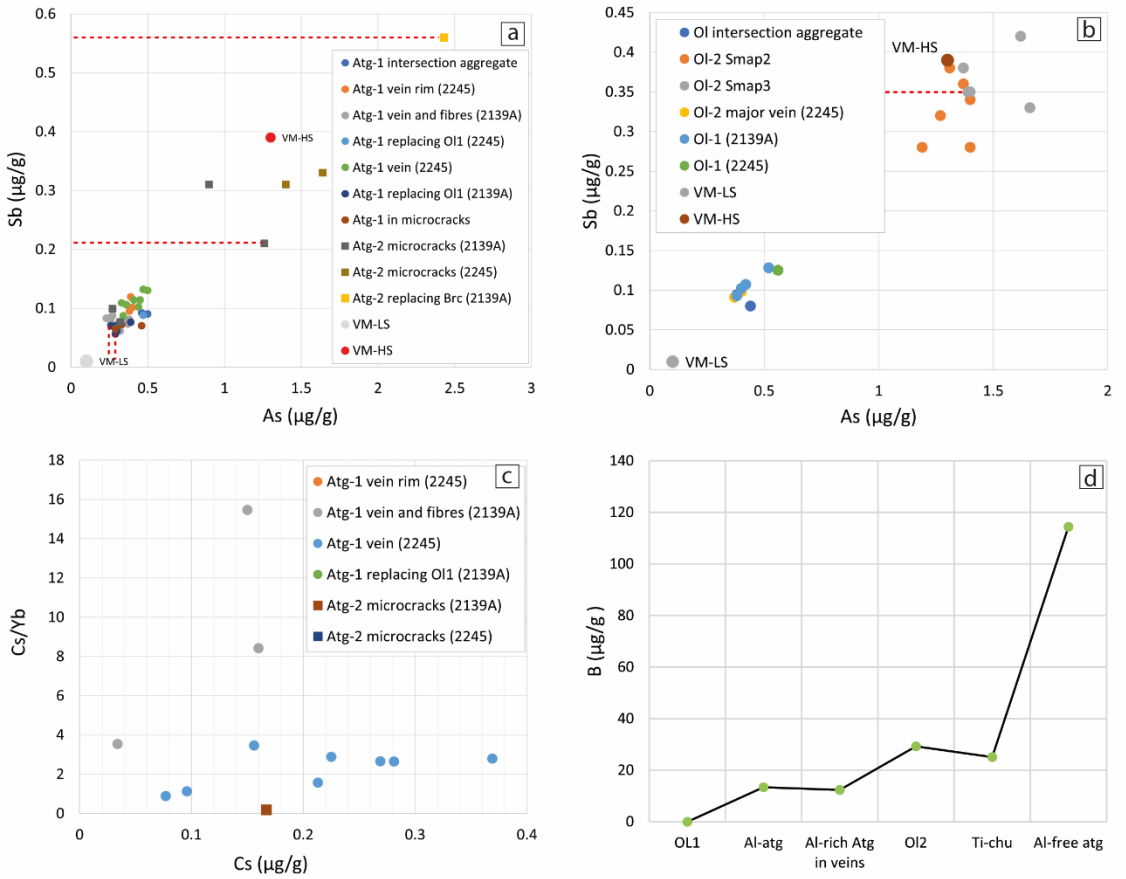

Figure 32. a, b) *As* and *Sb* fluid-mobile elements distribution for the antigorite and olivine generations (respectively) in different sites and samples. LoD values are included, to be considered as maximum values, values above the LoD for either *As* or *Sb* are highlighted by red, dashed lines. Abbreviations for antigorite as in Fig. 28, for olivine as in Fig. 30. VM-LS= Voltri Massif low-strain domains, VM-HS=Voltri Massif high-strain domains. Values for VM-LS and VM-HS from Cannaò et al. (2016). c) *Cs* vs *Cs/Yb* systematics for antigorite generations, only the series with values above the LoD are included. d) *B* contents in the subsequent generations of *Ol*, *Atg* and *Ti-chu*.

7. Discussion and conclusions

7.1 Discussion and conclusions

This thesis investigates meta-peridotites of the Erro-Tobbio (E-T) Unit, in the Voltri ultramafic Massif (Western Alps). The E-T Unit experienced Eoalpine, subduction metamorphism, reaching eclogite-facies peak conditions of 2.0-2.5 GPa and 550-600°C. The E-T Unit is mainly composed of antigorite meta-peridotites, which experienced antigorite dehydration during the prograde subduction path. This dehydration process is spectacularly recorded and preserved by the widespread occurrence of veins and reaction bands of metamorphic olivine derived from antigorite + brucite breakdown ($Atg+Brc \rightarrow Ol+H_2O$). The fluids released through this breakdown reaction escaped from the slab through a channel network (*Plümper et al., 2016*). The fluids released during subduction have many geodynamic implications, including the role of triggering of intermediate-depth earthquakes and slow earthquakes via dehydration embrittlement. The E-T Unit was selected as a suitable candidate for hosting structures representing slow earthquakes, since formation of the olivine veins and reaction bands described in previous studies (*Scambelluri et al., 1991, 1995, Plümper at al., 2016*) was estimated within the depth range 25-60 km , where slow earthquakes typically occur. The purpose of this thesis was to describe the deformation structures associated to the breakdown of antigorite and brucite displayed by the meta-peridotites of Mt. Tobbio, with the future aim of possibly associate these structures to slow earthquakes occurrence. However, within the frame of this thesis it was only possible to complete a preliminary detailed description of these structures associated with the meta-peridotite dehydration, by integrating a fieldwork study, microstructural analysis and geochemical analysis. The main results of my research are discussed hereafter.

- Olivine veins/reaction bands occur in a dominant steeply-dipping set (OlF1) within the large low strain domains oriented at a nearly orthogonal angle to N-S trending serpentinite mylonite horizons (a few tens of cm thick) wrapping the meta-peridotite domain. In detail, the olivine veins/reaction bands show a more complex organization, with the dominant OlF1 associated with differently oriented sets. In the thinner low-strain domain on the eastern bank of the Gorzente creek, a main set of olivine veins/reaction bands (OlF2) is parallel to the serpentinite mylonite foliation, and progressively intensifying towards (and within) the mylonites. These mylonitic domains consists either of mylonites with

a piano-parallel foliation outlined by OlF2 (type 1 mylonite), or of chaotic serpentinite, apparently *Ol*-free (type 2 mylonite). The presence of *Ol+Ti-chu* bands within mylonites was recognized also at the microscopic scale, where they form C-planes in the mylonitic foliation. This geometrical arrangement suggests a correlation between the brittle structures hosted in the low-strain domains and the mylonitic horizons, which is consistent with the partition of deformation due to the rheological heterogeneity described at depth ranges consistent with slow earthquakes. Rheological heterogeneities have been suggested to play a key role for occurrence of (i) tremors, triggered by brittle fracturing within low-strain domains, and (ii) correlated SSEs, accommodated by the ductile flow within mylonites.

- Microstructural analysis of OlF1 shows the occurrence of a complex sequence of dehydration and hydration reactions. The early pervasive serpentinization of the peridotite resulting in Al-rich antigorite, is followed by extensive dehydration ($Atg+Brc \rightarrow Ol+H_2O$) to form metamorphic olivine (Ol_2) arranged in reaction bands. EBSD analysis reveals an epitaxial growth of metamorphic Ol_2 on the mantle relic Ol_1. Within OlF1 reaction bands, in the low-strain domain, only a very minor crystal-plastic deformation localized at the contact between the two generations of olivine. The meta-peridotites were affected by a new stage of hydration after formation of Ol_2, especially localized within the reaction bands network along microcracks (5-10 μm thick) bearing a porous/fibrous phase identified as antigorite and locally brucite. In turn, this new antigorite was affected by dehydration with formation of granoblastic olivine (Ol_3).
- Microchemical (SEM-EDS) analysis reveals the presence of two generations of antigorite: (i), *Al-rich* antigorite, extensively replacing the mantle minerals and forming the meta-peridotite matrix, and (ii) *Al-free* antigorite, present within the microcracks hosted within the reaction bands. The 2 antigorite generations also differ in terms of trace elements composition. The *Al-free* antigorite is enriched in FMEs (*B, As, Sb, W, Ba, Sr*) compared to the *Al-rich* antigorite. In particular, the *As* and *Sb* concentrations in the *Al-rich* antigorite are consistent with the bulk composition of low-strain domains measured by Cannaò et al. (2016) over the Voltri Massif, and reflect an oceanic geochemical signature. The *As* and *Sb* concentrations of *Al-free* antigorite composition in *As* and *Sb* is, conversely, compatible with the bulk composition of high-strain domains in the Voltri Massif,

and reflect an influx of sedimentary and crust-derived fluids (*Cannaò et al., 2016*). The *As* and *Sb* concentrations in Ol_1 and Ol_2 suggest opening of the system during the first dehydration stage. Ol_2, in fact, is clustered in correspondence to the high-strain domains of the Voltri Massif, indicating interaction with externally-derived fluids. Conversely, Ol_1 is clustered at lower concentrations of *As* and *Sb*. In the case of olivine, however, more reliable data are needed for inferences on the fluid sources, since only one measurement for *Sb* and *As* in Ol_2 was above the LoD.

These observations indicate a transition from closed to an open chemical system during eclogite-facies deformation. The influx of subduction fluids along the network of olivine veins and reaction bands is, therefore, interpreted as a result of fluid-rock interaction occurring within subduction channel domains. These data are also compatible with the enrichment in *B* displayed by Ol_2 and Al-free antigorite with respect to Al-rich antigorite. Increasing subduction metamorphism and dehydration reactions should, in contrast, result in *B* loss. These observations indicate, as well, influx of fluids released from the subducting slab, consistently with the results on *B* isotopes systematics reported by Scambelluri et al. (2012) and Clarke et al. (2020). Moreover, the *Cs* and *Yb* systematics in Al-rich antigorite indicate that the early stage of serpentinization occurred at forearc regions, displaying values consistent with the results of Peters et al. (2017).

The observations collected during my thesis, clearly do not allow the interpretation of these structures in the E-T Unit in terms of subduction zone seismicity, despite they document the occurrence of 2 main stages of fluid release at conditions consistent with the occurrence of either earthquakes s.s. or slow earthquakes. However, my study allows a further step in understanding the dehydration processes occurring at the plate interface at eclogite-facies conditions. In particular, as a main result, I was able to discriminate 2 dehydration stages occurring within a system that progressively opens to infiltration of slab-derived fluids.

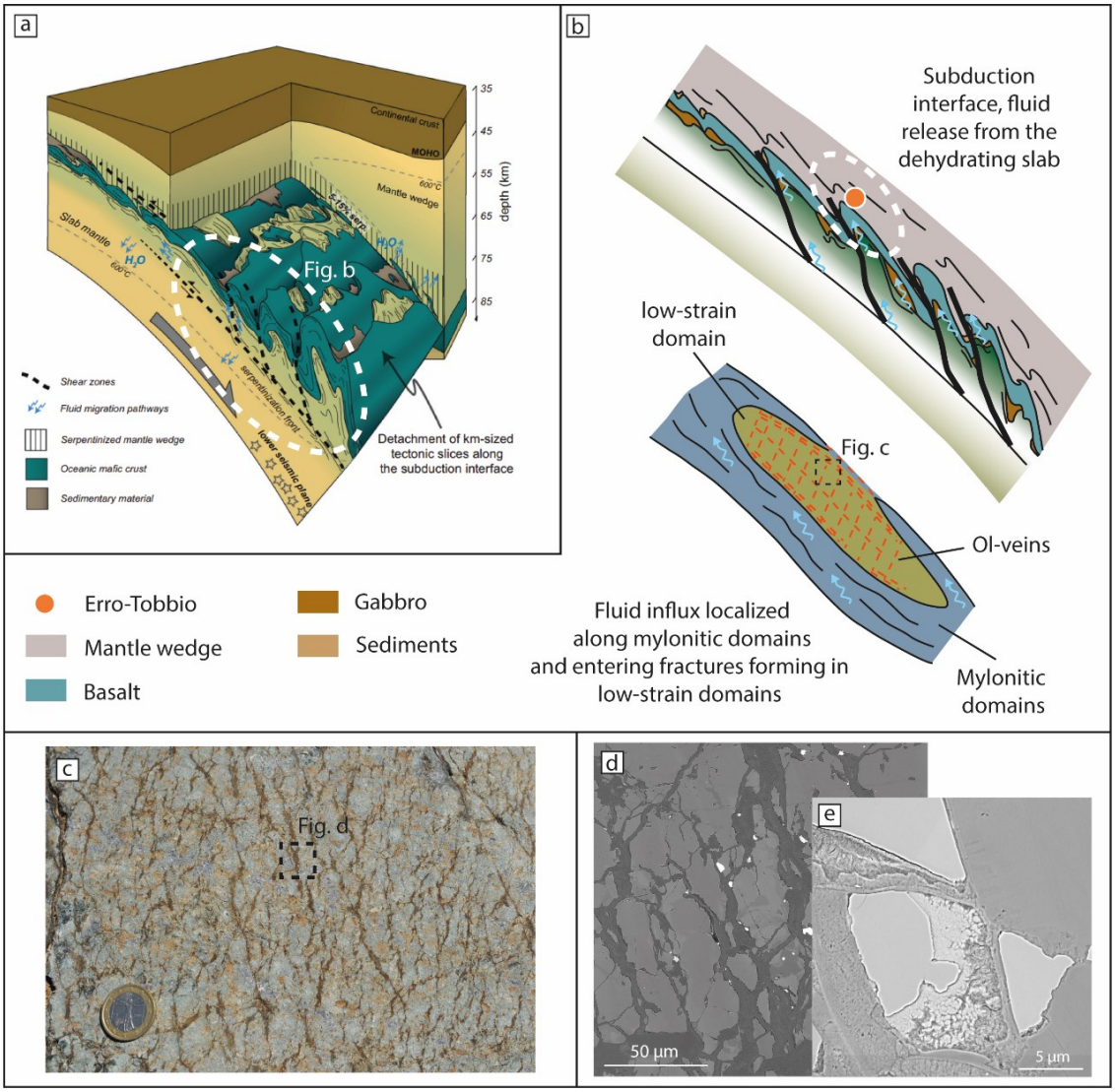

Figure 33. Sketches of the proposed fluid-rock interactions occurred within the E-T Unit at peak metamorphic conditions. a) General sketch of a subduction zone interface at 35-85 km, including the SSTs depth range (30-60 km), which is characterized by detachment of tectonic slices (tectonic underplating) and high fluid pressure (fluid release from the slab). From Angiboust et al. (2012). b) Above, idealized sketch of the subduction interface indicating the fluid pathways from the dehydrating slab reaching the estimated location for the E-T Unit (after Guillot et al., 2015, Clarke et al., 2020). Below, sketch of the relationship between the undeformed and the mylonitic domains, the latter representing preferential pathways for fluid influx from the dehydrating slab which penetrate also within the *Ol* veins and reaction bands forming within the low-strain domains. c) OlF1 reaction bands, composed of metamorphic olivine (Ol_2) dissected by antigorite microcracks related to a stage of hydration (influx of sedimentary-derived fluids) (d), and final dehydration stage with formation of Ol_3 replacing Ol_2 along the microcracks (e).

7.2 Further developments

To better constrain the developments of the *Ol + Ti-chu* structures and their relationship with the ductile domains, and to further analyse the E-T Unit in a perspective of slow earthquakes, future studies should include:

- Extension of the detailed microstructural observations to all the structural elements (OlF2 and mylonites)
- Detailed investigation of the shear zone hosting *Ol+Ti-chu* veins involved in the ductile deformation, to investigate the relationships between overprinting brittle and ductile deformation.
- Further in-situ geochemical analyses, to produce a more robust database, taking into account all the different fabrics (OlF1, OlF2, serpentinite mylonites) to assess their correlation in terms of fluid fluxes (e.g. to assess whether the fluids localized along the antigorite mylonites are related to the formation of the reaction bands), possibly considering also *O*, *B* and *Sr* stable isotopes.
- Quantification of the slip and strain rates associated to each deformation event, to verify the match with the values measured for slow earthquakes.

Appendix

A1. Raman spectra of the main phases and serpentine minerals.

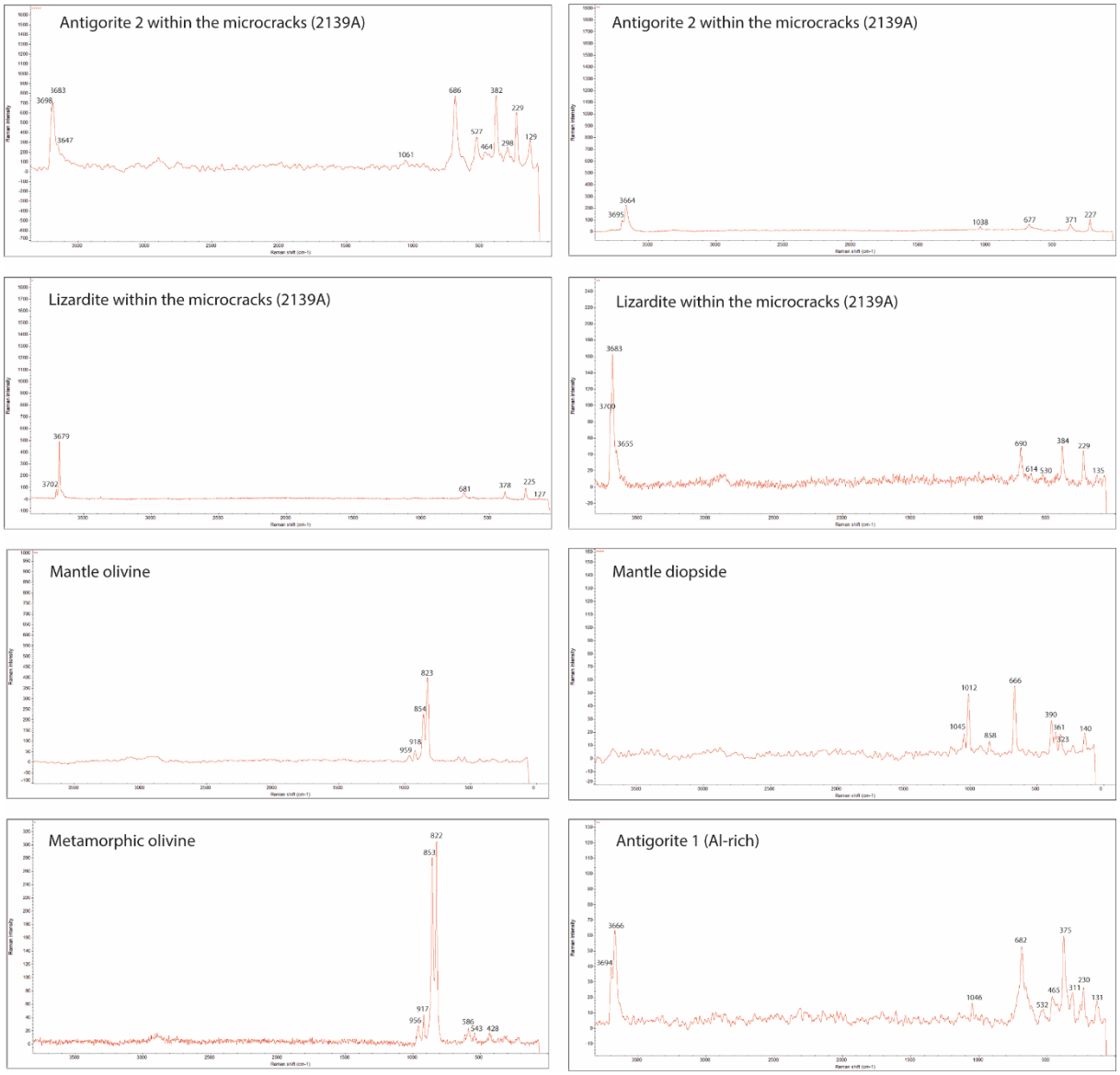

Raman spectra for key minerals in sample 2139A.

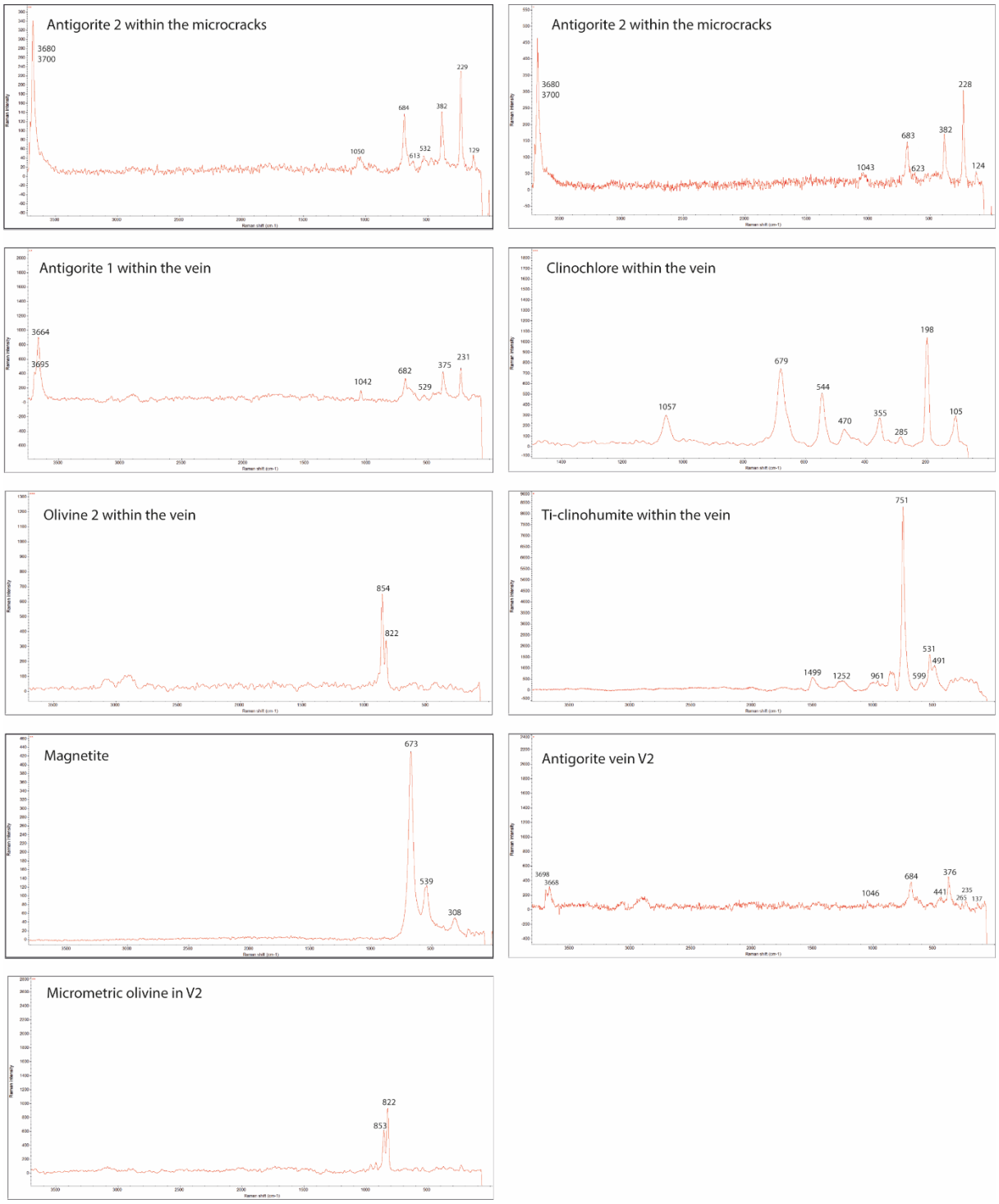

Raman spectra for key minerals in sample 22-45.

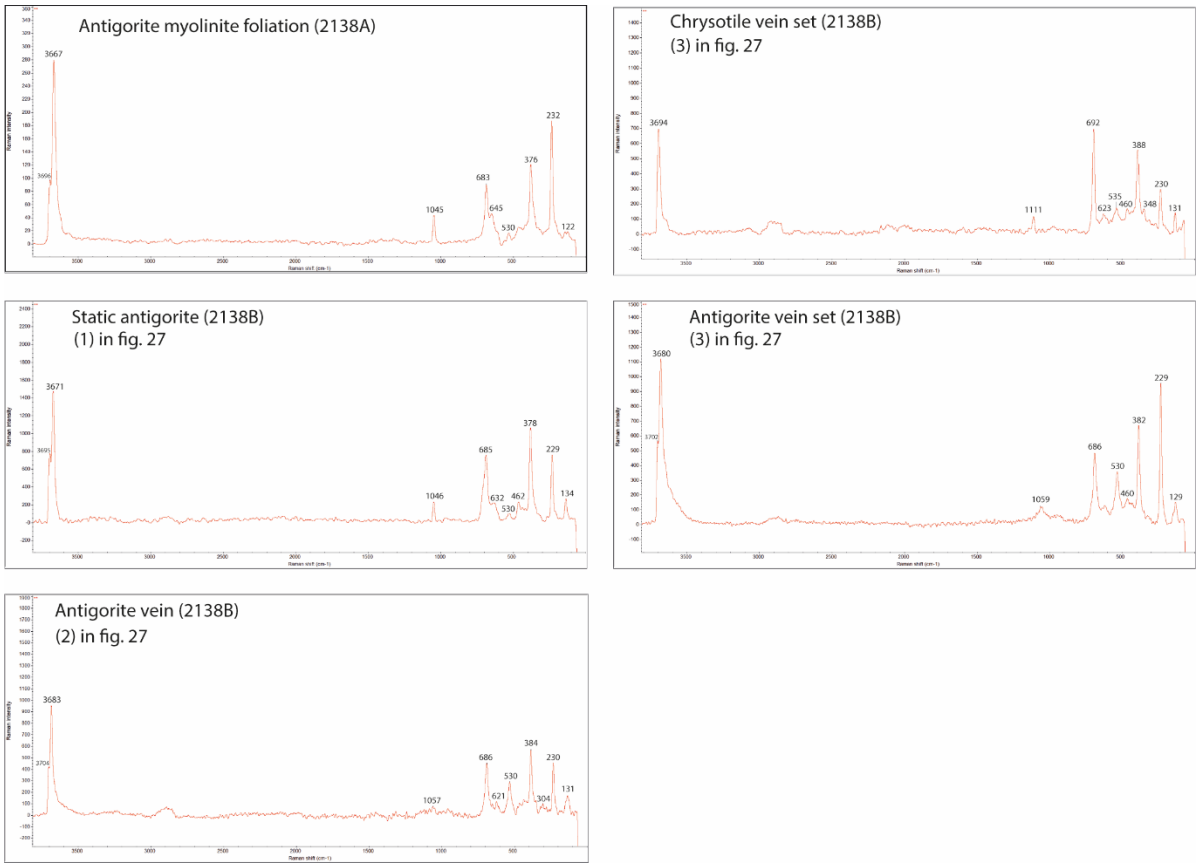

Raman spectra for key minerals in samples 2138A and 2138B.

The distinction of the serpentine polymorphs was only rarely straightforward. Commonly, spectra displaying peaks associated to both antigorite and lizardite, suggest the presence of a mixture of the two polymorphs in the analysed area. An example is the presence of lizardite typical O-H related peaks (3683-3702 cm^{-1}) associated with the characteristic peak for antigorite around 1044 cm^{-1}, slightly shifted towards higher Raman shifts (1050 cm^{-1}). A shoulder peak at around 3649 cm^{-1} within serpentine spectra indicates the presence of a mixture of serpentine and brucite, as proposed by Uno et al., 2019.

A2. Micro-Raman map *Rmap1*.

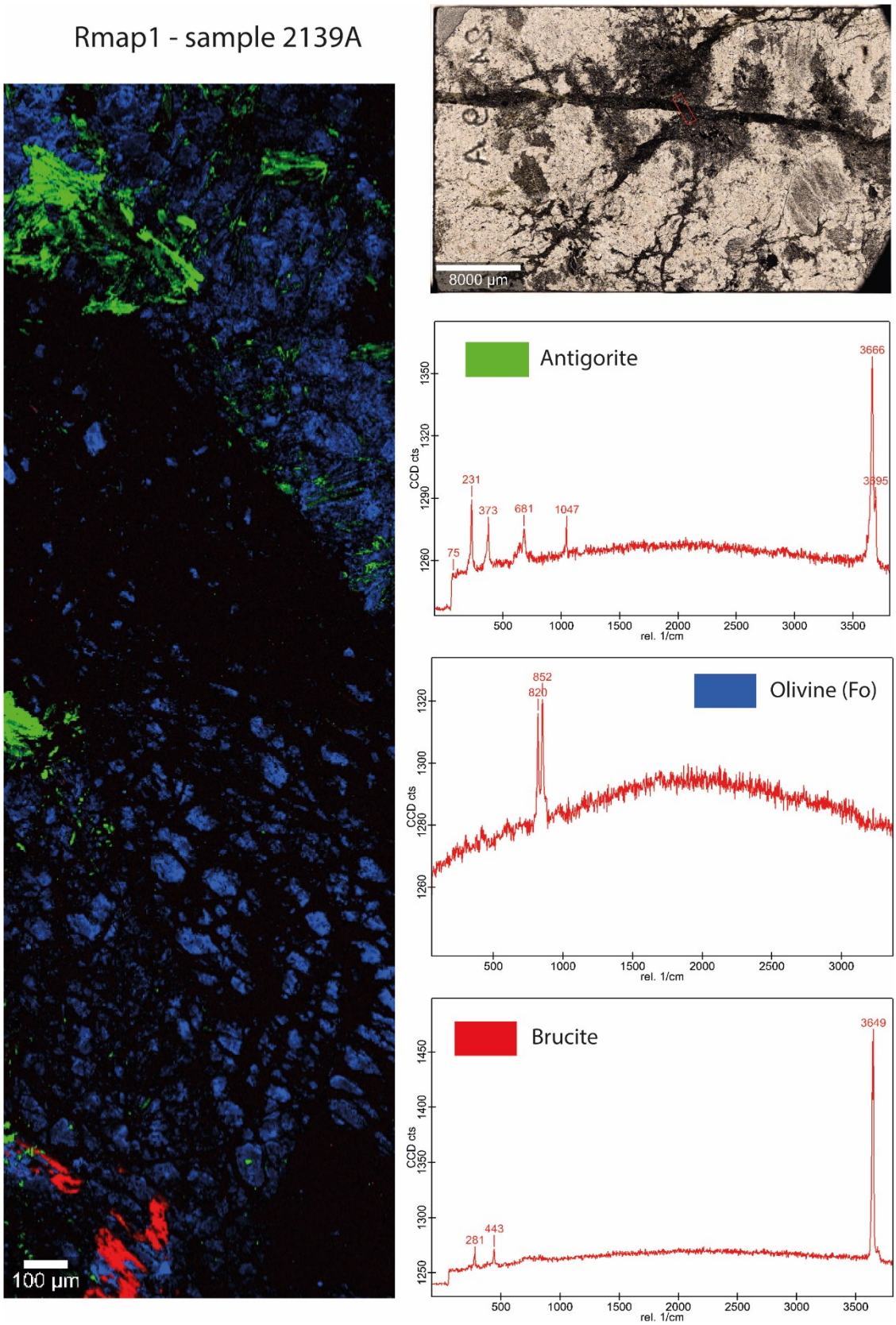

A3. Micro-Raman map *Rmap2*.

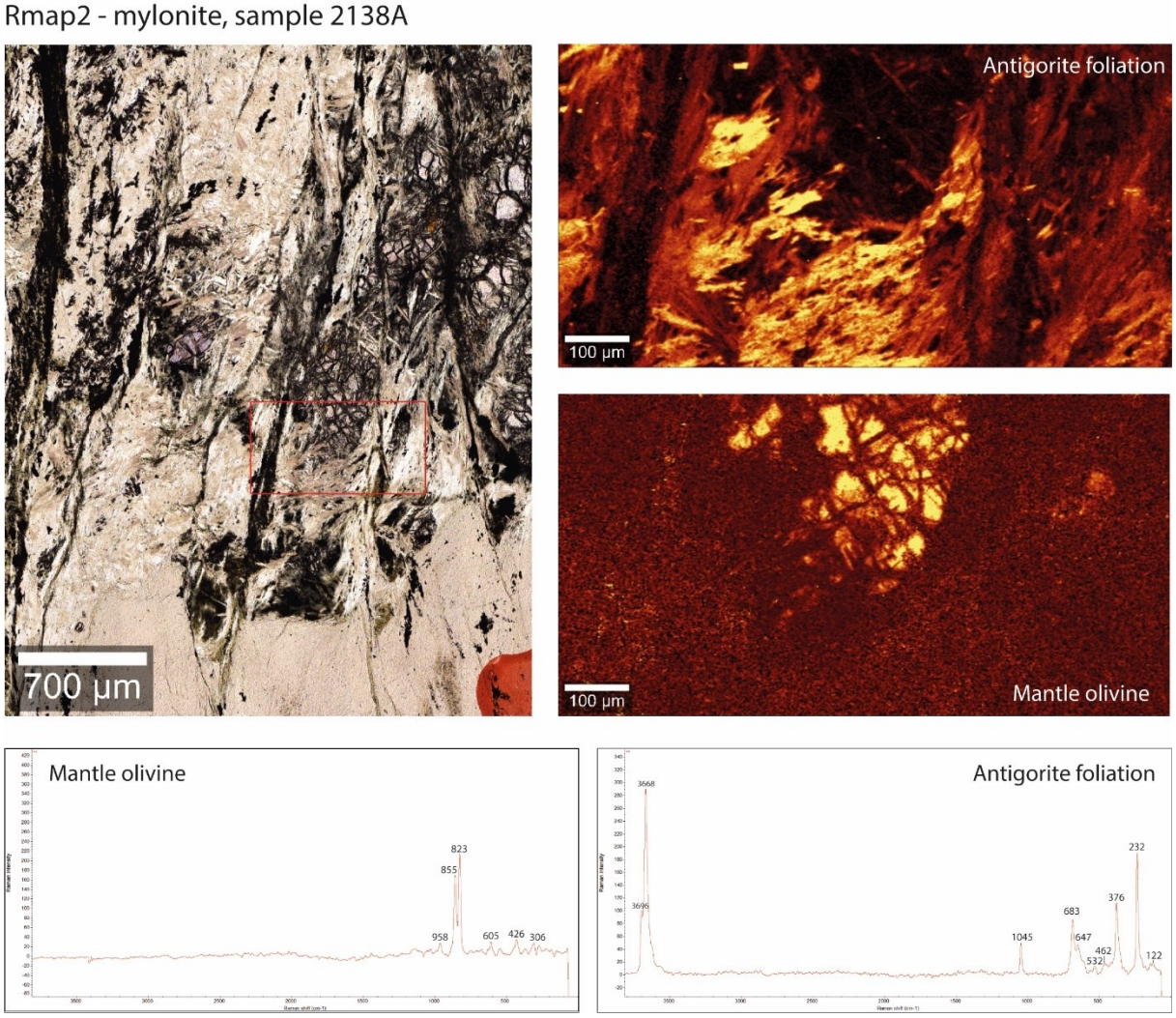

Micro-Raman map Rmap2 performed on an area of the mylonitic foliation of sample 2138A.

A4. EDS spectra (non-calibrated).

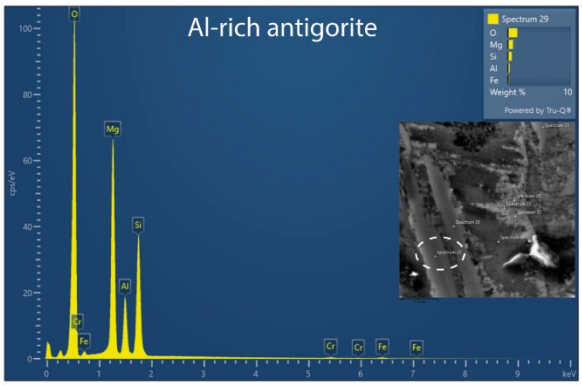

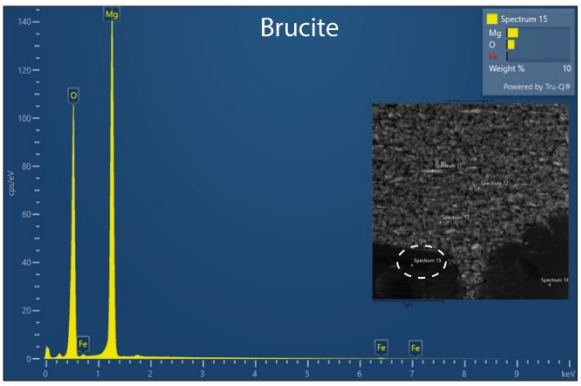

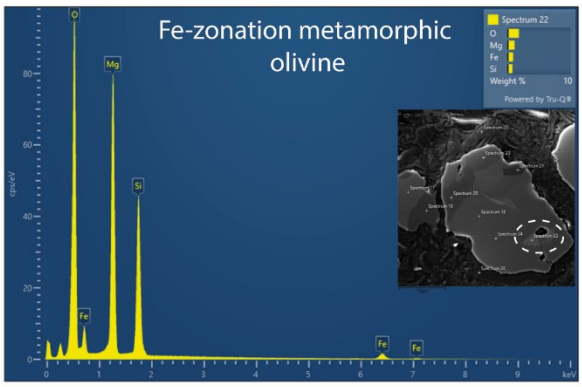

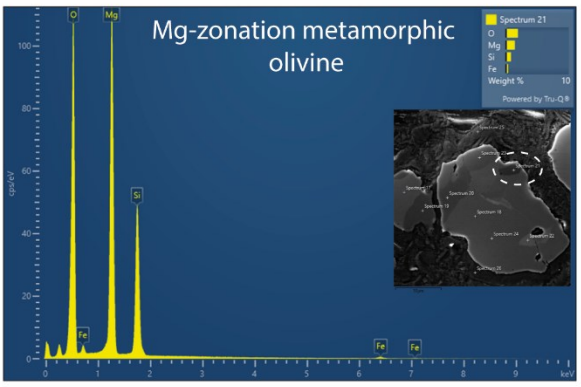

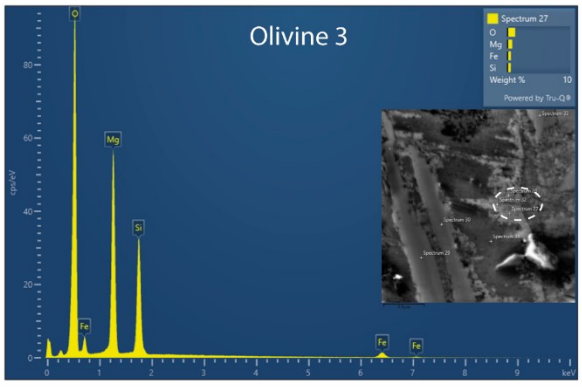

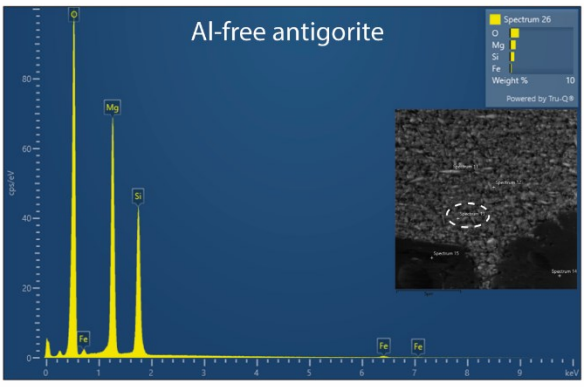

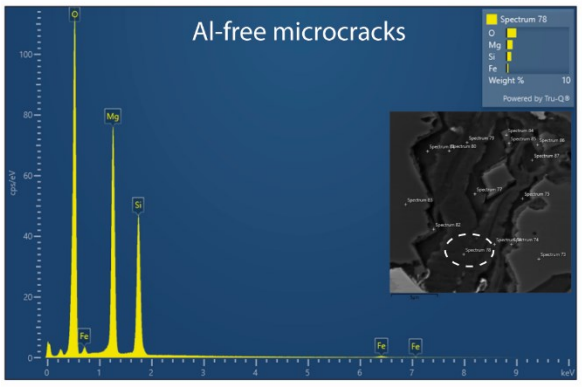

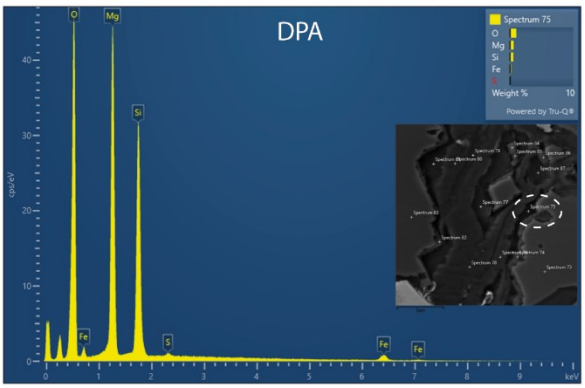

A5. EBSD map Smap2

The phase map obtained from the EBSD map *Smap2*, collected at the contact between an olivine mantle relic and metamorphic olivine, shows the presence of brucite within the microcracks dissecting the metamorphic olivine within the reaction bands, commonly in association with magnetite.

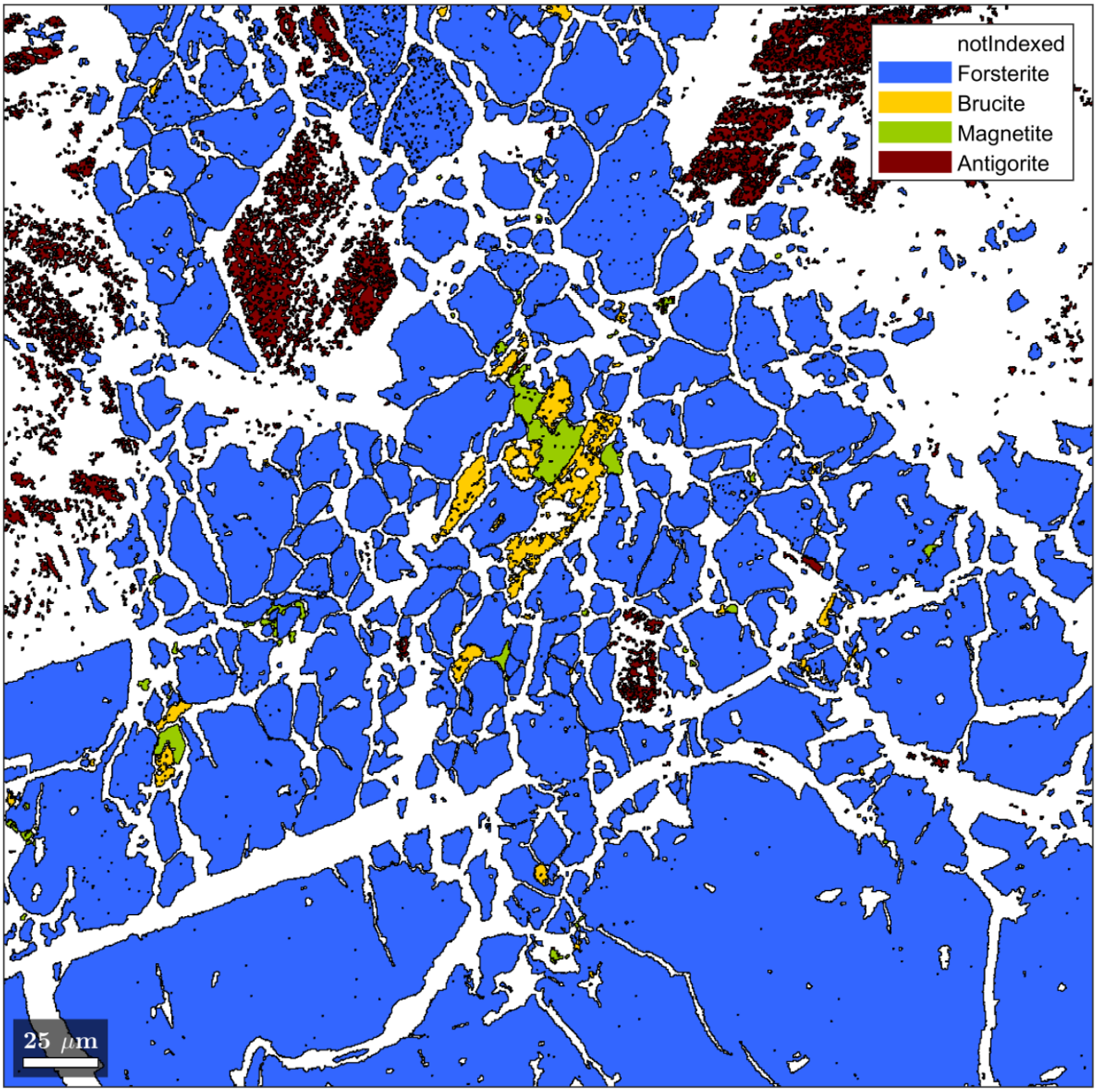

A6. LA-ICP-MS internal standards

	Internal standard for each mineral (wt %)			
	SiO_2	CaO	MgO	Reference
Antigorite	42.6			Scambelluri et al. (1997)
Olivine	41			Scambelluri et al. (1997)
Carbonate		56		-
Brucite			50-70	Scambelluri et al. (1997)
Ti-clinohumite	36			Scambelluri et al. (1997, 2001)
Chlorite-Clinochlore	35			Scambelluri et al. (1997)
Mantle diopside	50			Scambelluri et al. (2001)

Considering brucite, an internal standard of 70 wt% MgO was for set for the pure generation, since the SEM-EDS measurement evidenced absence or a very minor Fe content. The brucite-antigorite mixtures provided SiO_2 values too high for brucite and were therefore recomputed with a 50 wt% MgO as internal standard, which provided a SiO_2 content of 22,29 wt% and consequently a water content of ~30 wt%, which is consistent with the values found in literature for brucite (*Scambelluri et al., 1997*). The values for the mantle pyroxene relics, originally determined considering 42.6 wt% SiO_2 as internal standard, were recomputed with a 50 wt% SiO_2 (*Scambelluri et al., 2001*).

A7. RSD and accuracy values for standards used for calibration of trace element analyses.

BCR-2g			40 micron					25 micron		
Element	Mean	2sd	RSD%	Ref	Accuracy%	Mean	2sd	RSD%	Ref	Accuracy%
Li7	9.38	0.28	3%	9	4%	8.90	1.53	17%	9	-1%
Be9	1.92	0.21	11%	2.3	-17%	1.95	0.96	50%	2.3	-15%
B11	5.22	0.54	10%	6	-13%	5.03	-	-	6	-16%
Mg25	21262.29	227.88	1%	21360	0%	20300.80	888.65	4%	21360	-5%
Al27	69896.24	1092.86	2%	73320.75	-5%	69616.84	2100.47	3%	73320.75	-5%
Si29	253000.01	0.03	0%		Int Std	253000.07	0.02	0%		Int Std
Ca43	49745.31	734.63	1%	50428.57	-1%	48957.53	2588.61	5%	50428.57	-3%
Sc45	33.10	0.93	3%	33	0%	32.25	0.34	1%	33	-2%
Ti49	13611.80	94.08	1%	14100	-3%	13250.97	397.15	3%	14100	-6%
V51	436.20	6.61	2%	425	3%	415.45	33.98	8%	425	-2%
Cr53	15.86	1.31	8%	17	-7%	16.53	0.96	6%	17	-3%
Mn55	1513.47	5.06	0%	1550	-2%	1449.38	72.96	5%	1550	-6%
Co59	37.75	0.31	1%	38	-1%	36.32	1.89	5%	38	-4%
Ni60	11.82	0.75	6%	13	-9%	9.58	1.42	15%	13	-26%
Cu65	17.11	0.52	3%	21	-19%	16.51	1.36	8%	21	-21%
Zn66	141.45	2.08	1%	125	13%	124.44	12.47	10%	125	0%
As75	0.74	0.07	9%	0.7	6%	1.07	-	-	0.7	53%
Rb85	46.87	1.17	2%	47	0%	44.05	4.32	10%	47	-6%
Sr88	334.02	2.86	1%	342	-2%	332.51	4.89	1%	342	-3%
Y89	32.45	0.56	2%	35	-7%	32.46	1.82	6%	35	-7%
Zr90	172.44	3.61	2%	184	-6%	177.73	7.35	4%	184	-3%
Nb93	11.72	0.40	3%	12.5	-6%	11.94	0.59	5%	12.5	-4%
Mo95	258.29	3.05	1%	270	-4%	247.91	7.95	3%	270	-8%
Sb121	0.36	0.09	25%	0.35	3%	0.33	0.10	31%	0.35	-6%
Cs133	1.16	0.09	8%	1.16	0%	1.14	0.08	7%	1.16	-2%
Ba137	659.79	10.58	2%	683	-3%	629.86	23.85	4%	683	-8%
La139	24.12	0.50	2%	24.7	-2%	23.69	0.62	3%	24.7	-4%
Ce140	51.05	0.95	2%	53.3	-4%	51.21	2.34	5%	53.3	-4%
Pr141	6.44	0.16	2%	6.7	-4%	6.35	0.19	3%	6.7	-5%
Nd146	27.07	0.52	2%	28.9	-6%	26.89	1.53	6%	28.9	-7%
Sm149	6.18	0.15	2%	6.59	-6%	6.23	0.37	6%	6.59	-5%
Eu151	1.87	0.05	3%	1.97	-5%	1.87	0.12	7%	1.97	-5%
Gd157	6.25	0.17	3%	6.71	-7%	6.55	0.88	13%	6.71	-2%
Tb159	0.96	0.05	5%	1.02	-6%	1.03	0.03	3%	1.02	1%
Dy163	6.07	0.21	3%	6.44	-6%	6.13	0.20	3%	6.44	-5%
Ho165	1.18	0.03	3%	1.27	-7%	1.18	0.09	7%	1.27	-7%
Er167	3.53	0.15	4%	3.7	-5%	3.30	0.17	5%	3.7	-11%
Tm169	0.48	0.04	8%	0.51	-6%	0.48	0.03	5%	0.51	-5%
Yb173	3.14	0.17	5%	3.39	-7%	3.39	0.46	13%	3.39	0%
Lu175	0.47	0.02	4%	0.503	-7%	0.48	0.07	14%	0.503	-6%
Hf177	4.44	0.15	3%	4.84	-8%	4.19	0.38	9%	4.84	-13%
Ta181	0.73	0.04	5%	0.78	-6%	0.78	0.17	21%	0.78	0%
W182	0.55	0.03	5%	0.5	10%	0.52	0.11	21%	0.5	4%
Pb208	10.66	0.13	1%	11	-3%	10.41	0.49	5%	11	-5%
Th232	5.62	0.18	3%	5.9	-5%	5.63	0.37	7%	5.9	-5%
U238	1.62	0.04	2%	1.69	-4%	1.47	0.15	10%	1.69	-13%

ARM3	40 micron					25 micron				
Element	Mean	2sd	RSD%	Ref (ppm)	Accuracy%	Mean	2sd	RSD%	Ref (ppm)	Accuracy%
Li7	17.70	0.27	2%	18.6	-5%	18.29	0.46	2%	18.6	-2%
Be9	6.24	0.31	5%	6.29	-1%	5.42	0.93	17%	6.29	-14%
B11	49.32	1.55	3%	60.6	-19%	53.01	2.51	5%	60.6	-13%
Mg25	20810.41	140.75	1%	21060	-1%	20342.21	698.66	3%	21060	-3%
Al27	72211.32	731.96	1%	75509.43396	-4%	71408.93	1475.39	2%	75509.43	-5%
Si29	281858.01	0.03	0%	0	Int Std	281857.97	0.03	0%	0	Int Std
Ca43	36663.75	450.10	1%	38000	-4%	37195.53	2389.86	6%	38000	-2%
Sc45	11.43	0.38	3%	7.02	63%	11.67	1.14	10%	7.02	66%
Ti49	6233.60	30.00	0%	6109.876543	2%	6195.84	288.85	5%	6109.877	1%
V51	11.26	0.33	3%	12.2	-8%	10.70	0.71	7%	12.2	-12%
Cr53	8.63	1.06	12%	9.07	-5%	8.70	1.45	17%	9.07	-4%
Mn55	370.45	3.06	1%	387.3239437	-4%	368.82	6.15	2%	387.3239	-5%
Co59	7.11	0.27	4%	7.45	-5%	7.38	0.31	4%	7.45	-1%
Ni60	11.82	0.59	5%	12.3	-4%	13.36	4.29	32%	12.3	9%
Cu65	12.52	0.50	4%	13.6	-8%	12.88	1.69	13%	13.6	-5%
Zn66	31.65	0.40	1%	36.1	-12%	29.36	2.92	10%	36.1	-19%
As75	3368.40	41.37	1%	3780	-11%	3541.11	292.80	8%	3780	-6%
Rb85	7.24	0.22	3%	7.54	-4%	7.14	0.36	5%	7.54	-5%
Sr88	18.89	0.11	1%	19.6	-4%	18.62	1.93	10%	19.6	-5%
Y89	7.24	0.14	2%	7.05	3%	7.59	0.77	10%	7.05	8%
Zr90	10.93	0.32	3%	10.9	0%	11.30	0.82	7%	10.9	4%
Nb93	11.96	0.23	2%	12.2	-2%	12.24	0.68	6%	12.2	0%
Mo95	9.37	0.17	2%	9.49	-1%	9.07	1.46	16%	9.49	-4%
Sb121	13.56	0.25	2%	13	4%	13.38	0.28	2%	13	3%
Cs133	7.24	0.16	2%	7.53	-4%	6.94	0.34	5%	7.53	-8%
Ba137	27.81	0.42	2%	28.4	-2%	27.25	1.43	5%	28.4	-4%
La139	6.34	0.21	3%	6.62	-4%	6.72	0.21	3%	6.62	2%
Ce140	7.76	0.21	3%	7.97	-3%	8.14	0.50	6%	7.97	2%
Pr141	5.49	0.10	2%	5.68	-3%	5.46	0.22	4%	5.68	-4%
Nd146	7.43	0.16	2%	7.53	-1%	7.91	1.22	15%	7.53	5%
Sm149	5.77	0.21	4%	6	-4%	5.71	0.26	5%	6	-5%
Eu151	5.51	0.09	2%	5.71	-4%	5.51	0.16	3%	5.71	-4%
Gd157	5.88	0.34	6%	6	-2%	5.62	0.87	15%	6	-6%
Tb159	6.29	0.10	2%	6.62	-5%	6.70	0.52	8%	6.62	1%
Dy163	6.11	0.20	3%	6.18	-1%	6.30	0.79	13%	6.18	2%
Ho165	6.71	0.09	1%	7.17	-6%	7.29	0.58	8%	7.17	2%
Er167	6.34	0.17	3%	6.28	1%	5.70	0.40	7%	6.28	-9%
Tm169	6.07	0.11	2%	6.47	-6%	6.43	0.12	2%	6.47	-1%
Yb173	8.80	0.47	5%	8.88	-1%	8.89	0.49	6%	8.88	0%
Lu175	6.31	0.08	1%	6.48	-3%	6.79	0.38	6%	6.48	5%
Hf177	5.69	0.23	4%	6.21	-8%	5.67	0.60	11%	6.21	-9%
Ta181	6.11	0.09	1%	6.16	-1%	6.21	0.17	3%	6.16	1%
W182	9.16	0.23	3%	9.12	0%	9.01	0.78	9%	9.12	-1%
Pb208	12.15	0.25	2%	12.7	-4%	12.16	0.35	3%	12.7	-4%
Th232	3.12	0.05	2%	3.28	-5%	3.21	0.18	5%	3.28	-2%
U238	3.56	0.05	1%	3.75	-5%	3.58	0.17	5%	3.75	-4%

ML3B

	40 micron					25 micron				
Element	Mean	2sd	RSD%	Ref (ppm)	Accuracy%	Mean	2sd	RSD%	Ref (ppm)	Accuracy%
Li7	4.82	0.34	7%	4.5	7%	4.74	0.71	15%	4.5	5%
Be9	0.60	0.14	22%	0.62	-3%	0.91	0.13	15%	0.62	46%
B11	2.55	0.39	15%	2.5	2%	6.42	-	-	2.5	157%
Mg25	40030.79	471.03	1%	39540	1%	38666.50	2434.45	6%	39540	-2%
Al27	67849.57	932.30	1%	74415.094	-9%	63159.59	4906.89	8%	74415.094	-15%
Si29	240263.85	0.03	0%	Int Std	0%	240263.79	0.04	0%	Int Std	0%
Ca43	70625.99	1346.91	2%	75000	-6%	67092.50	4544.00	7%	75000	-11%
Sc45	29.29	0.87	3%	31.6	-7%	27.35	2.08	8%	31.6	-13%
Ti49	12171.11	142.66	1%	12885.185	-6%	11434.92	771.72	7%	12885.185	-11%
V51	293.36	4.72	2%	268	9%	291.73	25.22	9%	268	9%
Cr53	162.54	8.75	5%	177	-8%	166.89	2.65	2%	177	-6%
Mn55	1317.01	8.23	1%	1316.901	0%	1252.17	28.61	2%	1316.901	-5%
Co59	44.71	1.03	2%	41.2	9%	44.50	4.01	9%	41.2	8%
Ni60	106.51	1.86	2%	107	0%	113.93	5.19	5%	107	6%
Cu65	115.75	1.89	2%	112	3%	107.81	5.46	5%	112	-4%
Zn66	107.77	3.17	3%	108	0%	98.78	4.08	4%	108	-9%
As75	0.43	0.08	20%	0.28	54%	-	-	-	0.28	-
Rb85	5.75	0.20	3%	5.8	-1%	5.25	0.22	4%	5.8	-10%
Sr88	300.39	3.04	1%	312	-4%	282.18	32.67	12%	312	-10%
Y89	21.08	0.54	3%	23.9	-12%	18.52	1.48	8%	23.9	-23%
Zr90	110.33	2.14	2%	122	-10%	100.37	8.69	9%	122	-18%
Nb93	7.80	0.14	2%	8.61	-9%	7.91	0.34	4%	8.61	-8%
Mo95	20.00	0.66	3%	16.7	20%	19.36	0.31	2%	16.7	16%
Sb121	0.13	0.01	7%	0.11	17%	0.14	-	-	0.11	27%
Cs133	0.14	0.04	26%	0.14	-1%	0.18	0.02	10%	0.14	29%
Ba137	78.57	1.61	2%	80.1	-2%	76.11	5.59	7%	80.1	-5%
La139	8.38	0.14	2%	8.99	-7%	7.71	0.52	7%	8.99	-14%
Ce140	22.55	0.57	3%	23.1	-2%	21.84	1.70	8%	23.1	-5%
Pr141	3.23	0.07	2%	3.43	-6%	2.93	0.10	3%	3.43	-15%
Nd146	15.74	0.30	2%	16.7	-6%	14.45	0.85	6%	16.7	-13%
Sm149	4.43	0.21	5%	4.75	-7%	3.84	0.83	22%	4.75	-19%
Eu151	1.62	0.11	7%	1.67	-3%	1.51	0.16	11%	1.67	-10%
Gd157	4.59	0.13	3%	5.26	-13%	4.22	0.88	21%	5.26	-20%
Tb159	0.72	0.03	5%	0.797	-9%	0.67	0.08	12%	0.797	-16%
Dy163	4.42	0.13	3%	4.84	-9%	3.91	0.18	4%	4.84	-19%
Ho165	0.83	0.03	4%	0.906	-8%	0.74	0.08	11%	0.906	-18%
Er167	2.27	0.06	3%	2.44	-7%	1.75	0.14	8%	2.44	-28%
Tm169	0.28	0.01	3%	0.324	-13%	0.28	0.04	14%	0.324	-14%
Yb173	1.67	0.14	8%	2.06	-19%	1.55	0.03	2%	2.06	-25%
Lu175	0.25	0.02	8%	0.286	-13%	0.20	0.02	11%	0.286	-31%
Hf177	2.82	0.17	6%	3.22	-12%	2.57	0.39	15%	3.22	-20%
Ta181	0.48	0.04	8%	0.555	-13%	0.40	0.10	25%	0.555	-27%
W182	0.46	0.05	11%	0.35	31%	0.47	0.16	35%	0.35	33%
Pb208	1.30	0.08	6%	1.38	-6%	1.33	0.14	10%	1.38	-4%
Th232	0.50	0.03	6%	0.548	-10%	0.46	0.01	1%	0.548	-16%
U238	0.47	0.03	6%	0.442	6%	0.45	0.02	4%	0.442	3%

GSD-2g 25 micron

Element	Mean	2sd	RSD%	Ref (ppm)	Ref (wt%)	Accuracy%
Li7	42.6	1.3	3%	42.57		0%
Be9	41.4	1.3	3%	45.24		-9%
B11	37.1	2.1	6%	40.45		-8%
Mg25	20225.3	712.9	4%	21060	3.51	-4%
Al27	66543.5	1273.4	2%	72554.72	13.26	-8%
Si29	260899.9	0.1	0%	Int Std		0%
Ca43	45769.4	1236.4	3%	45857.14	6.42	0%
Sc45	39.2	0.9	2%	41.93		-7%
Ti49	6938.5	250.2	4%	6956.79	1.15	0%
V51	43.8	0.1	0%	44.37		-1%
Cr53	48.1	5.5	11%	44.3		9%
Mn55	608.8	9.1	1%	641		-5%
Co59	39.4	1.9	5%	38.79		2%
Ni60	45.9	2.1	4%	45.99		0%
Cu65	38.0	4.6	12%	36.96		3%
Zn66	41.1	7.4	18%	48.44		-15%
As75	26.8	2.0	7%	29.02		-8%
Rb85	36.7	0.9	2%	38.34		-4%
Sr88	62.7	1.2	2%	66.27		-5%
Y89	38.5	1.2	3%	42.91		-10%
Zr90	42.2	2.9	7%	45.31		-7%
Nb93	44.8	3.0	7%	45.67		-2%
Mo95	38.2	0.2	0%	39.93		-4%
Sb121	37.3	0.2	1%	39.36		-5%
Cs133	32.0	0.0	0%	32.04		0%
Ba137	41.5	3.6	9%	44.6		-7%
La139	37.1	0.2	1%	39.56		-6%
Ce140	40.3	0.5	1%	42.47		-5%
Pr141	40.1	1.0	2%	42.32		-5%
Nd146	41.2	3.1	8%	44.27		-7%
Sm149	41.8	0.3	1%	43.3		-3%
Eu151	39.5	1.0	3%	41.8		-6%
Gd157	38.8	0.1	0%	42.23		-8%
Tb159	38.8	1.2	3%	42.54		-9%
Dy163	39.3	0.8	2%	43.18		-9%
Ho165	39.7	2.4	6%	43.2		-8%
Er167	36.9	1.9	5%	41.99		-12%
Tm169	40.1	0.9	2%	42.68		-6%
Yb173	40.8	3.7	9%	46.37		-12%
Lu175	42.2	2.0	5%	46.4		-9%
Hf177	36.4	4.4	12%	40.32		-10%
Ta181	40.6	2.2	5%	43.17		-6%
W182	43.9	1.8	4%	43.59		1%
Pb208	30.0	0.2	1%	30.67		-2%
Th232	39.1	1.1	3%	43.36		-10%
U238	40.8	0.3	1%	42.1		-3%

A8. Trace element composition of olivine.

	Ol$_1$ (2139A)												Mean	Std dev.	Ol$_1$ (22-45)										Mean	Std. Dev	Ol$_1$ (2139A)										Mean	Std. Dev	Ol$_1$ (22-45)										Ol$_1$ int. cluster (2139A)										Mean	Std dev.
Li7	5.27	4.71	<1.99	3.54	4.29	2.57	<2.18	3.1	3.89	2.48	5.66	3.95	1.071	14.9	0	<0.227	<0.00	13.9	14.4	0.47	1.7	2.54	2.02	2.06	2.08	0.3	1.27	5.25	3.5	4.375	0.875
Be9	<0.85	<1.11	<0.82	<0.81	<0.78	<1.18	<0.89	<0.00	<1.25	0.4	<1.20	0.4	0	<0.227	<0.00	-	-	-	<0.287	<0.27	<0.265	<0.215	-	-	-	<0.46	<0.29	0.06	0.06	0.06	0
B11	33.12	27.84	38.14	33.22	25.44	36.69	20.64	28.65	25	38.01	26.23	30.3	5.63	19.3	21.5	20.4	1.15	<2.11	<2.66	<1.97	<2.20	-	-	-	-	<2.46	28.44	36.56	32.5	4.06	
Mg25	297679	302262	279338	291031	294007	309795	283205	287192	310901	287592	293424	294220	9744	287971	284077	286024	1947	307566	301078	310003	305758	306101	3268	294631	294713	286346	296529	4184			
Al27	59.0	21.1	98.0	<6.57	8.89	831	<7.43	<7.12	<7.41	16.46	<7.12	172.4	296	<1.68	<1.72	-	-	28.4	52.2	31.3	12.7	31.1	14.1	13.41	<1.65	4.35	4.35	4.35	0		
Si29	191650	191650	191650	191650	191650	191650	191650	191650	191650	191650	191650	191650	0.0096209	191650	191650	191650	0	191650	191650	191650	191650	191650	0	191650	191650	191650	191650	0.005			
Ca43	<1683.03	<1558.27	<1604.76	<1597.68	<1542.24	<1655.73	2324	<1695.81	<1748.64	<1788.58	<1675.74	2324	0	<354.92	<353.35	-	-	<409.15	<553.62	<389.43	<452.35	-	-	-	-	<391.53	<436.75	<359.98	-	-	-	
Sc45	18.8	15.8	13.1	19.4	17.8	7.41	6.88	16.4	20.1	11.6	17.3	15.0	4.42	43.0	42.3	42.7	0.38	5.63	5.77	6.49	5.9	5.95	0.327	4.98	14.1	5.67	9.91	4.24			
Ti49	36.6	12.1	16.6	10.2	44.3	25.5	130	45.9	61.8	79.3	46.8	46.2	33.2	5.69	6.05	5.87	0.18	13.37	29.14	13.9	10.93	16.8	7.19	20.84	42.52	98.21	70.4	27.8			
V51	1.15	1.05	0.99	<0.58	<0.56	4.09	<0.51	1.45	0.96	<0.63	0.91	1.51	1.06	0.39	0.214	0.302	0.088	1.02	1.31	1.59	0.93	1.21	0.259	0.139	1.11	<0.138	1.11	0			
Cr53	<7.35	<6.23	<6.65	6.95	8.31	39.8	9.43	18.0	11.9	19.0	21.7	16.9	10.0	31.0	31.9	31.4	0.47	24.48	31.97	25.95	13.9	24.1	6.51	5.99	36.07	3.58	19.9	16.2			
Mn55	1929	2004	2267	2298	1961	2654	2753	2290	2094	2401	1887	2231	276.8	2781	2740	2760	20.6	1336.08	1507.12	1155.7	1423.44	1356	130	2601.15	2050.71	3092.8	2572	521.045			
Co59	266	277	247	270	275	178	265	252	275	279	277	260.2	27.8	225	222	224	1.60	147.65	153.92	149.13	152.21	151	2.47	205.34	294.46	285.56	290	4.45			
Ni60	3092	3087	1787	2458	2786	972	1545	2333	3024	2435	3043	2415	678	3178	3169	3173	4.75	3027.65	3012.81	3148.41	3129.75	3080	60.0	2981.47	3342.78	1658.24	2501	842			
Cu65	<1.80	<1.60	<1.72	<1.67	<1.58	<1.59	<1.61	<1.34	<1.87	<1.86	<1.65	-	-	67	0.64	0.655	0.015	0.41	1.31	0.59	0.68	0.7475	0.339	0.44	0.44	<0.34	0.44	0			
Zn66	61.6	70.6	66.1	71.6	66.3	65.9	84.5	58.3	64.8	167.6	62.3	76.3	29.6	84.9	81.3	83.1	1.83	55.77	62.34	46.65	57.75	55.6	5.70	85.05	75.59	91.96	83.8	8.19			
As75	<1.37	<1.19	<1.27	<1.40	<1.40	<1.31	<1.39	<1.37	<1.62	<1.66	-	-	-	<0.37	<0.40	-	-	0.4	0.52	0.38	0.42	0.43	0.0539	0.56	0.38	0.44	0.41	0.03			
Rb85	<0.53	<0.49	<0.49	<0.51	<0.44	<0.49	<0.53	<0.56	<0.53	<0.55	<0.47	-	-	<0.134	<0.141	-	-	<0.120	<0.176	<0.113	<0.132	-	-	<0.152	<0.118	<0.110	-	-			
Sr88	0.237	0.139	1.05	0.264	0.252	0.232	<0.00	0.24	<0.068	0.56	0.164	0.349	0.273	0.067	0.376	0.222	0.155	0.037	0.194	<0.0152	0.0129	0.0813	0.0803	0.829	0.0182	0.212	0.115	0.0969			
Y89	0.417	0.47	1.05	0.7	0.48	1.15	0.6	0.35	0.267	0.48	0.47	0.585	0.267	0.0274	0.048	0.0377	0.0103	0.0163	0.035	<0.026	0.0197	0.0237	0.00813	0.049	0.82	3.42	2.12	1.3			
Zr90	0.09	<0.136	0.21	0.088	0.45	0.3	0.18	<0.00	<0.109	<0.157	<0.104	0.220	0.126	0.0125	<0.031	0.0125	0	<0.026	0.060	<0.034	0.017	0.017	0	<0.035	0.153	1.23	0.692	0.539			
Nb93	0.024	<0.051	0.025	0.07	0.023	<0.00	0.026	0.078	<0.00	<0.00	<0.110	0.041	0.0235	<0.0153	<0.0158	-	-	<0.064	0.0089	0.0088	<0.0180	<0.0146	-	0.00885	5E-05	<0.00	-	<0.0197	<0.144	-	-	
Mo95	<0.50	<0.62	<0.34	0.32	<0.46	<0.43	<0.59	<0.57	<0.26	<0.27	<0.33	0.32	0	<0.147	<0.186	-	-	<0.085	0.102	0.128	0.093	0.107	<0.119	0.107	0	<0.147	<0.092	0.125	0.094	<0.031	0.08	0.087	0.007	
Sb121	<0.36	<0.28	<0.32	<0.28	<0.34	<0.38	<0.35	<0.38	<0.42	<0.27	<0.33	0.35	0	<0.091	<0.098	-	-	0.047	0	<0.037	<0.044	<0.039	0.107	0.1075	0.0129	0.125	<0.044	<0.031				
Cs133	<0.174	<0.138	<0.122	<0.157	<0.162	<0.168	<0.174	<0.173	0.32	<0.199	<0.181	0.285	0.314	<0.066	0.5	0.047	<0.042	0.026	0.095	<0.00	<0.041	0.0493	0.0323	0.83	0.027	0.072	0.0495	0.0225			
Ba137	0.098	0.098	0.56	0.097	0.19	0.32	<0.00	0.32	<0.237	0.64	1.09	0.00822	0.00723	0.0039	<0.00	0.0039	0	<0.0082	<0.00	<0.00	<0.00	-	<0.00	0.0019	0.0075	0.0047	0.0028				
La139	<0.00	0.014	<0.0314	0.014	<0.030	0.015	<0.00	0.031	<0.048	<0.00	<0.00	0.00822	0.00723	0.0039	<0.00	0.0039	0	<0.0082	<0.00	<0.00	<0.00	-	<0.00	0.0019	0.0075	0.0047	0.0028				
Ce140	<0.00	<0.00	<0.00	<0.00	0.012	0.026	<0.00	0.013	<0.00	0.027	<0.00	0.0195	0.00702	<0.00	<0.0115	-	-	<0.0102	0.0046	0.004	<0.00	0.0043	0.0003	<0.00	0.0017	0.0022	0.00195	0.00025			
Pr141	<0.024	<0.00	0.011	<0.022	<0.00	<0.023	<0.00	<0.00	<0.00	<0.00	<0.0236	-	-	<0.00	0.0029	0.0029	0	<0.00	<0.00	<0.00	0.0013	0.0013	0	0.0018	<0.00	<0.00	-	-			
Nd146	<0.139	0.12	<0.00	<0.00	<0.00	<0.00	<0.00	<0.00	<0.00	<0.00	0.064	0.092	0.028	<0.00	<0.040	-	-	0.015	<0.047	<0.00	0.0079	0.01145	0.00355	0.022	<0.00	0.011	0.011	0			
Sm149	0.075	<0.00	<0.167	<0.00	<0.00	<0.170	<0.00	<0.00	<0.00	<0.19	<0.00	-	-	<0.00	<0.00	-	-	<0.044	0.042	0.012	<0.047	0.027	0.015	<0.00	0.0099	<0.00	0.0099	0			
Eu151	0.038	<0.00	<0.043	<0.042	0.037	<0.00	<0.00	<0.00	0.021	<0.00	<0.00	0.032	0.00779	<0.00	0.0028	0.0028	0	<0.0113	0.0073	0.0032	<0.00	0.00525	0.00205	<0.00	<0.0117	0.0035	0.0035	0			
Gd157	<0.00	<0.00	<0.155	<0.153	<0.00	<0.223	0.077	<0.28	<0.00	<0.00	<0.00	0.077	0	0.019	0.01	0.0145	0.0045	<0.00	0.013	<0.00	0.0093	0.01115	0.00185	<0.053	<0.00	<0.00	-	-			
Tb159	<0.023	<0.00	0.011	<0.0222	<0.00	0.011	<0.00	<0.00	0.022	<0.0246	<0.0232	0.0347	0.00519	<0.0065	<0.0067	<0.00	<0.00	<0.00	<0.00	<0.0089	-	-	-	-	-	-	0.0063	0.0009			
Dy163	<0.133	<0.087	0.086	<0.00	0.118	0.088	<0.00	0.044	0.089	<0.099	<0.133	0.085	0.0236	0.011	0.0058	0.0084	0.0026	<0.0242	<0.00	<0.00	<0.0037	-	-	-	0.0036	0.0054	0.0072				
Ho165	0.01	0.02	0.022	0.01	<0.00	0.055	0.023	0.011	0.022	0.034	<0.00	0.0107	0.0135	<0.00	0.0058	0.0058	0	<0.00	0.0038	0.0017	0.0013	0.00227	0.00110	0.0018	0.0022	0.044	0.177	0.111	0.0665			
Er167	0.044	0.133	0.047	0.2	0.127	<0.00	0.099	<0.147	0.049	0.26	0.095	0.117	0.0694	<0.029	<0.029	-	-	<0.00	0.0084	<0.0246	<0.00	0.0084	0	<0.00	0.155	0.74	0.448	0.293			
Tm169	0.031	0.076	0.04	0.055	0.055	0.041	0.032	0.031	0.011	0.021	0.055	0.0407	0.0176	0.009	0.0041	0.00655	0.00245	0.0012	<0.00	<0.0074	<0.0060	0.0012	0	<0.0071	0.081	0.116	0.0985	0.0175			
Yb173	0.74	0.46	0.43	0.47	0.53	0.25	0.126	0.5	0.15	0.5	0.45	0.419	0.171	0.099	0.153	0.126	0.027	0.036	0.011	0.019	0.03	0.024	0.00967	0.03	1.05	0.463	0.757	0.294			
Lu175	0.113	0.116	0.04	0.102	0.118	0.03	0.042	0.021	0.062	0.041	0.091	0.0776	0.0361	0.0673	0.0585	0.0629	0.0044	0.0061	0.0018	0.0047	0.0025	0.00378	0.00172	0.0051	0.263	0.046	0.155	0.109			
Hf177	<0.00	<0.00	<0.00	<0.00	<0.00	<0.00	<0.00	0.05	<0.00	<0.114	<0.107	0.05	0	<0.0295	<0.00	-	-	<0.0270	<0.036	<0.00	<0.00	-	-	<0.00	0.019	0.182	0.101	0.0815			
Ta181	0.0093	<0.00	<0.00	<0.00	0.009	0.01	<0.00	0.01	<0.0230	<0.00	-	0.00958	0.000438	0.0013	<0.00	0.0013	0	<0.00	0.0018	<0.00	<0.00	0.0018	0	<0.00	<0.0057	0.0017	0.0017	0			
W182	<0.080	0.41	0.073	0.101	<0.00	<0.00	<0.00	<0.081	0.089	<0.189	<0.113	0.172	0.125	0.0141	<0.00	0.0141	0	<0.0206	<0.0274	<0.00	0.0046	0.0046	0	<0.00	0.0047	0.019	0.0119	0.00715			
Pb208	<0.147	<0.164	0.126	<0.137	0.151	<0.146	<0.171	<0.163	<0.130	<0.156	<0.155	0.139	0.0125	<0.048	<0.032	-	-	<0.040	<0.058	<0.036	0.044	0.044	0	<0.051	<0.052	<0.037	-	-			
Th232	<0.00	<0.00	<0.00	<0.00	<0.00	<0.00	<0.00	<0.00	<0.00	<0.00	<0.00	-	-	<0.00	<0.00	-	-	<0.00	<0.00	<0.00	<0.00	-	0	<0.00	<0.00	<0.00	-	-			
U238	<0.00	<0.00	<0.00	<0.00	<0.00	<0.00	<0.00	<0.00	<0.00	<0.00	<0.00	-	-	<0.00	<0.00	-	-	<0.00	<0.00	<0.00	<0.00	0.00092	0	<0.00	<0.00	<0.00	-	-			

A9. Trace element composition of Al-rich antigorite in sample 2139A.

	Al-rich Antigorite (Atg_1) (2139A)																									
	Atg vein and radial lamellae												*Mean*	*Std dev.*	Replacing Ol_1					*Mean*	*Std dev.*	Int. cluster			*Mean*	*Std dev.*
Li7	<0.40	<0.40	0.36	<0.46	<0.43	0.45	<0.40	<0.38	<0.40	<0.43	<0.41	<0.42	0.585	0.045	<0.36	<0.36	<0.35	<0.37	<0.38	-	-	<0.49	<0.48	<0.58	-	-
Be9	<0.153	<0.21	<0.205	<0.41	<0.251	<0.242	<0.00	<0.00	<0.215	<0.177	0.23	<0.174	0.23	0	<0.149	<0.155	<0.261	<0.162	<0.00	-	-	<0.273	0.21	<0.34	0.21	0
B11	8.97	10.4	8.49	11.8	12.5	11.5	9.64	10.57	7.62	5.21	7.85	5.45	9.16	2.25	20.9	20.3	22.1	17.1	17.9	19.7	1.87	9.84	24.5	8.99	14.4	7.10
Mg25	232175	235008	237492	242905	241417	238848	238216	234838	232037	240353	233293	234559	236762	3492	244100	247387	249278	246942	252067	247955	2641	232142	241308	236691	236714.0	3742
Al27	12358	14064	12869	18006	17102	13659	12597	12191	12017	15535	14727	14419	14129	1866	2487	1186	948	2896	2443	1992	775	12046	5346	9710	9034	2777
Si29	199129	199129	199129	199129	199129	199129	199129	199129	199129	199129	199129	199129	199129	0.0121	199129	199129	199129	199129	199129	199129	0.004	199129	199129	199129	199129	0
Ca43	<330.70	<313.43	<319.62	<393.62	<375.97	438.94	<328.86	<317.54	<333.49	<381.89	395.15	<363.76	417	21.9	<319.16	338.0	<305.78	<324.31	<340.80	338.0	0	<412.11	415	<505.06	415	0
Sc45	9.52	8.37	9.07	8.82	7.66	8.25	8.38	9.29	8.32	9.31	8.88	8.83	8.73	0.518	6.42	6.07	5.22	6.65	6.48	6.17	0.510	8.49	6.78	7.86	7.71	0.706
Ti49	26.7	27.8	62.6	25.1	26.2	25.9	27.6	29.0	23.8	29.9	34.4	25.9	30.4	10.0	34.6	21.2	19.2	24.1	14.7	22.8	6.63	21.2	28.3	23.7	24.4	2.93
V51	82.6	86.5	79.9	97.4	94.4	97.7	91	85	92	102	98	101	92.3	7.012	4.88	3	2.36	6.98	8.87	5.22	2.43	96	17.5	60.3	57.9	32.1
Cr53	3569	4221	3633	3871	4051	3482	3049	3607	3522	3614	3892	3363	3656	302	36.4	28.2	28.5	32.6	70.6	39.2	16.0	3762	106	609	1493	1618
Mn55	358	346	388	364	357	366	336	404	335	299	328	285	347	32.4	316	263	313	274	248	283	27.4	363	410	682	485	141
Co59	55.5	50.2	50.8	37.5	38.1	38.4	55	50	56	56	53	55	49.6	7.046765	46.2	56.4	57.4	44.4	58.2	52.5	5.94	53.4	60.6	58.1	57.4	2.97
Ni60	410	184	221	226	227	190	325	255	287	433	379	438	298	91.5	119	271	170	97.3	423	216	119	169	1010	1405	861	516
Cu65	<0.30	0.46	<0.29	0.34	0.43	0.4	0.48	0.42	0.35	0.37	0.94	0.33	0.452	0.170	0.37	0.69	0.41	0.66	0.39	0.504	0.141	0.41	<0.37	0.92	0.665	0.255
Zn66	29.8	28.2	27.7	31.4	31.2	31.1	30.0	31.1	29.5	32.7	30.1	30.1	30.2	1.33	24.1	22.5	23.2	22.5	22.2	22.9	0.692	29.7	26.8	29.4	28.6	1.28
As75	<0.23	<0.26	<0.26	<0.38	<0.32	<0.37	<0.32	<0.26	<0.27	<0.38	<0.33	<0.26	-	-	<0.30	<0.26	0.3	<0.39	<0.29	0.3	0	<0.34	<0.50	<0.46	-	-
Rb85	<0.101	0.211	<0.091	0.303	<0.111	0.127	<0.091	<0.095	<0.094	<0.120	<0.105	<0.103	0.257	0.0719	<0.103	<0.098	0.088	<0.105	<0.099	0.088	0	<0.125	<0.116	<0.136	-	-
Sr88	0.203	0.307	0.326	0.728	0.607	3.53	0.269	0.346	0.18	0.136	0.383	0.106	0.593	0.903	0.365	0.663	0.171	0.51	0.144	0.371	0.198	0.113	0.45	0.543	0.369	0.185
Y89	0.21	0.224	0.224	0.319	0.258	0.242	0.15	0.187	0.117	0.117	0.162	0.082	0.191	0.0654	0.126	0.094	0.052	0.141	0.07	0.0966	0.0333	0.105	0.057	0.021	0.061	0.0344
Zr90	0.109	0.125	0.13	0.355	0.26	0.172	0.066	0.146	0.042	0.049	0.139	0.027	0.135	0.0907	0.172	0.104	0.088	0.144	<0.022	0.127	0.0330	0.044	0.337	<0.055	0.1905	0.1465
Nb93	0.0038	<0.0178	<0.0143	<0.0175	0.0039	<0.0117	<0.0148	<0.0176	0.0036	<0.0171	<0.00	0.0072	0.00463	0.001491	<0.0143	<0.0149	<0.0102	<0.0108	<0.0165	-	-	0.0039	<0.0231	<0.00	0.0039	0
Mo95	0.071	<0.083	<0.105	<0.100	0.037	<0.054	0.074	<0.082	<0.070	<0.057	<0.075	<0.079	0.0607	0.0168	<0.067	<0.085	<0.107	<0.088	<0.078	-	-	0.092	<0.088	<0.110	0.092	0
Sb121	<0.083	<0.078	<0.085	<0.081	<0.061	<0.073	<0.075	0.073	<0.087	<0.078	<0.079	<0.071	0.073	0	<0.071	<0.070	<0.062	<0.076	<0.056	-	-	<0.078	<0.090	<0.092	-	-
Cs133	0.034	0.031	<0.033	0.16	0.15	0.045	<0.030	<0.027	<0.035	<0.037	<0.029	<0.034	0.084	0.0582	<0.030	<0.034	<0.031	<0.031	<0.029	-	-	<0.040	<0.037	<0.048	-	-
Ba137	0.165	0.136	0.209	1.31	0.8	2.96	0.147	0.266	0.032	0.72	0.217	0.265	0.602	0.795	0.131	<0.065	0.138	0.11	0.091	0.118	0.0184	<0.058	0.45	0.71	0.58	0.13
La139	0.0139	0.0023	0.0077	0.0069	0.0047	0.0137	0.0071	0.028	<0.0065	0.0044	0.007	0.0043	0.00909	0.006924	0.0102	0.0041	0.0064	0.0095	0.0021	0.00646	0.00309	0.0048	<0.00	<0.0101	0.0048	0
Ce140	0.0347	0.0287	0.0401	0.0447	0.0334	0.0382	0.0222	0.0431	0.0156	0.0156	0.0147	<0.0089	0.0301	0.0109	0.0107	0.0164	<0.00	0.0084	0.0018	0.009325	0.00523	0.0168	0.0032	<0.00	0.01	0.0068
Pr141	<0.0046	0.005	0.0051	<0.0076	<0.0052	0.0049	0.0048	0.0033	0.0016	<0.0052	0.0052	<0.0052	0.00427	0.001244	0.0015	<0.0046	0.0015	0.0014	0.003	0.00185	0.000665	0.0017	<0.00	0.0024	0.00205	0.00035
Nd146	<0.00	0.03	0.02	0.049	0.02	<0.00	<0.00	0.039	0.0093	0.019	<0.029	<0.0306	0.0266	0.0126	0.0086	0.0088	<0.00	0.0081	<0.030	0.0085	0.000294	0.051	<0.034	<0.043	0.051	0
Sm149	<0.00	<0.00	0.013	0.012	<0.039	<0.037	<0.00	<0.032	<0.048	<0.039	<0.063	0.011	0.0120	0.000816	<0.032	<0.048	<0.033	<0.035	<0.053	-	-	<0.043	<0.00	<0.00	-	-
Eu151	<0.0090	0.0128	0.0033	<0.0103	<0.00	<0.0097	0.0094	<0.0085	<0.00	<0.0143	<0.0095	0.003	0.00713	0.004154	<0.0146	<0.0124	<0.00	0.0079	0.0029	0.0054	0.0025	<0.0158	0.0051	0.0094	0.00725	0.00215
Gd157	0.012	0.07	0.012	<0.038	0.024	<0.00	0.049	0.047	0.011	0.033	<0.035	0.011	0.0299	0.0202	<0.0306	<0.055	0.011	0.0095	0.011	0.0105	0.000707	<0.070	<0.00	<0.051	-	-
Tb159	0.0066	0.0067	0.0069	0.0099	0.0102	0.0016	0.0049	0.0134	0.0095	0.0063	0.0083	0.0077	0.00767	0.002844	0.0029	0.0044	<0.0044	0.0041	0.003	0.0036	0.000660	<0.0058	<0.00	<0.00	-	-
Dy163	0.035	0.03	0.049	0.116	0.042	0.047	0.027	0.03	0.02	0.02	0.0138	<0.021	0.0391	0.0266	<0.00	<0.027	<0.00	0.023	0.0124	0.0177	0.0053	0.0071	<0.024	<0.00	0.0071	0
Ho165	<0.0047	0.0071	0.0091	0.015	<0.0053	0.0199	0.0085	0.0136	0.0048	0.0032	<0.0050	<0.00	0.0102	0.00525	<0.0062	<0.00	<0.0044	0.0027	0.0045	0.0036	0.0009	<0.0058	0.0053	0.0073	0.0063	0.001
Er167	<0.00	0.0075	0.032	<0.024	0.023	0.037	<0.021	<0.0200	0.014	<0.024	0.0075	<0.00	0.0202	0.0115	0.02	0.0066	0.0068	0.0122	<0.0224	0.0114	0.00545	0.038	0.012	<0.00	0.025	0.013
Tm169	<0.0044	0.0063	<0.0042	<0.0051	<0.00	0.0016	<0.00	<0.0042	<0.0062	0.0045	0.0047	<0.0069	0.00428	0.001695	<0.0041	0.0028	0.0073	0.0013	0.0029	0.00358	0.00224	<0.0095	0.005	<0.00	0.005	0
Yb173	0.0096	<0.0259	<0.00	0.019	0.0097	<0.00	<0.026	0.0097	0.0092	<0.0300	0.0095	<0.00	0.0111	0.00353	0.017	0.017	0.017	<0.00	<0.00	0.017	0	0.02	0.03	<0.00	0.025	0.005
Lu175	<0.0045	<0.0043	<0.00	0.0031	0.0048	<0.00	0.0031	0.0048	<0.00	<0.0050	<0.00	0.0015	0.00346	0.00124	<0.0041	<0.0043	0.0014	0.0051	<0.00	0.00325	0.00185	<0.0055	<0.00	<0.00	-	-
Hf177	<0.00	<0.0207	<0.00	0.015	0.023	<0.023	<0.00	<0.020	<0.00	<0.00	<0.00	0.0072	0.0151	0.00645	<0.0201	<0.00	<0.0287	<0.00	<0.00	-	-	0.016	<0.038	<0.00	0.016	0
Ta181	<0.00	<0.00	<0.0059	<0.00	<0.00	<0.00	<0.00	0.0016	<0.00	0.0015	<0.0047	<0.00	0.00155	0.00005	<0.00	<0.00	<0.00	<0.0044	<0.00	-	-	<0.00	<0.00	<0.0096	-	-
W182	<0.0163	0.0058	0.018	<0.00	<0.00	0.0057	0.018	<0.0155	<0.0162	<0.0259	<0.017	<0.0180	0.0119	0.006125	0.071	0.026	0.059	0.019	0.026	0.0402	0.0208	0.048	0.092	0.28	0.14	0.101
Pb208	<0.040	<0.034	<0.035	<0.037	0.048	<0.039	<0.036	<0.037	0.037	<0.037	<0.025	<0.035	0.0425	0.0055	<0.033	<0.030	<0.037	<0.038	<0.032	-	-	<0.048	<0.038	<0.053	-	-
Th232	<0.00	<0.00	<0.00	<0.00	0.0017	<0.00	<0.00	<0.00	<0.00	<0.00	<0.00	<0.00	0.0017	0	<0.00	<0.00	<0.00	<0.00	<0.00	-	-	<0.00	<0.00	<0.00	-	-
U238	<0.00	0.0012	0.0012	0.0012	0.0012	<0.00	<0.00	<0.00	<0.00	<0.00	<0.00	<0.00	0.0012	0	<0.00	<0.00	<0.00	0.00094	<0.00	0.00094	0	<0.00	0.0018	<0.00	0.0018	0

A10. Trace element composition of Al-rich antigorite in sample 22-45.

	Al-rich antigorite (Atg_1) (22-45)																			
	V1 rim			*Mean*	*Std dev.*	**Replacing Ol1**	**Vein V2**								*Mean*	*Std dev.*	**Microcracks**			*Mean*	*Std dev.*
Li7	<0.49	<0.51	<0.51	-	-	<0.56	<0.53	<0.56	<0.60	<0.57	<0.58	<0.62	<0.62	<0.64	-	-	0.67	<0.41	<0.33	0.67	0
Be9	0.048	<0.220	0.048	0.048	0	<0.00	<0.39	<0.24	<0.259	<0.35	0.115	0.116	<0.37	0.06	0.251	0.0262	<0.16	<0.00	0.29	0.29	0
B11	12.9	12.2	11.9	12.3	0.433	14.2	12.6	11.1	10.7	12.2	11.3	12.6	12.1	16.2	12.3	1.59	16	27.5	15.1	19.5	5.65
Mg25	236615	232677	238136	235809	2300	241211	238306	236572	242185	242880	239746	242375	243051	239751	240608	2230	246412	246422	245505	246113	430
Al27	12655	13656	13187	13166	409	11170	11918	11451	11232	11073	12175	11578	11467	11596	11561	330	1051	1297	1773	1374	300
Si29	199129	199129	199129	199129	0.009428	199129.14	199129	199129	199129	199129	199129	199129	199129	199129	199129	0.0139	199129	199129	199129	199129	0.00942809
Ca43	<354.44	<324.97	<350.06	-	-	<368.50	<332.67	<369.79	<384.51	<375.54	<386.30	<402.85	<398.37	<409.09	-	-	<249.54	<278.44	1173	1173	0
Sc45	10.5	10.7	10.6	10.6	0.06549	9.39	9.12	9.02	9	9.51	10.1	9.4	10.1	10.3	9.56	0.485	25.7	33.8	25.9	28.5	3.79
Ti49	21.7	22.6	18.7	21.0	1.70	23.6	19.5	20.6	16.5	31.7	22.2	25.0	22.6	28.0	23.3	4.55	55.9	11.7	20.5	29.4	19.1
V51	67.9	68.5	71.5	69.3	1.59	43.7	70.3	71.3	69.1	66.0	69.5	69.5	71.3	66.2	69.2	1.93	6.34	8.67	9.05	8.02	1.20
Cr53	1700	1477	1648	1608	95.2	344.4	1124	1512	1418	1231	2271	1810	1694	1873	1617	350	27.1	30.5	110	56.0	38.5
Mn55	375	331	352	353	17.9	375	345	368	376	409	370	360	369	362	370	17.1	516	270	533	440	120
Co59	57.7	59.1	59.7	58.8	0.847	62.8	66.9	67.9	67.4	64.9	65.7	65.1	67.4	64.8	66.3	1.19	64.8	56.3	54.1	58.4	4.62
Ni60	894	1001	967	954	44.5	1284	913	880	888	846	745	738	701	689	800.0	85.2	1333	1343	744	1140	280
Cu65	0.61	0.49	<0.42	0.55	0.06	0.69	0.71	0.56	0.67	0.54	<0.41	<0.45	0.41	0.54	0.572	0.0975	<0.34	<0.27	<0.25	-	-
Zn66	27.1	28.7	28.0	27.9	0.633	28.9	28.2	28.4	28.4	27.7	29.2	29.1	30.1	28.5	28.7	0.686	23.5	21.1	22.6	22.4	0.994
As75	<0.39	<0.38	<0.40	-	-	<0.47	<0.33	<0.36	<0.44	<0.45	<0.34	<0.41	<0.47	<0.50	-	-	0.33	<0.46	<0.29	0.33	0
Rb85	<0.137	<0.130	<0.134	-	-	<0.143	0.18	0.233	0.4	0.214	<0.155	0.215	0.194	<0.158	0.239	0.0738	<0.087	<0.121	<0.087	-	-
Sr88	0.181	0.149	0.168	0.166	0.0131	0.121	0.508	0.741	0.793	0.959	0.806	0.741	0.494	0.619	0.708	0.148	0.317	0.143	1.189	0.550	0.458
Y89	0.496	0.284	0.459	0.413	0.0925	0.086	0.377	0.849	0.896	0.917	1.01	0.736	0.593	0.981	0.795	0.202	0.252	0.045	0.528	0.275	0.198
Zr90	0.432	0.451	0.57	0.484	0.0611	0.1	0.542	0.861	1.2	0.903	1.58	1.13	1.01	1.18	1.05	0.284	0.303	0.219	0.262	0.261	0.0343
Nb93	0.0033	0.0065	<0.0212	0.0049	0.0016	<0.0165	<0.0153	0.0072	<0.0176	0.0038	<0.0238	<0.00	<0.0180	<0.0264	0.0055	0.0017	0.013	<0.0181	<0.0145	0.013	0
Mo95	<0.128	0.063	<0.073	0.063	0	<0.136	<0.125	0.079	<0.117	<0.157	<0.158	<0.085	<0.084	<0.215	0.079	0	0.085	<0.121	<0.084	0.085	0
Sb121	<0.119	<0.095	<0.101	-	-	<0.088	<0.109	<0.106	<0.102	<0.114	<0.087	<0.114	<0.132	<0.130	-	-	<0.072	<0.070	<0.065	-	-
Cs133	<0.037	<0.037	<0.044	-	-	<0.043	0.156	0.269	0.369	0.281	0.213	0.225	0.077	0.096	0.211	0.0919	<0.033	<0.037	<0.024	-	-
Ba137	<0.065	0.196	0.112	0.154	0.042	0.092	0.97	1.21	1.43	1.67	1.19	1.04	0.73	0.88	1.14	0.284	0.39	0.162	0.61	0.387	0.183
La139	0.0078	0.0078	0.0096	0.0084	0.000849	<0.00	0.0023	0.0108	0.0091	0.0023	0.0117	0.0108	0.0023	0.0122	0.00769	0.00426	<0.00	<0.0076	<0.00	-	-
Ce140	0.0161	0.0077	0.0307	0.0182	0.009503	0.0118	0.0254	0.0355	0.0275	0.0471	0.058	0.0276	0.0221	0.0381	0.0352	0.0115	0.0042	<0.0093	0.0236	0.0042	0.0097
Pr141	0.0014	0.0028	0.0041	0.00277	0.001103	0.0032	0.0032	0.0046	0.0096	<0.00	0.0099	0.005	0.0016	0.0104	0.00633	0.00332	0.007	<0.0076	0.0077	0.00735	0.00035
Nd146	0.0082	0.024	0.048	0.0267	0.0164	0.0095	<0.038	0.063	0.029	0.114	0.078	0.055	0.029	0.072	0.0629	0.0275	0.021	<0.00	0.011	0.016	0.005
Sm149	<0.00	0.01	0.031	0.0205	0.0105	<0.00	0.049	<0.051	0.024	<0.053	0.012	<0.057	0.049	0.026	0.032	0.0147	<0.035	<0.00	<0.00	-	-
Eu151	0.0053	<0.0120	0.0129	0.0091	0.0038	<0.00	0.0062	0.0205	<0.0143	0.0247	0.0095	0.0192	0.0063	0.0067	0.0133	0.00731	<0.0128	<0.00	0.0111	0.0111	0
Gd157	0.053	<0.043	0.0094	0.0312	0.0218	<0.00	0.034	0.064	0.067	0.067	0.103	0.081	0.087	0.121	0.078	0.0248	<0.033	<0.00	0.054	0.054	0
Tb159	0.0097	0.0082	0.0068	0.00823	0.00118	0.0032	0.0032	0.0167	0.02	0.0159	0.0311	0.0082	0.0065	0.0223	0.0155	0.00864	0.0055	0.005	0.0077	0.00607	0.00117
Dy163	0.076	0.031	0.045	0.0507	0.018803	<0.028	0.052	0.092	0.09	0.116	0.099	0.067	0.066	0.132	0.0893	0.0252	0.07	0.01	0.14	0.0733	0.0531
Ho165	0.0126	0.0069	0.0244	0.0146	0.007288	<0.0070	0.0178	0.0243	0.0185	0.0303	0.0317	0.0241	0.0326	0.06	0.0299	0.0125	0.0138	0.0025	0.0192	0.0118	0.00696
Er167	0.053	0.03	0.09	0.0577	0.0247	0.007	0.057	0.087	0.112	0.074	0.223	0.109	0.097	0.113	0.109	0.0469	0.015	0.011	0.045	0.0237	0.0152
Tm169	0.0091	<0.0084	0.0097	0.0094	0.0003	0.0045	0.0061	0.01	0.009	0.0135	0.0216	0.0164	0.0153	0.0129	0.0131	0.00452	0.0033	<0.00	0.0072	0.00525	0.00195
Yb173	0.023	0.031	0.061	0.0383	0.0164	0.0088	0.045	0.101	0.132	0.106	0.136	0.078	0.086	0.085	0.0961	0.0278	0.096	<0.00	0.117	0.1065	0.0105
Lu175	0.0115	0.0064	0.0126	0.0102	0.002701	<0.0092	0.0136	0.0213	0.0187	0.0164	0.0307	0.0263	0.0183	0.037	0.0228	0.00743	0.0097	0.0047	0.0144	0.0096	0.00396
Hf177	0.032	0.025	0.035	0.0307	0.00419	<0.0316	<0.029	0.069	0.036	0.043	0.089	0.06	0.078	0.067	0.0631	0.0173	0.025	0.046	0.026	0.0323	0.00967
Ta181	<0.0085	<0.00	<0.0060	-	-	0.0015	<0.00	<0.0063	<0.00	<0.00	0.0015	<0.00	<0.00	0.0032	0.00235	0.00085	<0.00	<0.00	0.0036	0.0036	0
W182	0.0144	<0.00	0.0188	0.0166	0.0022	0.022	<0.00	0.0052	0.0054	0.0163	<0.0241	<0.00	0.0111	0.0059	0.00878	0.00435	0.083	0.0086	0.042	0.0445	0.0304
Pb208	<0.042	<0.038	<0.036	-	-	<0.052	<0.037	<0.043	0.038	<0.049	<0.047	<0.047	<0.048	<0.047	0.038	0	<0.026	<0.038	<0.027	-	-
Th232	<0.00	<0.00	<0.00	-	-	<0.00	<0.00	<0.00	<0.00	<0.00	<0.00	<0.00	<0.00	<0.00	-	-	<0.00	<0.00	<0.00	-	-
U238	0.00091	<0.00	0.0009	0.000905	0	0.001	<0.00	<0.00	0.0021	<0.00	<0.00	<0.00	<0.00	<0.00	0.0021	0	<0.00	<0.00	<0.00	-	-

A11. Trace element composition of Al-free antigorite and Ti-clinohumite.

	Al-free antigorite (Atg_2)																Ti-clinohumite													
	2139A			Mean	Std dev.	22-45		Mean	Std dev.	Int. Cluster (2139A)	V1 (22-45)		Mean	Std dev.	V3 (22-45)		Mean	Std dev.	2139A		Mean	Std dev.
Li7	0.99	<0.43	<1.78	<1.47	0.99	0	6.07	<1.60	6.07	0	<3.18	9.74	8.18	7.98	8.633	0.787	1.96	10.9	6.44	4.48	2.6	2.26	2.43	0.17
Be9	<0.27	0.21	0.4	0.79	0.467	0.241	0.85	<1.09	0.85	0	<1.32	0.049	0.146	0.05	0.0817	0.0455	<0.249	0.054	0.054	0	<0.33	<0.43	-	-
B11	105	99	172	187	141	39.0	34	89.7	61.9	27.9	114	9.0	10.1	9.7	9.577	0.443	50.5	36.9	43.7	6.77	30.6	28.9	29.7	0.855
Mg25	345115	303263	264977	265286	294660.4	33029	286771	272130	279450.5	7321	649732	269409	273618	277333	273453	3237	275942	277589	276766	824	268542	271581	270061	1519
Al27	<1.56	1.61	41.36	17.31	20.1	16.3	<5.70	<5.50	-	-	2885.61	3.04	3.2	3.77	3.337	0.313	6.74	2.3	4.52	2.22	1764	19.3	891	872
Si29	199129	199129	199129	199129	199129.1	0.0179	199129	199129	199129.2	0	199129	168278	168278	168278	168278	0.00943	168278	168278	168278	0.01	168278	168278	168278	0
Ca43	625.98	<380.63	<1326.54	<1177.37	626	0	<1082.86	<1096.18	-	-	<2642.64	<321.01	<332.82	<339.28	-	-	<387.87	<364.24	-	-	946	<497.65	946	0
Sc45	23.7	19.7	20.6	26.1	22.5	2.55	22.5	51.3	36.9	14.4	4.91	55.3	65.3	53.5	58.1	5.19	26.1	81.2	53.6	27.6	25.7	20.8	23.2	2.43
Ti49	49.0	109.3	31.1	15.5	51.2	35.6	22.1	<5.15	22.1	0	139	22951	21637	22955	22515	620	24582	26113	25348	765	13966	14680	14323	357
V51	1.59	1.13	0.58	0.86	1.04	0.372	0.45	<0.43	0.45	0	1.51	24.6	26.9	25.4	25.6	0.937	16.1	18.6	17.4	1.28	15.3	5.83	10.6	4.75
Cr53	42.5	29.6	9.26	12.5	23.5	13.4	8.74	28.5	18.6	9.89	238	104	104	89	99.2	7.23	108	149	129	20.5	160	52.3	106	53.7
Mn55	3066	2423	1848	1625	2241	558	2520	1483	2001	519	3434	2884	2880	2806	2857	36.0	2598	3612	3105	507	2535	2551	2543	7.63
Co59	318	337	241	232	282	46.0	290	372	331	41.1	192	182	182	180	181	0.796	179	199	189	10	168	197	183	14.3
Ni60	3816	3382	3088	3027	3328	312	3578	3493	3535	42.8	795	2030	2050	2037	2039	8.29	2114	2156	2135	21.0	1734	1996	1865	131
Cu65	1.39	3.39	5.47	3.13	3.35	1.45	<1.17	<1.26	-	-	<2.20	1.96	1.61	1.93	1.83	0.158	1.79	1.85	1.82	0.03	0.95	1.87	1.41	0.46
Zn66	21.2	33.3	10.4	8.66	18.4	9.87	71.18	24.7	47.9	23.2	25.77	87.0	87.6	87.6	87.4	0.314	85.1	88.9	87.0	1.86	69.9	84.4	77.1	7.27
As75	<0.32	<0.27	<0.90	<1.26	-	-	<1.64	<1.4	-	-	2.43	<0.33	<0.33	<0.37	-	-	<0.36	<0.40	-	-	<0.47	<0.44	-	-
Rb85	<0.117	<0.108	<0.43	<0.40	-	-	<0.44	0.35	0.35	0	<0.75	<0.133	<0.124	<0.136	-	-	<0.155	<0.152	-	-	<0.148	<0.145	-	-
Sr88	3.24	5.06	3.62	4.06	4.00	0.680	5.71	4.26	4.99	0.725	2.25	0.094	<0.0128	0.16	0.127	0.033	0.251	<0.146	0.251	0	1.57	0.623	1.10	0.474
Y89	0.834	0.711	0.76	0.87	0.794	0.0621	0.73	0.48	0.605	0.125	1.96	0.102	0.204	0.042	0.116	0.0669	0.0247	0.225	0.125	0.100	0.907	0.865	0.886	0.021
Zr90	0.185	0.283	0.27	0.097	0.209	0.0747	0.67	<0.14	0.67	0	1.03	7.17	9.6	7.62	8.13	1.06	5.86	8.83	7.35	1.49	0.88	1.29	1.09	0.205
Nb93	<0.0187	<0.0169	<0.062	<0.039	-	-	<0.00	0.023	0.023	0	<0.085	0.647	0.624	0.682	0.651	0.0238	0.03	<0.024	0.03	0	<0.022	0.0045	0.0045	0
Mo95	0.106	<0.111	<0.20	<0.178	0.106	0	<0.22	<0.21	-	-	<0.55	<0.175	0.127	<0.104	0.127	0	<0.081	<0.182	-	-	<0.192	-	-	-
Sb121	<0.076	<0.099	<0.31	0.21	0.21	0	<0.33	<0.31	-	-	0.56	<0.102	<0.095	<0.106	-	-	<0.098	<0.103	-	-	<0.111	<0.105	-	-
Cs133	<0.043	<0.036	0.167	<0.116	0.167	0	<0.141	<0.121	-	-	<0.25	<0.043	<0.043	<0.043	-	-	<0.046	<0.041	-	-	<0.040	<0.050	-	-
Ba137	1.77	4.25	2.4	1.77	2.55	1.02	8.51	2.02	5.27	3.25	<0.35	0.071	<0.064	0.278	0.175	0.104	0.016	0	0.016	0	1.24	1.24	1.24	0
La139	0.0097	0.0058	0.016	<0.00	0.0105	0.00420	<0.00	<0.00	-	-	<0.00	0.0039	<0.0089	<0.00	0.0039	0	<0.00	0.0022	0.0022	0	0.039	0.055	0.047	0.008
Ce140	<0.00	0.0179	0.04	<0.0200	0.0290	0.0111	0.015	<0.00	0.015	0	0.103	<0.0076	0.0034	0.0018	0.0026	0.0008	0.0019	0.0019	0.0019	0	0.076	0.064	0.07	0.006
Pr141	<0.0057	0.0041	<0.019	<0.00	0.0041	0	<0.00	<0.037	-	-	<0.00	<0.00	<0.0063	<0.0065	-	-	0.0032	0.0016	0.0024	0.0008	0.0139	0.0039	0.0089	0.005
Nd146	0.014	0.037	0.067	<0.00	0.0393	0.0217	<0.00	<0.00	-	-	<0.212	<0.037	<0.053	<0.054	-	-	<0.00	<0.00	-	-	0.083	0.105	0.094	0.011
Sm149	<0.00	<0.038	<0.00	<0.172	-	-	<0.00	<0.161	-	-	<0.00	<0.00	<0.00	<0.00	-	-	<0.054	<0.00	-	-	<0.00	<0.053	-	-
Eu151	<0.0111	<0.0100	<0.00	0.021	0.021	0	<0.041	<0.00	-	-	0.04	<0.00	0.0027	0.0027	0.0027	0	0.003	<0.0137	0.003	0	0.0045	0.0113	0.0079	0.0034
Gd157	<0.00	<0.00	<0.127	<0.160	-	-	<0.16	0.22	0.22	0	0.14	<0.043	0.0096	<0.045	0.0096	0	0.011	<0.050	0.011	0	0.097	0.055	0.076	0.021
Tb159	<0.0057	0.0021	<0.00	<0.0165	0.0021	0	0.025	0.01	0.0175	0.0075	<0.036	<0.00	<0.00	<0.00	-	-	0.0016	0.0015	0.00155	0.00005	0.0138	0.0192	0.0165	0.0027
Dy163	0.058	0.043	0.137	<0.118	0.0793	0.0412	<0.00	<0.088	-	-	0.29	<0.0253	<0.025	<0.0260	-	-	0.0128	0.031	0.0219	0.0091	0.133	0.128	0.1305	0.0025
Ho165	0.0141	0.0131	0.011	0.044	0.0206	0.0136	0.038	<0.032	0.038	0	<0.052	<0.0062	<0.0063	0.0014	0.0014	0	0.0032	<0.0071	0.0032	0	0.0254	0.041	0.0332	0.0078
Er167	0.274	0.224	0.048	0.19	0.184	0.0840	0.055	0.135	0.095	0.04	0.32	<0.028	0.092	<0.028	0.092	0	<0.031	0.123	0.123	0	0.062	0.147	0.1045	0.0425
Tm169	0.104	0.065	0.052	0.072	0.0733	0.0191	0.024	0.023	0.0235	0.0005	0.06	0.0262	0.0392	0.0054	0.0236	0.0139	0.009	0.03	0.0195	0.0105	0.0263	0.0463	0.0363	0.01
Yb173	1.31	0.99	0.89	0.94	1.03	0.164	<0.13	0.35	0.35	0	0.12	0.344	0.702	0.234	0.427	0.200	0.094	0.632	0.363	0.269	0.603	0.319	0.461	0.142
Lu175	0.346	0.253	0.104	0.245	0.237	0.0864	0.059	0.137	0.098	0.039	<0.00	0.114	0.181	0.104	0.133	0.0342	0.0496	0.197	0.123	0.0737	0.109	0.086	0.0975	0.0115
Hf177	0.021	0.041	<0.00	<0.076	0.031	0.01	<0.00	0.048	0.048	0	<0.17	0.296	0.292	0.256	0.281	0.0180	0.384	0.431	0.408	0.0235	0.064	0.045	0.0545	0.0095
Ta181	0.0022	<0.00	<0.0173	0.01	0.0061	0.0039	<0.00	<0.00	-	-	<0.00	0.0065	0.0039	0.0107	0.00703	0.00280	0.0044	<0.00	0.0044	0	<0.0089	<0.00	-	-
W182	0.731	0.379	0.47	0.48	0.515	0.131	0.27	0.294	0.282	0.012	2.96	0.029	0.027	0.0198	0.0253	0.00395	0.497	1.064	0.781	0.284	0.172	0.096	0.134	0.038
Pb208	<0.048	<0.043	<0.124	0.185	0.185	0	<0.138	0.378	0.378	0	<0.22	<0.033	<0.040	<0.032	-	-	<0.042	<0.052	-	-	0.037	<0.045	0.037	0
Th232	<0.00	<0.00	<0.00	<0.00	-	-	<0.00	<0.00	-	-	<0.00	<0.00	<0.00	<0.00	-	-	<0.00	<0.00	-	-	<0.00	<0.00	-	-
U238	<0.00	<0.00	<0.00	<0.00	-	-	<0.00	<0.00	-	-	<0.00	<0.00	<0.00	<0.00	-	-	<0.00	<0.00	-	-	<0.00	-	0.0013	0

A12. Trace element compositon of calcite (sample 22-45) and brucite (sample 2139A).

	Calcite (22-45A)					Brucite (2139A)															
				Mean	Std dev,	Pure brucite					Mean	Std dev.	Atg + Brc				Mean	Std dev.			
Li7	<0.41	<0.39	<0.40	-	-	<0.29	<1.46	<0.32	<0.40	-	-	-	0.82	0.84	0.83	0.01					
Be9	<0.31		0.08	<0.00	0.08	0	<0.114		0.28	<0.14	0.077	0.179	0.102	<0.00	<0.00	-	-	-			
B11	<1.50	<1.37	1.7	1.7	1.7	0	2.19	18.6	6.72	<1.66	9.17	6.92	29.0	32.5	30.7	1.76					
Mg25	352	842	198	464	275	422173.25	422173.3	422173	422173	422173.3	0.0335	301552	301552	301552	301552.3	0.015					
Al27	1.63	17.6	1.6	6.94	7.53	11.8	714	1.32	4.92	183	306	41.9	49.2	45.6	3.64						
Si29	531	650	393	525	105	1655.07	29386.92	9281	3441	10941	11017	104304	107022	105662.9	1359						
Ca43	400233	400233	400233	400233	0.0141	287	<1196.59	<286.00	339	313	26.0	2196	9580	5888	3692						
Sc45	<0.35	<0.34	<0.36	-	-	<0.30	<1.40	0.95	<0.40	0.95	0	4.25	4.92	4.59	0.335						
Ti49	2.3	<0.92	<1.45	2.3	0	46.95	34.92	80.3	102	66.1	26.7	134	114	124	10.1						
V51	<0.077	<0.101	<0.100	-	-	0.125	1.13	0.171	<0.133	0.475	0.463	0.79	0.94	0.865	0.075						
Cr53	<1.35	<1.33	<1.27	-	-	7.85	98.8	154	100	90.1	52.3	123	167	145	22.1						
Mn55	693	799	630	707	69.8	1564	1516	1724	1648	1613	79.8	2263	2227	2245	18.4						
Co59	<0.109	0.297	<0.104	0.297	0	161	100	58.4	61.3	95.2	41.4	356	351	353	2.39						
Ni60	<0.51	5.09	<0.55	5.09	0	1264	433	152	235	521	441	1657	1408	1533	125						
Cu65	<0.33	<0.31	<0.32	-	-	0.82	<1.09	1.51	1.23	1.19	0.283	0.83	1.9	1.37	0.535						
Zn66	<0.75	<0.66	<0.69	-	-	56.2	26.6	58.9	62.2	50.9	14.2	86.4	93.0	89.7	3.34						
As75	<0.28	<0.30	<0.33	-	-	<0.176	<1.12	<0.29	0.36	0.36	0	<0.54	<0.52	-	-						
Rb85	<0.094	<0.102	<0.101	-	-	<0.075	<0.37	<0.085	<0.094	-	-	<0.171	<0.174	-	-						
Sr88	5.86	16.9	5.77	9.49	5.20	0.058	0.368	0.517	0.03	0.243	0.206	12.2	41.9	27.1	14.8						
Y89	0.056	0.0204	0.0222	0.0329	0.0164	0.027	0.242	0.019	0.024	0.078	0.0947	1.73	1.55	1.64	0.09						
Zr90	0.0123	0.0053	<0.034	0.0088	0.0035	0.026	0.218	0.051	<0.023	0.0983	0.0852	0.51	0.504	0.507	0.003						
Nb93	<0.0122	0.0027	<0.0124	0.0027	0	0.0069	<0.055	0.0091	<0.021	0.008	0.0011	0.028	<0.0209	0.028	0						
Mo95	<0.099	<0.055	<0.100	-	-	<0.052	<0.31	<0.090	<0.113	-	-	0.24	<0.17	0.24	0						
Sb121	<0.076	<0.076	<0.079	-	-	<0.055	<0.25	0.102	<0.087	0.102	0	<0.130	<0.131	-	-						
Cs133	<0.036	<0.027	<0.035	-	-	<0.024	<0.134	<0.025	<0.030	-	-	0.057	<0.066	0.057	0						
Ba137	1.6	11.12	0.94	4.55	4.65	0.09	0.074	0.211	<0.00	0.125	0.0612	12.98	57.66	35.3	22.3						
La139	<0.0073	0.0016	<0.00	0.0016	0	<0.0048	<0.0229	<0.0058	<0.00	-	-	0.0166	0.036	0.0263	0.0097						
Ce140	<0.0063	0.0014	0.0014	0.0014	0	<0.0042	0.0094	0.0048	0.0054	0.006533	0.002042	0.083	0.093	0.088	0.005						
Pr141	<0.00	<0.00	<0.00	-	-	0.003	<0.0289	<0.00	<0.00	0.003	0	0.0119	0.0036	0.00775	0.00415						
Nd146	0.032	<0.00	<0.0311	0.032	0	<0.00	<0.00	<0.00	<0.0308	-	-	0.047	0.106	0.0765	0.0295						
Sm149	<0.00	<0.00	<0.00	-	-	<0.00	<0.00	0.029	<0.00	0.029	0	0.029	0.026	0.0275	0.0015						
Eu151	<0.0099	<0.00	<0.00	-	-	<0.00	<0.0316	0.0075	<0.00	0.0075	0	<0.0169	0.041	0.041	0						
Gd157	0.0094	<0.035	0.0081	0.00875	0.00065	<0.0241	<0.113	<0.0288	<0.00	-	-	0.056	0.2	0.128	0.072						
Tb159	0.0027	<0.00	<0.00	0.0027	0	<0.0034	<0.0163	<0.0041	<0.00	-	-	0.0198	0.043	0.0314	0.0116						
Dy163	0.0162	<0.0199	0.0047	0.0105	0.00575	<0.00	<0.065	<0.00	<0.021	-	-	0.147	0.191	0.169	0.022						
Ho165	<0.0051	0.0011	0.0012	0.00115	0	<0.00	<0.0167	0.0039	<0.0052	0.0039	0	0.057	0.086	0.0715	0.0145						
Er167	<0.0224	<0.0215	0.005	0.005	0	<0.00	0.136	0.017	<0.0230	0.0765	0.0595	0.231	0.207	0.219	0.012						
Tm169	<0.0048	0.0021	<0.0049	0.0021	0	0.0057	0.0073	<0.00	0.0021	0.005033	0.002175	0.043	0.052	0.0475	0.0045						
Yb173	0.0073	0.019	<0.0286	0.0132	0.00585	<0.00	<0.00	0.022	0.013	0.0175	0.0045	0.226	0.183	0.2045	0.0215						
Lu175	0.0013	<0.00	0.0043	0.0028	0.0015	<0.0033	<0.00	0.0073	<0.00	0.0073	0	0.043	0.065	0.054	0.011						
Hf177	<0.00	<0.0222	<0.0235	-	-	<0.0223	0.035	<0.00	<0.00	0.035	0	0.018	0.016	0.017	0.001						
Ta181	<0.00	<0.00	<0.00	-	-	0.0028	0.0071	<0.00	<0.00	0.00495	0.00215	<0.00	<0.00	-	-						
W182	<0.00	<0.00	<0.00	-	-	0.534	1.09	0.041	0.031	0.424	0.435	2.24	0.515	1.38	0.863						
Pb208	<0.032	<0.027	<0.035	-	-	0.024	<0.109	0.056	0.044	0.0413	0.013199	<0.067	0.104	0.104	0						
Th232	<0.00	<0.00	<0.00	-	-	<0.00	<0.00	<0.00	<0.00	-	-	<0.00	<0.00	-	-						
U238	<0.00	0.0045	<0.00	0.0045	0	<0.00	<0.00	<0.00	<0.00	-	-	<0.00	<0.00	-	-						

A13. Field measurements

Dip	Dip azimuth	Description
63	80	OlF2
61	71	OlF2
77	50	Carbonate along fractures
79	53	Carbonate along fractures
65	98	OlF2
67	84	OlF2
69	84	OlF2
54	78	Serpentinite mylonite
76	128	Other Ol veins
73	127	Other Ol veins
75	131	Other Ol veins
76	116	Other Ol veins
75	130	Other Ol veins
73	122	Other Ol veins
47	110	Other Ol veins
66	92	Other Ol veins
59	104	Other Ol veins
75	319	OlF1
73	321	OlF1
80	328	OlF1
77	130	Other Ol veins
79	348	OlF1
79	322	OlF1
78	312	OlF1
74	322	OlF1
62	356	Other Ol veins
65	357	Other Ol veins
79	319	OlF1
75	314	OlF1
81	316	OlF1
72	51	Serpentinite mylonite
77	54	Serpentinite mylonite
89	66	Serpentinite mylonite
73	229	Serpentinite mylonite lineation
74	48	OlF2

References

Angiboust S., Wolf S., Burov E., Agard P., Yamato P., 2012 Effect of fluid circulation on subduction interface tectonic processes: Insights from thermos-mechanical numerical modelling. Earth and Planetary Science Letters 357-358 (2012) 238-248. http://dx.doi.org/10.1016/j.epsl.2012.09.012

Behr W. M., Bürgmann R. 2021. What's down there? The structures, materials and environment of deep-seated slow slip and tremor. Phil. Trans. R. Soc. A 379: 20200218. https://doi.org/10.1098/rsta.2020.0218

Behr W. M., Kotowski A. J., and Ashley K. T. 2018, Dehydration-induced rheological heterogeneity and the deep tremor source in warm subduction zones. Geology, v. 46; no. 5; p. 475–478. https://doi.org/10.1130/G40105.1

Beroza G. C. and Ide S. 2011. Slow Earthquakes and Nonvolcanic Tremor. Annu. Rev. Earth Planet. Sci. 2011. 39:271–96. doi: 10.1146/annurev-earth-040809-152531

Brown J. R., Prejean S. G., Beroza G. C., Gomberg J. S., Haeussler P. H. 2013. Deep low frequency earthquakes in tectonic tremor along the Alaska-Aleutian subduction zone. J. Geophys. Res. Solid Earth, 118, 1079–1090. doi: 10.1029/2012JB009459

Bürgmann R. 2018. The geophysics, geology and mechanics of slow fault slip. Earth and Planetary Science Letters, 495, 112–134 https://doi.org/10.1016/j.epsl.2018.04.062

Cannaò E., Scambelluri M., Agostini S., Tonarini S., Godard M., 2016. Linking serpentinite geochemistry with tectonic evolution at the subduction-plate interface: The Voltri Massif case study (Ligurian Western Alps, Italy). Geochimica et Cosmochimica Acta 190 (2016) 115–133. http://dx.doi.org/10.1016/j.gca.2016.06.034

Clarke E., De Hoog J. C. M., Kirstein L. A., Harvey J., Debret B., 2020. Metamorphic olivine record external fluid infiltration during serpentinite dehydration. Geochem. Persp. Let. (2020) 16, 25–29. doi: 10.7185/geochemlet.2039 25

Compagnoni R., Cossio R., Mellini M., 2021. Raman anisotropy in serpentinite minerals, with a caveat on identification. J Raman Spectrosc. 2021;52:1334–1345. doi: 10.1002/jrs.6128

Dandar O., Okamoto A., Uno M., Oyanagi R., Nagaya T., Burenjargal U., Miyamoto T., Noriyoshi T., 2019. Formation of secondary olivine after orthopyroxene during hydration of mantle wedge: evidence from the Khantaishir Ophiolite, western Mongolia. Contributions to Mineralogy and Petrology (2019) 174:86. https://doi.org/10.1007/s00410-019-1623-1

Deschamps F., Godard M., Guillot S., Hattori K., 2013. Geochemistry of subduction zone serpentinites: A review. Lithos 178 (2013) 96–127. http://dx.doi.org/10.1016/j.lithos.2013.05.019

Frost B. R., Beard J. S., 2007. On silica activity and Serpentinization. J. of Petrology Vol. 48, 7, 1351-1368. doi:10.1093/petrology/egm021

Frost B. R., Evans K. A., Swapp S. M., Beard J. S., Mothersole F. E., 2013. The process of serpentinization in dunite from New Caledonia. Lithos 178 (2013) 24–39. http://dx.doi.org/10.1016/j.lithos.2013.02.002

Giuntoli F., Viola G., Sorensen B. E. 2022. Deformation machanisms of blueschist facies continental metasediments may offer insights into deep episodic tremor and slow slip events. Journal of Geophysical Research: Solid EarthVolume 127, Issue 10JB024265. https://doi.org/10.1029/2022JB024265

Groppo C., Rinaudo C., Cairo S., Gastaldi D., Compagnoni R., 2006. Micro-Raman spectroscopy for a quick and reliable identification of serpentinite minerals from ultramafics. Eur. J. Mineral 18, 319-329. Doi: 10.1127/0935-1221/2006/0018-0319

Guillot S., Schwartz S., Reynard B., Agard P., Pringent C., 2015. Tectonic significance of serpentinites. Tectonophysics 646 (2015) 1–19. http://dx.doi.org/10.1016/j.tecto.2015.01.020

Hermann J., Müntener O., Scambelluri M. 2000. The importance of serpentinite mylonites for subduction and exhumation of oceanic crust. Tectonophysics 327, 225±238. https://doi.org/10.1016/S0040-1951(00)00171-2

Kempf E. D., Hermann J., Reusser E., Baumgartner L. P., Lanari P., 2020. The role of the antigorite + brucite to olivine reaction in subducted serpentinites (Zermatt, Swizterland). Swiss J Geosci (2020) 113:16. https://doi.org/10.1186/s00015-020-00368-0

Kirkpatrick J. D. Fagereng Å., Shelley D. R. 2021. Geological constraints on the mechanisms of slow earthquakes. Nature review. https://doi.org/10.1038/s43017-021-00148-w

McDonough W. F. and Sun S. S., 1995. The composition of the Earth. Chemical Geology 120 (1995) 223-253. doi: 10.1016/0009-2541(94)00140-4

Messiga B., Scambelluri M., Piccardo G. B. 1995. Chloritoid-bearind assemblages in mafic systems and eclogite-facies hydration of alpine Mg-Al metagabbros (Erro-Tobbio Unit, Ligurian Western Alps). Eur. J. Mineral., 7, 1149-1167. doi: 10.1127/ejm/7/5/1149

Nagaya T., Wallis S. R., Seto Y., Miyake A., Soda Y., Uehara S., Matsumoto M., 2017. Minimizing and quantifying mis-indexing in electron backscatter diffraction (EBSD) determinations of antigorite crystal directions. Journal of Structural Geology 95 (2017) 127e141. http://dx.doi.org/10.1016/j.jsg.2016.12.006

Nagaya T., Okamoto A., Kido M., Muto J., Wallis S. R., 2022. Dehydration of brucite+antigorite under mantle wedge conditions: insights from the direct comparison of microstructures before and after experiments. Contributions to Mineralogy and Petrology (2022) 177: 87. https://doi.org/10.1007/s00410-022-01956-z

Obara K., Kato A. 2016. Connecting slow earthquakes to huge earthquakes. Science 353 (6296), 253-257. doi: 10.1126/science.aaf1512

Pennacchioni G., Scambelliru M., Bestmann M., Notini L., Nimis P., Plümper O., Faccenda M., Nestola F., 2020. Record of intermediate-depth subduction seismicity in a

dry slab from an exhumed ophiolite. Earth and Planetary Science Letters 548 (2020) 116490 https://doi.org/10.1016/j.epsl.2020.116490

Peters D., Bretschera A., John T., Scambelluri M., Pettke T. 2017. Fluid-mobile elements in serpentinites: Constraints on serpentinization environments and element cycling in subduction zones. Chemical Geology 466, 654–666. http://dx.doi.org/10.1016/j.chemgeo.2017.07.017

Peters D., Pettke T., John T., Scambelluri M. 2020. The role of brucite in water and element cycling during serpentinite subduction – Insights from Erro Tobbio (Liguria, Italy). Lithos 360–361, 105431. https://doi.org/10.1016/j.lithos.2020.105431

Petriglieri J. R., Salvioli-Mariani E., Mantovani L., Tribaudino M., Lottici P. P., Laporte-Magoni C., Bersani D., 2015. Micro-Raman mapping of the polymorphs of serpentine. J. Raman Spectrosc., 46: 953– 958. doi: 10.1002/jrs.4695

Plümper O., John T., Podladchikov Y. Y., Vrijmoed J. C., Scambelluri M. 2017. Fluid escape from subduction zones controlled by channel-forming reactive porosity. Nature Geoscience, v. 10, 150–156. https://doi.org/10.1038/ngeo2865

Rinaudo C., Gastaldi D., 2003. Characterization of chrysotile, antigorite and Lizardite by FT-Raman spectroscopy. The Canadian Mineralogist Vol. 41, pp. 883-890.

Rogers G., Dragert H. 2003. Episodic Tremor and Slip on the Cascadia Subduction Zone: The Chatter of Silent Slip. Science 300(5627):1942-3. doi: 10.1126/science.1084783.

Rowe C. D. and Griffith W. A. 2015. Do faults preserve a record of seismic slip: A second opinion. Journal of Structural Geology 78, 1e26. http://dx.doi.org/10.1016/j.jsg.2015.06.006

Scambelluri, M., Hoogerduijn Strating E. H., Piccardo G. B., Vissers R. L. M. and Rampone E. 1991. Alpine olivine- and titanian clinohumite-bearing assemblages in the Erro-Tobbio peridotite (Voltri Massif, NW Italy). J. metamorphic Geol., 9, 79-91. https://doi.org/10.1111/j.1525-1314.1991.tb00505.x

Scambelluri M., Müntener O., Hermann J., Piccardo G. B., Trommsdorff V., 1995. Subduction of water into the mantle: History of an Alpine peridotite. Geology; v. 23; no. 5; p. 459–462 .

Scambelluri M., Piccardo G. B., Philippot P., Robbiano A., Negretti L. 1997. High salinity fluid inclusions formed from recycled seawater in deeply subducted alpine serpentinite. Earth and Planetary Science Letters 148, 485-499. https://doi.org/10.1016/S0012-821X(97)00043-5

Scambelluri M., Pennacchioni G., Gilio M., Bestmann M, Plümper O., Nestola F., 2017. Fossil intermediate-depth earthquakes in subducting slabs linked to differential stress release. Nature Geoscience V. 960 10 (2017) 960–966 https://doi.org/10.1038/s41561-017-0010-7

Scambelluri M., Cannaò E. Gilio M. 2019. The water and fluid-mobile element cycles during serpentinite subduction. A review. Eur. J. Mineral., 31, 405–428. https://doi.org/10.1127/ejm/2019/0031-2842

Schwartz S. Y. and Rokosky J. M. 2007. Slow-slip events and seismic tremor at circum-pacific subduction zones. Rev. Geophys., 45, RG3004, doi:10.1029/2006RG000208.

Shelly D. R., Beroza G. C. Ide S. 2007. Non-volcanic tremor and low-frequency earthquake swarms. Nature 446, 305–307. https://doi.org/10.1038/nature05666

Sonzogni, Y., Treiman, A. H. and Schwenzer, S. P. (2017). Serpentinite with and without brucite: A reaction pathway analysis of a natural serpentinite in the Josephine ophiolite, California. Journal of Mineralogical and Petrological Sciences, 112(2) pp. 59–76. http://dx.doi.org/doi:10.2465/jmps.160509

Šontevske V., Jovanovski G., Makreski P., 2007. Minerals from Macedonia. Part XIX. Vibrational spectroscopy as identification tool for some sheet silicate minerals. Journal of Molecular Structure 834–836 (2007) 318–327. doi:10.1016/j.molstruc.2006.10.026

Tapani Holmi J., Lipsanen H., 2022. WITio: A MATLAB data evaluation toolbox to script broader insights into big data from WITec microscopes. SoftwareX 18 (2022) 101009. https://doi.org/10.1016/j.softx.2022.101009

Toffol. G., Yang J., Pennacchioni G., Faccenda M., Scambelluri M., 2022. How to quake a subducting dry slab at intermediate depths: Inferences from numerical modelling. Earth and Planetary Science Letters 578 (2022) 117289. https://doi.org/10.1016/j.epsl.2021.117289

Vignaroli G., Rossetti F., Rubatto D., Theye T., Lisker F., Phillips D. 2010. Pressure-temperature-deformation-time (P-T-d-t) exhumation history of the Voltri Massif HP complex, Ligurian Alps, Italy. Tectonics, Vol. 29, TC6009. doi:10.1029/2009TC002621

Uno M., Kirby S., 2019. Evidence for multiple stages of serpentinization from the mantle through the crust in the Redwood City Serpentinite melange along the San Andreas Fault in California. Lithos 336-337 (2019) 276-292. https://doi.org/10.1016/j.lithos.2019.02.005

Zahn Z. 2020. Mechanisms and Implications of Deep Earthquakes. Annu. Rev. Earth Planet. Sci. 2020. 48:147–74. https://doi.org/10.1146/annurev-earth-053018-060314

Zucali M., Marinoni N., Diella V., Croce A., Rinaudo C., Fontana E., 2018. Deciphering the tectonic-geodynamic context of the gem-quality “noble serpentine” deposit formation combining microstructural, chemical and micro-Raman analyses in Palaeozoic olivine-bearing marbles and serpentine-hosting rocks (Pizzo Tremogge, Margna unit – Austroalpine, Val Malenco – Central Alps, Italy). Ore Geology Reviews 92 257-270. https://doi.org/10.1016/j.oregeorev.2017.11.020

Ringraziamenti

Volevo ringraziare innanzitutto i miei genitori, per avermi sempre supportato in questo percorso. Ringrazio il Prof. Pennacchioni che mi ha trasmesso la sua passione e mi ha permesso di portare avanti questo progetto. Grazie perché in pochi mesi di lavoro ho imparato davvero molto. Ringrazio anche i miei amici, che mi hanno sopportato in quest'ultimo periodo senza mai abbandonarmi, nonostante non sia stata molto presente e abbia rotto le scatole con questa tesi. Grazie soprattutto a Luli e Nicola. Un enorme grazie alla Prof.ssa Franca Perin che, nonostante la geologia non fosse la sua passione, mi ha trasmesso un interesse infinito per le scienze.

Feel alive